QA: N/A

Civilian Radioactive Waste Management System
Management & Operating Contractor

Single Heater Test Interim Report

BABEAF000-01717-6900-0001 REV 00

February 1997

Prepared for:

U.S. Department of Energy
Yucca Mountain Site Characterization Office
P.O. Box 30307
North Las Vegas, NV 89036-0307

Prepared by:

TRW Environmental Safety Systems Inc.
1180 Town Center Drive
Las Vegas, Nevada 89134

Under Contract Number
DE-AC01-91RW00134

CONTENTS

CONTENTS (Continued)

FIGURES

FIGURES (Continued)

TABLES

INTENTIONALLY LEFT BLANK

ACRONYMS

ASTM	American Society for Testing and Materials
CRWMS	Civilian Radioactive Waste Management System
DAS	Data Acquisition System
DST	Drift Scale Test
EMF	Electromagnetic Field
ERT	Electrical Resistivity Tomography
ESF	Exploratory Studies Facility
FETT	First ESF Thermal Test
GPa	GigaPascal
GPR	Ground Penetrating Radar
IR	Infrared
LANL	Los Alamos National Laboratory
LBNL	Lawrence Berkeley National Laboratory
LLNL	Lawrence Livermore National Laboratory
LVDT	Linear Variable Displacement Transducer
M&O	Management and Operating Contractor
MPBX	Multi-Point Borehole Extensometers
NUFT	Non-Isothermal Unsaturated Flow and Transport Code
RBLC	Rock Bolt Load Cells
REKA	Rapid Evaluation of K and Alpha
RMR	Rock Mass Rating
RTD	Resistance Temperature Detectors
SCP	Site Characterization Plan
SHT	Single Heater Test
SNL	Sandia National Laboratories
TBM	Tunnel Boring Machine
TC	Thermocouple
TCO	Technical Coordination Office/Officer
TDIF	Technical Data Information Form
THM	Thermal-Hydrological-Mechanical
TM	Thermal-Mechanical

ACRONYMS (Continued)

TMHC	Thermal Mechanical Hydrologic Geochemical
TOUGH2	Transport of Unsaturated Groundwater and Heat (computer code)
Tpt	Topopah Spring tuff
Tptpmn	Topopah Tuff, Crystal Poor, Middle Nonlithophysal
Tsw2	Topopah Spring - Densely Welded Devitrified Lithophysal-Poor Tuff
WBS	Work Breakdown Structure
WX	Wire Extensometers
WXM	Wire Tape Extensometers

1. INTRODUCTION

1.1 BACKGROUND

The Exploratory Studies Facility (ESF) Thermal Test Facility, shown schematically in Figure 1-1, is an integral part of the program of site investigations to characterize Yucca Mountain in Nye County, Nevada for the permanent disposal of spent nuclear fuel and high level nuclear waste. The purpose of the ESF Thermal Test is to understand better the coupled thermal, mechanical, hydrological, and chemical processes likely to exist in the rock mass surrounding the potential geologic repository at Yucca Mountain. Plans for a suite of in situ thermal tests to be conducted in the ESF began with the *Site Characterization Plan* (SCP) (DOE 1988). The planning basis documented in the SCP has evolved over the past several years to meet the changing needs and updated knowledge base of the project. The most recent iteration, in which the SCP thermal testing program was re-evaluated and consolidated, is discussed in *In Situ Thermal Testing Program Strategy* (DOE 1995a). The ESF Thermal Test is being conducted in a facility specifically constructed for this purpose in the middle nonlithophysal (Tptpmn) lithologic unit of the thermomechanical unit TSw2, the proposed repository horizon.

The ESF Thermal Test facility general location and plan view are shown in Figures 1-2 and 1-3, respectively. The ESF Thermal Test will consist of two heater tests, the Single Heater Test (SHT) and Drift Scale Test (DST), along with an east-west observation drift driven from the ESF main drift, and a connecting drift. Most measurements will be made via instruments placed in boreholes.

Table 1-1 provides a comprehensive listing of information needs in terms of parameters to be measured in the ESF Thermal Test. Also included in the table are the corresponding instruments, which will measure these parameters in the SHT and/or DST.

Table 1-2 provides a matrix of thermally related processes and parameters which are considered relevant to the SHT. Specifically, four types of processes are identified: thermal, mechanical, hydrological, and chemical. Each process consists of several subprocesses which are labeled in terms of their importance as either primary or secondary. Primary processes will receive much emphasis and will be addressed directly in the SHT. Secondary processes will receive less attention but their understanding will be advanced as a result of the SHT. The SHT will provide useful insights in many key areas such as construction; instrument installation, measuring systems, and numerical predictions which will be beneficial to the implementation of the DST.

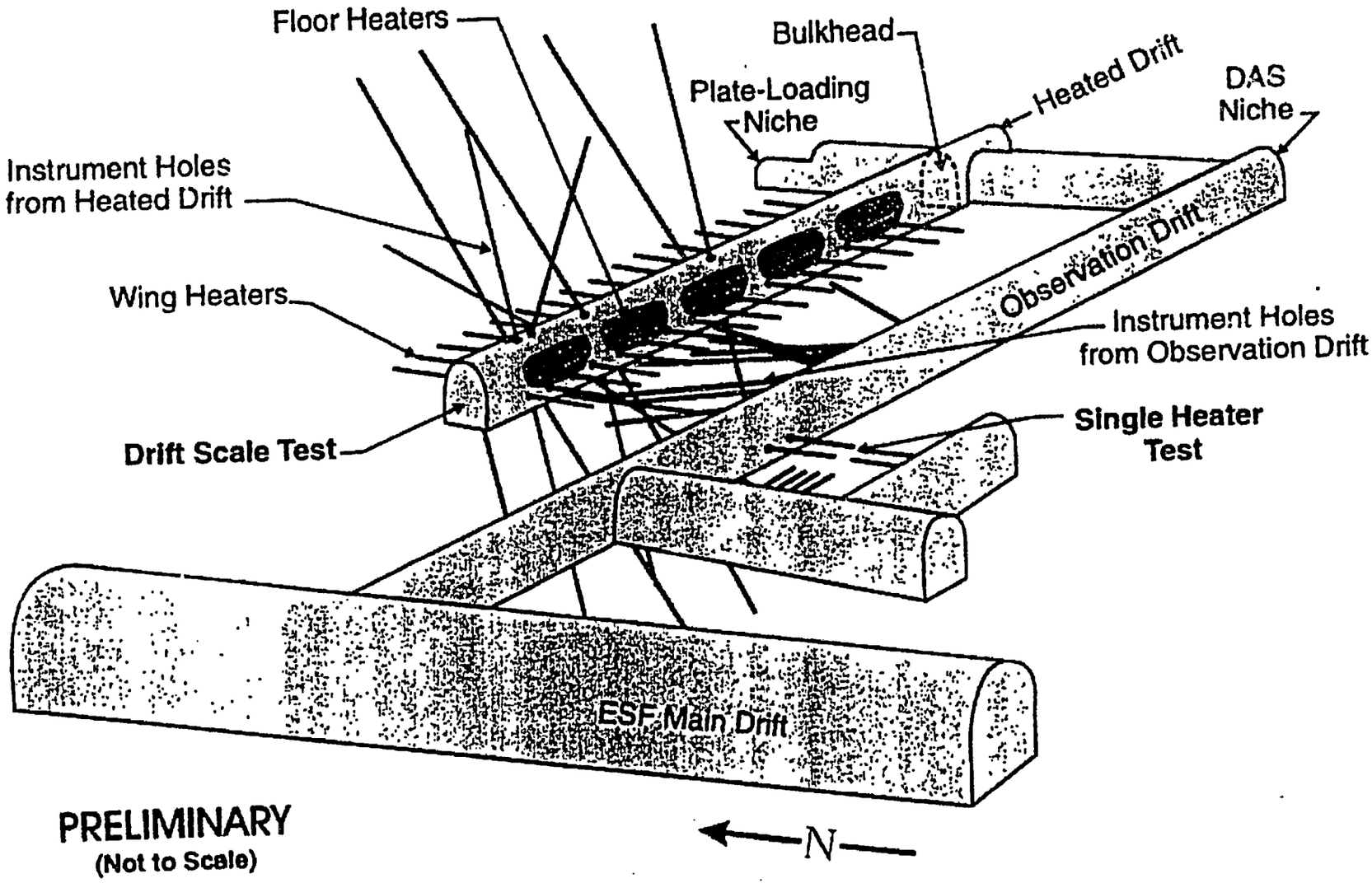

Figure 1-1. Schematic of ESF Thermal Test Facility

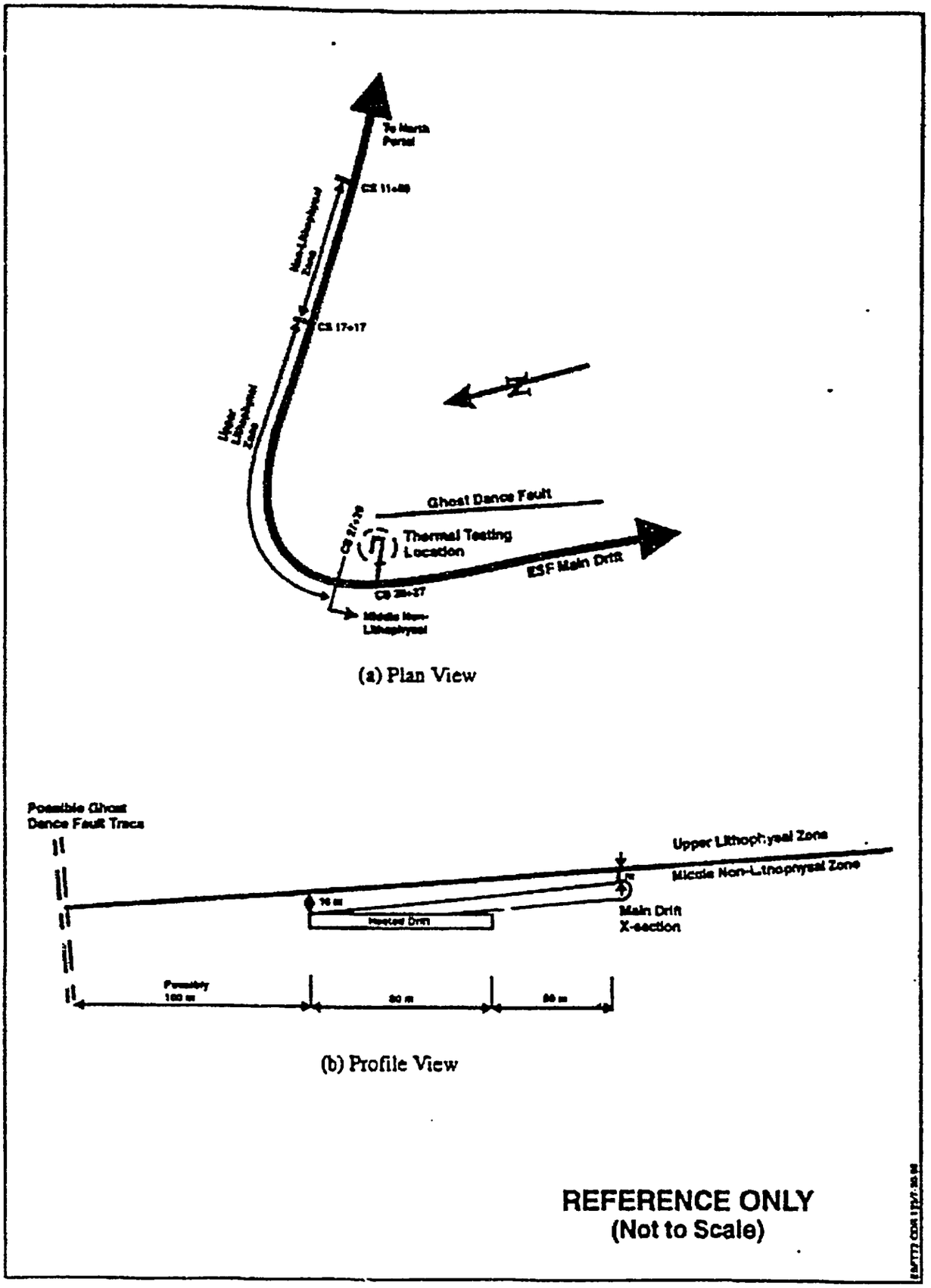

(a) Plan View

(b) Profile View

Figure 1-2. General Location of the ESF Thermal Test

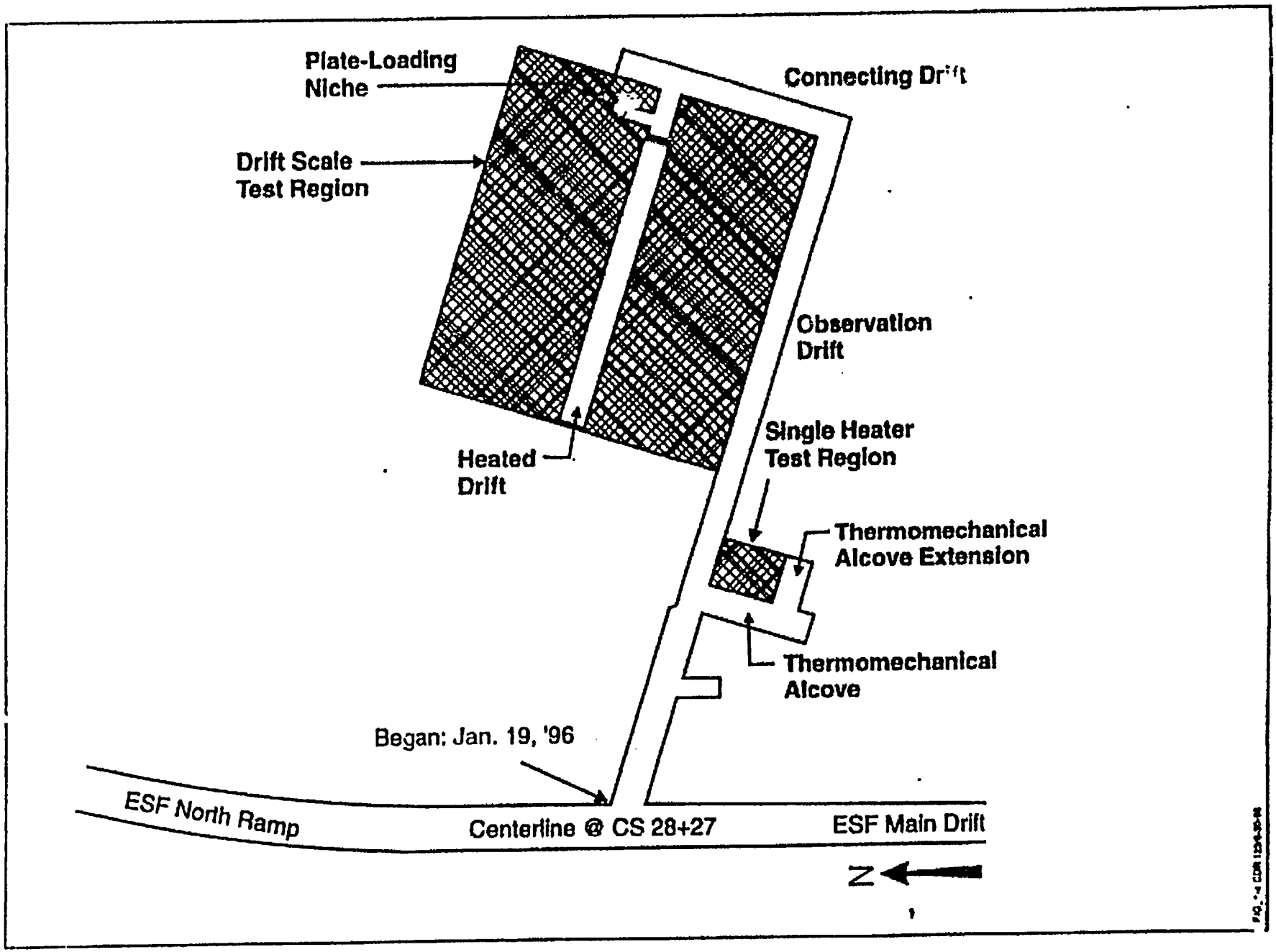

Figure 1-3. Plan View of ESF Thermal Test Facility

Table 1-1. Listing of Parameters and Corresponding Instrumentation

Information Needs/Parameters	Instrumentation Types
Heat Capacity (Specific Heat)	• Resistance Temperature Detectors (RTD) • Thermocouples • Rapid Evaluation of K and Alpha-Thermal Probes (REKA)
Thermal Conductivity	• Resistance Temperature Detectors (RTD) • Thermocouples • Rapid Evaluation of K and Alpha-Thermal Probes (REKA)
Thermal Expansion	• Multi-Point Borehole Extensometers (MPBX) • Optical Multi-point Borehole Extensometers • Wire Extensometers
Deformation Modules	• Goodman Borehole Jack • Plate-Loading
Rock-Mass Ground Support Interaction	• Rock Bolt Load Cells • Pull Tests • Multi-Point Borehole Extensometers (MPBX) • Wire (Cross-Drift) Extensometers • Pressure Cells • Strain Gages (Concrete/Shotcrete)
Changes in Water Saturation	• Humicaps • Neutron Logging • Electrical Resistivity Tomography (ERT) • Ground Penetrating Radar
Water Chemistry	• Micro Electrode Array Chemical Sensors * • Post-test Observations on Coupons of Waste Package Materials • Borehole Fluid Sampling
Mineralogic Changes	• Micro Electrode Array Chemical Sensors * • Post-test Sampling and Analyses of Rock Samples * • Borehole Fluid Sampling
Propagation of "Drying Front"	• Humicaps • Neutron Logging • Electrical Resistivity Tomography (ERT) • Resistance Temperature Detectors (RTD) • Gas Permeability • Thermocouples
Residual Water Saturation in "Dry Zone"	• Humicaps • Neutron Logging • Electrical Resistivity Tomography (ERT)
Drainage/Reflux of Liquid by Fracture Flow	• Infrared Imaging • Detailed Fracture Mapping • Fluid Sampling • Electrical Resistivity Tomography (ERT) • Resistance Temperature Detector (RTD) • Neutron Logging
Rock-Mass and Fracture Permeability Changes	• Gas Permeability Measurements • Gas Gage Pressure Transducers
Conductive/Convective Heat Transfer	• Gas Gage Pressure Transducers • Resistance Temperature Detector (RTD) • Thermocouples • Rapid Evaluation of K and Alpha-Thermal Probes
In Situ Stress and Stress Orientation	• Overcoring Methods • Hydraulic Fracturing

Table 1-1. Listing of Parameters and Corresponding Instrumentation (Continued)

Information Needs/Parameters	Instrumentation Types
Seismic Velocity	• Geophones • Accelerometers
Convergence, Convergence Rate, and Rock-Mass Displacement	• Multi-Point Borehole Extensometers (MPBX) • Optical Multi-Point Borehole Extensometers • Tape Extensometers • Wire Extensometers
Air Permeability	• Borehole Packers with Pressure Transducers and Flowmeters
Moisture Content and Water Potential	• Borehole Packers with Humicaps
Relative Humidity and Drift Wall Moisture	• Humicaps • Infrared Imaging Camera

* Installed with SEAMIST System in Borehole

1.2 PURPOSE

The purpose of the interim report on the SHT is most appropriately stated in the following Criteria Statement:

> This report will document the results of an integrated analysis of the results of the first three to four months of the heating phase of the SHT started on August 26, 1996. Measurements made by various sensors, instruments and methods will be presented at selected time steps and compared with corresponding predicted results. Synergistic interpretive analyses of observed data leading to inferences, if any, about heat-related processes such as heat transfer mechanism, dry-out and condensation zone formation will be reported. Rock mass thermal expansion derived from thermal and mechanical measurements and rock mass deformation modulus at elevated temperatures as directly measured will be reported. An evaluation of the performance of the various measuring systems will be presented.

Accordingly, the contents of this report includes separate sections on predictions and measurements which are summations of previously submitted reports. A comparative analyses of predictions and measurements and a set of conclusions are also included.

1.3 SINGLE HEATER TEST DESCRIPTION

The SHT is part of the ESF Thermal Test being conducted underground at the potential high-level nuclear waste repository at Yucca Mountain, Nevada. This experiment will provide a preliminary evaluation of coupled thermal-mechanical-hydrologic-geochemical (TMHC) processes expected to occur during waste emplacement at Yucca Mountain. The ESF Thermal Test includes the SHT and a DST. Although borehole emplacement is not considered likely at this time, the geometry of the test is useful for directly measuring rock mass thermal and thermomechanical properties such as thermal conductivity, thermal expansion, and rock mass modulus.

The SHT is being conducted in the Topopah Spring Welded Tuff lithologic unit (middle-nonlithophysal) in a facility located south of the north ramp and east of the north-south main drift. The location of the Thermal Testing Facility is shown schematically in Figures 1-1 through 1-3. The

SHT block is bounded on the north by the Observation Drift (declining at about 10 percent), on the west by the Thermomechanical Alcove, and on the south by the Thermomechanical Alcove Extension. The dimensions of the excavations are given in Figure 1-4. Refer to CRWMS (1996a), for specific details regarding the test and facility design.

Figure 1-4 shows the conceptual layout for the SHT in plan and cross-section. The SHT includes a long (5 m) heater at a slight upward incline in a borehole in the west face of the test block. The test configuration includes the heater in roughly the center (plan view) of the test block, with instrumentation access from all three free surfaces bounded by the excavations.

The SHT heater was activated on August 26, 1996. This report presents measured data collected during the first quarter of heating (through November 30, 1996) and numerical data for the duration of the test. Specifically, measured data is acquired from instrumentation installed in boreholes that monitor thermal, mechanical, hydrological, and chemical responses within the SHT block.

As noted previously, the layout for the SHT includes the block of the Topopah Spring Welded Tuff bounded by the Observation Drift on the north, the Thermomechanical Alcove on the west, and the Thermomechanical Alcove Extension on the south. Forty-one boreholes are drilled in the SHT block, which include tape extensometer pins and wire extensometer stations. Figures 1-5 and 1-6 show the general borehole layout in plan and cross-section views. Figure 1-6 also includes a table listing the heater and instrumentation boreholes which are numbered between 1 and 41. Also listed are the types of instruments installed, borehole diameter, borehole length, and additional information related to the instrument.

1.4 CHARACTERIZATION AND SENSOR INFORMATION

Ambient site characterization information was obtained from data gathered in situ at the SHT block as well as from core taken from selected boreholes (CRWMS, 1996b). The characterization information includes bulk permeability from air injection tests, water saturation from laboratory testing, rock mass quality assessments (Q and RMR) from scanline mapping, intact modulus and Poisson's ratio from laboratory testing, and intact thermal conductivity from laboratory testing. This characterization information was used in pretest analyses of the SHT.

Table 1-2. Matrix of Processes Relevant to the Single Heater Test

Heat Related Processes and Parameters	First ESF Thermal Test
Thermal	
Conduction	Primary
Convection	Secondary
Radiation	Secondary
Heat Pipes	Secondary
Enhanced Diffusion	Secondary
Effect of Percolation on Temperature Distribution	Secondary
Hydrological	
Sub-Boiling Mobilization (toward drift)	Primary
Sub-boiling Mobilization (away from drift)	Secondary
Dry-out Zone Formation (boiling/sub-boiling)	Secondary
Two Phase Water Movement From Dry-Out Zone	Secondary
Vapor Movement from Condensation Zone	Secondary
Shedding/Drainage from Condensation Zone	Secondary
Imbibition in Condensation Zone	Secondary
Vapor Removal (engineered system)	Secondary
Rewetting Time	Secondary
"Downspout" Rewetting	Secondary
Effect of Lateral Condensation on Downspout Rewetting	Secondary
Mechanical	
Rock-Mass Properties	Primary
Drift Stability, Preclosure	Secondary
Drift Stability, Postclosure	Secondary
Fracture Aperture Change	Secondary
New Fracture Formation	Secondary
Near Field Stress/Displacement	Secondary
Ground Support—Rock Mass Interaction	Secondary
Chemical	
Return Water Chemistry (to waste package)	Secondary
Evolution of Near Field Water Chemistry	Secondary
Change to Hydrologic Pathways	Secondary
Change to Matrix Transport Properties	Secondary

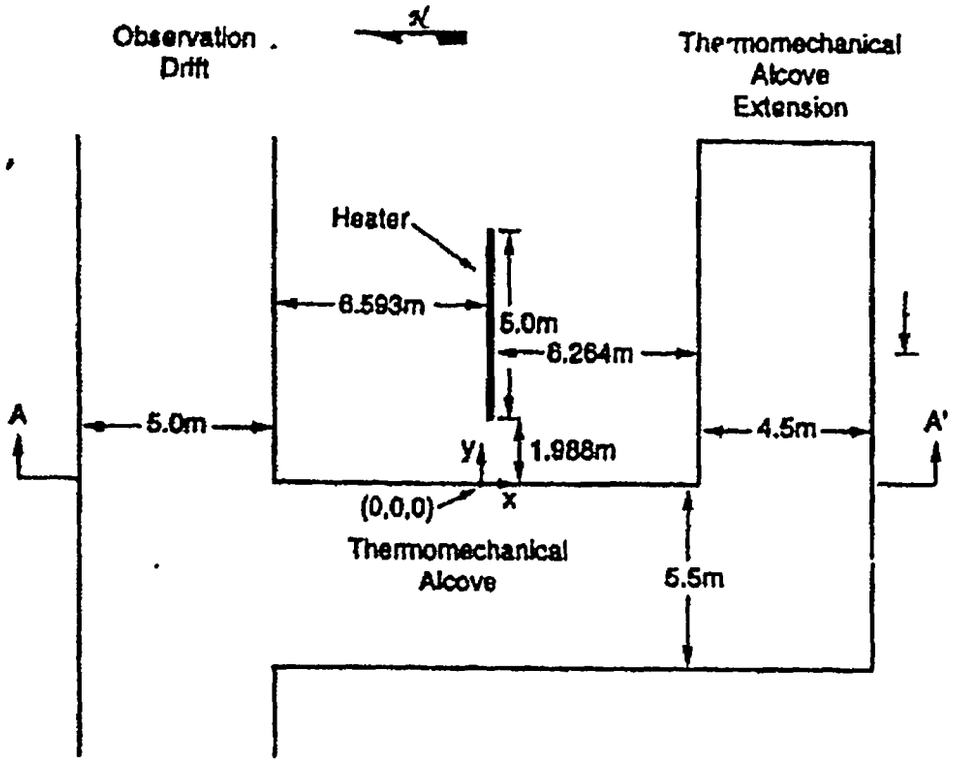

a). Plan View

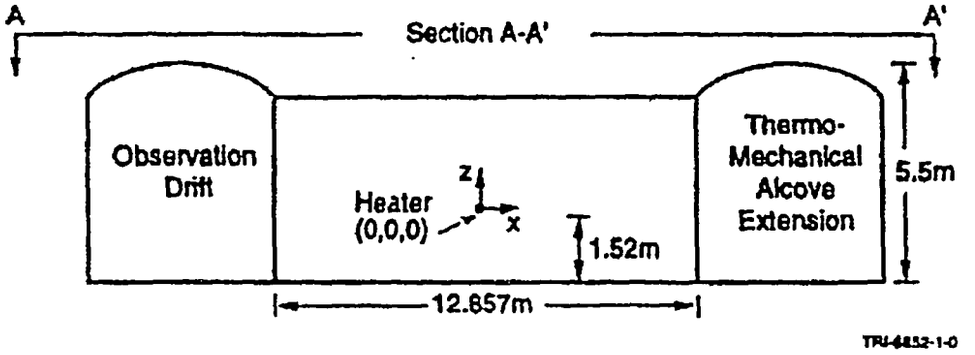

b). Cross-Section

Figure 1-4. Geometric Description of the SHT

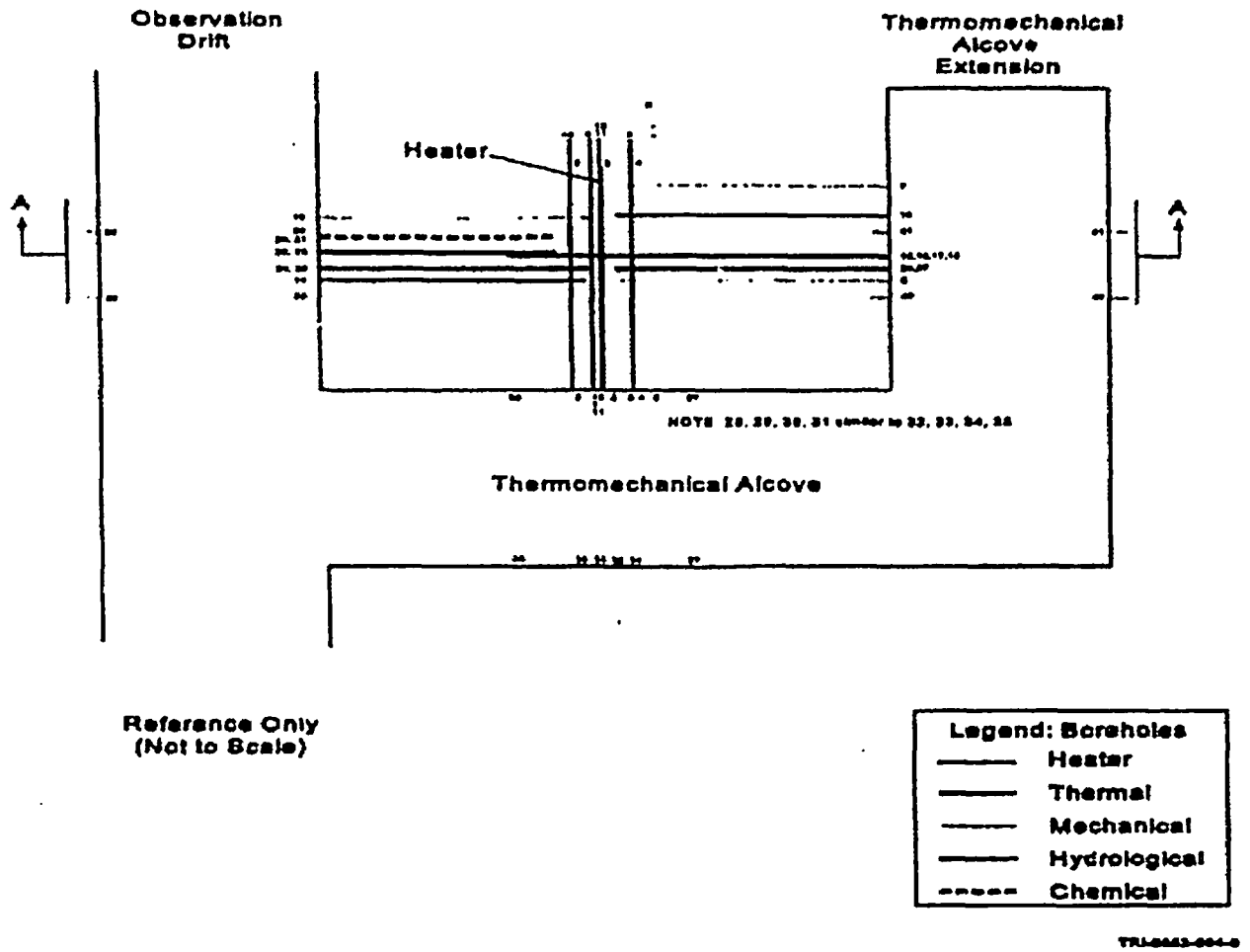

Figure 1-5. Layout of Single Heater Test (Plan)

The sensor locations are given in x, y, z coordinates (with the heater borehole collar at 0,0,0) in Appendix A. The positive directions for the right-hand coordinate system are north to south, west to east, and vertically up for the x, y, z axes, respectively. The gages included thermocouples (TCs), resistance temperature devices (RTDs), thermistors, multiple point borehole extensometers (MPBXs), wire extensometers (WXs), tape extensometers (WXM) [illegible] bolt load cells (RBLCs), Goodman jack measurements, humicaps, and heater power. Sensor locations for other measuring systems such as electrical resistance tomography (ERT) and neutron logging, which are not part of the ongoing data acquisition system, are not presented. These sensors are not defined by discrete locations but rather along borehole lengths.

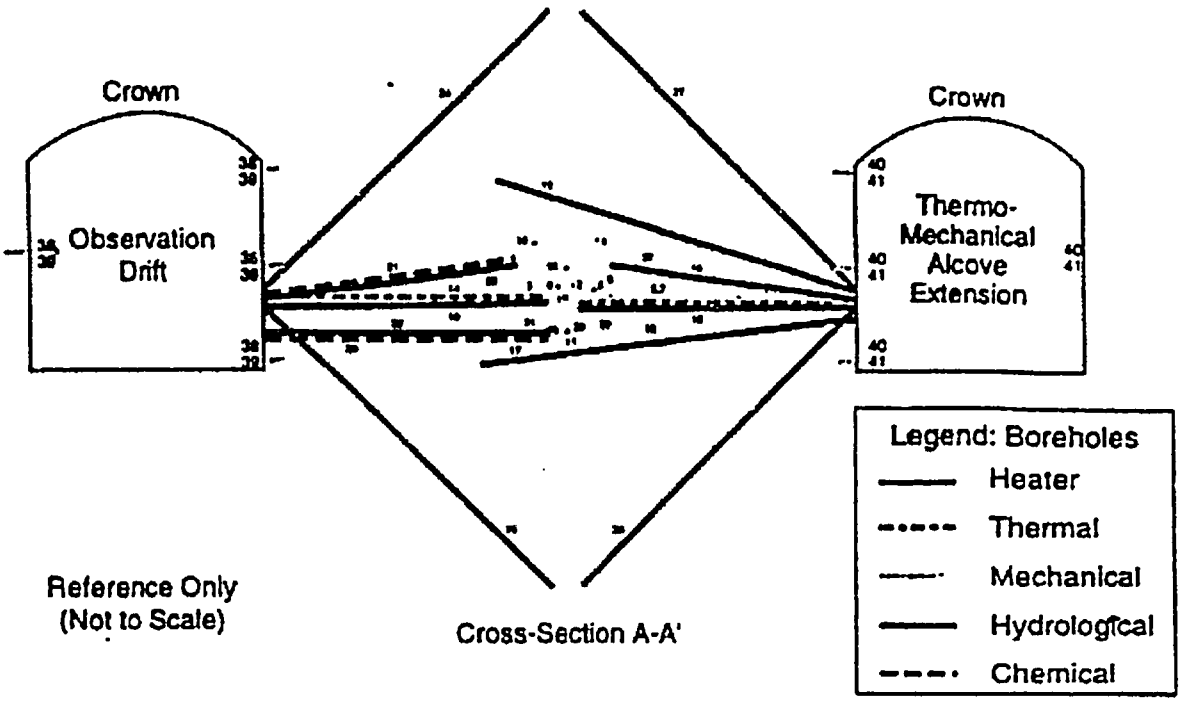

Fig. ID #	Borehole Instrument	Dia. (cm)	Length (m)	Additional Instrument Information
1	Heater	9.8	7.00	5m Long Heater w/Metallic Spring Centralizers
2	MPBX	7.57	7.00	6-pt Extensometers
3	MPBX	7.57	7.00	6-pt Extensometers
4	MPBX	7.57	7.00	6-pt Extensometers
5	MPBX	7.57	6.20	6-pt Extensometers
6	Optical MP	7.57	12.00	Laser Reflection MPBX System
7	Optical MP	7.57	6.20	Laser Reflection MPBX System
8	Thermocouple	4.80	8.00	Thermocouple Probes Grouted in Hole
9	Thermocouple	4.80	8.00	Thermocouple Probes Grouted in Hole
10	Thermocouple	4.80	8.00	Thermocouple Probes Grouted in Hole
11	Thermocouple	4.80	8.00	Thermocouple Probes Grouted in Hole
12	Thermocouple	4.80	8.00	Thermocouple Probes Grouted in Hole
13	Thermocouple	4.80	6.20	Thermocouple Probes Grouted in Hole
14	Thermocouple	6.40	6.20	Thermocouple Probes Grouted in Hole
15	Neutron Probe & Temp	7.57	8.50	Temp Probe Grouted Between Hole and Small Pipe
16	Hydrology	7.57	5.50	Humidity Sensors (Humicaps) in Packer Systems
17	Neutron Probe & Temp	7.57	8.50	Temp Probe Grouted Between Hole and Small Pipe
18	Hydrology	7.57	5.00	Humidity Sensors (Humicaps) in Packer Systems
19	Borehole Jack	7.57	6.20	Open Hole for Borehole Jack
20	Chemistry - SEAMIST	7.57	5.00	SEAMIST System with Chemical Sensors
21	Chemistry - SEAMIST	7.57	5.50	SEAMIST System with Chemical Sensors
22	Neutron Probe & Temp	7.57	5.00	Temp Probe Grouted Between Hole and Small Pipe
23	Neutron Probe & Temp	7.57	5.50	Temp Probe Grouted Between Hole and Small Pipe
24	Electrical Resistivity Tomography	7.57	8.70	Electrical Resistivity Tomography
25	Electrical Resistivity Tomography	7.57	8.70	Electrical Resistivity Tomography
26	Electrical Resistivity Tomography	7.57	8.70	Electrical Resistivity Tomography
27	Electrical Resistivity Tomography	7.57	8.70	Electrical Resistivity Tomography
28	Rock Bolt w/ Load Cell	6.67	5.00	Vibrating Wire Load Cell on Head of Rock Bolt
29	Rock Bolt w/ Load Cell	6.67	5.00	Vibrating Wire Load Cell on Head of Rock Bolt
30	Rock Bolt w/ Load Cell	6.67	5.00	Vibrating Wire Load Cell on Head of Rock Bolt
31	Rock Bolt w/ Load Cell	6.67	5.00	Vibrating Wire Load Cell on Head of Rock Bolt
32	Rock Bolt w/ Load Cell	6.67	5.00	Vibrating Wire Load Cell on Head of Rock Bolt
33	Rock Bolt w/ Load Cell	6.67	5.00	Vibrating Wire Load Cell on Head of Rock Bolt
34	Rock Bolt w/ Load Cell	6.67	5.00	Vibrating Wire Load Cell on Head of Rock Bolt
35	Rock Bolt w/ Load Cell	6.67	5.00	Vibrating Wire Load Cell on Head of Rock Bolt
36	Tape Extensometer Array 3	2.54	Up to 0.5	4-pin Tape Extensometer Array
37	Tape Extensometer Array 3	2.54	Up to 0.5	4-pin Tape Extensometer Array
38	Tape Extensometer Array 3	2.54	Up to 0.5	4-pin Tape Extensometer Array
39	Tape Extensometer Array 3	2.54	Up to 0.5	4-pin Tape Extensometer Array
40	Tape Extensometer Array 3	2.54	Up to 0.5	4-pin Tape Extensometer Array
41	Tape Extensometer Array 3	2.54	Up to 0.5	4-pin Tape Extensometer Array

TRI-6852-0C3-0

Figure 1-6. Layout of Single Heater Test (Cross-Section)

INTENTIONALLY LEFT BLANK

2. PREDICTIONS

This section provides summations of a variety of reports that predict the thermal, thermomechanical, thermohydrological, and thermochemical processes in the SHT block. These summations are intended to provide an overview of each study. Specifically, four summarized reports document a Thermal-Hydrological-Mechanical Analyses, a Thermal-Hydrologic Analyses, a Thermal-Hydrological Analyses and Air Injection Test, and a Thermal-Chemical Analyses. Detailed discussions and presentation are summarized below.

2.1 SUMMATION OF *PRE-EXPERIMENT THERMAL-HYDROLOGICAL-MECHANICAL ANALYSES FOR THE ESF SINGLE HEATER TEST - PHASE 2* (Sobolik et al., 1996)

2.1.1 Introduction

This document describes pretest analyses performed for the SHT of the ESF Thermal Test in the ESF at Yucca Mountain by Sandia National Laboratories (SNL), under Yucca Mountain Project WBS Number 1.2.3.14.2. The SNL Work Agreement WA-0319 (SNL 1996) defines pre-experiment thermal-hydrological-mechanical (THM) analyses that model the response of the welded tuff in the SHT block to a horizontally-emplaced 4 kW heater. The THM response is determined by measurements of temperature, moisture content, and displacement within the test block. The analyses consist of TH and TM calculations. To the extent possible, input parameters for the calculations were obtained from SHT site-specific information

The SNL Work Agreement WA-0319 details the Quality Assurance procedures that governed the work described in the work agreement. A series of pretest THM analyses of the SHT is documented in Sobolik et. al. (1996) prior to heater activation. A second series of pretest THM analyses, designated Phase 2 analyses, incorporates observations from the first month of testing. The original pretest scenario and the Phase 2 analyses with their scenarios modifications are described below.

2.1.1.1 Original Pretest Analyses

The scenario for the SHT that was modeled by the analyses described in Sobolik et al. (1996) is as follows:

- A SHT facility approximately matching the SHT facility description in Figure 1-5 has been built. The height, width, and depth of the test block are known.

- The heater was assumed to have an output of 4-kW; a diameter of 9.6-cm; and a length of 5-m. The heater was inserted horizontally into the TSw2 rock such that the near end of the heater is 1.9 m from the borehole collar.

- A vapor barrier installed as backing on a thin (6-inch) layer of insulation has been used to cover the three exposed sides of the SHT block to minimize moisture movement out of the rock. The layer of insulation minimizes heat transfer and provides a well defined boundary condition. The vapor barrier and insulation boundaries were modeled such that no heat flux or mass flow exists from the three exposed sides of the SHT block.

- Multi-point borehole extensometers (MPBXs), wire extensometers and anchor pins, thermocouple probes, moisture sensors, a borehole jack, rock bolts and rock bolt load cells have been installed into the rock per the test design as documented CRWMS (1996a).

- The heater is turned on at full power (~4 kW) for a period of one year during which temperature, displacement, and moisture measurements are taken. After one year, the heater is turned off; the measurements are continued for an additional period of six months.

2.1.1.2 Phase 2 Analyses

The following tasks are defined for the Phase 2 analyses to predict the THM response in the SHT block.

Task 1: Thermal-Hydrological Predictions for the SHT

A series of calculations to predict the thermal-hydrological response of the rock to the presence of the heater were performed. The calculations were performed with the multi-phase, three-dimensional thermal-hydrological code TOUGH2 (Pruess, 1991), Version 3.2 in SNL's Software Configuration Management System. These calculations provide temporal predictions of temperature at the in situ locations of the thermocouples, and predictions of liquid saturation in the block over time for comparison with moisture-measuring techniques (neutron probes, electrical resistivity tomography, and humicaps). The predicted temperature histories for the SHT block were used as input to the thermal-mechanical calculations (Task 2).

Task 2: Thermal-Mechanical Predictions for the Single Heater Test

A series of calculations to predict the thermal-mechanical response of the rock to the presence of the heater were performed. The calculations were performed with the finite element nonlinear structural mechanics code JAC3D (Biffle, 1993), Version 6.1-04 in SNL's Software Configuration Management System. These calculations provide temporal predictions of displacements at the in situ locations of the MPBXs and wire extensometers, as well as predictions of changes in stress in the SHT block.

The Phase 2 calculations used the same scenario as the original pretest analyses, with modifications due to additional site-specific information observation from the installation of the SHT. The assumptions used to develop the original pretest thermal-hydrological model were used for the Phase 2 calculations, excepting any changes to those assumptions warranted by additional SHT material property data and as built information from the test. Some of the modifications to the original pretest calculations that have been implemented include the following:

- Temperature predictions were calculated at many times in the heating and cooling phases of the SHT for two heating scenarios (9 months and 12 months).

- Updated bulk and matrix permeability data per in situ measurements in the SHT block have been incorporated.

- A modified boundary condition allowing heat flow through the insulation layers has been implemented.

- A time-averaged value of 3.86 kW of heater power was used in the analyses as opposed to the assumed value of 4 kW in the original pretest analyses.

- A value of in situ liquid saturation of 0.92 taken from SD-9 borehole data was implemented.

2.1.2 Results

TH and TM analyses were performed to predict temperatures, saturations, and displacements in the SHT test block. A comprehensive set of results is presented in Sobolik et al, (1996) are to be used as first-cut predictions of the THM parameters being measured during the SHT experiment. The following general conclusions can be drawn from these analyses:

- A low and a high value of bulk permeability (approximately three orders of magnitude difference) based on in situ measurements were used with the equivalent continuum model in TOUGH2 to predict the thermal-hydrological behavior of the rock. The assumptions of isotropic and homogeneous properties were also included in the model. The model predicts the thermal-hydrological response of the rock to the SHT tests to have a minor dependency on permeability (a maximum difference at any point of about 20°C), and that the resulting isotherms will be essentially axisymmetric around the heater.

- Total head-to-collar displacements along the MPBX's are predicted to be less than three mm. There was no significant difference in the results using low and high bulk permeabilities. Potential opening and closing of fracture apertures may account for displacements of a similar order of magnitude.

2.1.3 Recommendations

During the post-test analysis phase of the SHT it is recommended that:

- Heterogeneous bulk permeability be incorporated based on in situ measurements.

- Alternative conceptual flow models, such as discrete fractures or dual permeability, be evaluated.

- A more representative "wet" thermal conductivity be determined and implemented in the analyses.

- The sensitivity of displacement and stress predictions to rock mass Young's modulus be evaluated.

- Thermal-mechanical calculations implementing different material models (elastic-plastic with strain hardening, discrete fractures with friction, pressure-dependent fracture aperture widths, etc.) be evaluated.

2.2 SUMMATION OF *FORECAST THERMO-HYDROLOGIC RESULTS OF THE SINGLE HEATER TEST* (Lee, 1996)

2.2.1 Introduction

The objective of this report is to present the results of numerical calculations conducted to forecast the thermo-hydrologic (TH) response in the SHT block. The numerical calculations predict temperature and moisture distributions in the SHT block during heating and cooling. Predictions are provided at intervals of one week for the first six weeks, two weeks for the second six weeks, and one month thereafter from the start of both the heating and cooling phases of the test. Two heating scenarios were simulated (9 and 12 months).

The NUFT code (Nitao, 1993) was used to conduct six three-dimensional numerical simulations of the TH behavior in the SHT block. The fractured rock is modeled using an equivalent continuum analysis (e.g., Nitao, 1988). Calculations were conducted for three bulk permeabilities (k_b) which were obtained from air injection measurements:

- Low (3.3 milli-darcy; 3.2×10^{-15} m^2)
- Medium (0.12 darcy; 1.2×10^{-13} m^2)
- High (4.5 darcy; 4.4×10^{-12} m^2)

The low bulk and high bulk permeabilities represent the lower and upper limits from air injection measurements in the SHT block (CRWMS M&O, 1996b) The medium-permeability is the log center of the extreme values. The two heating scenarios were implemented for each of the three bulk permeabilities resulting in a total of six sets of calculations.

2.2.2 Results

Rock temperatures and liquid saturations predicted by the simulations are presented for selected times and locations in Lee (1996). Predictions were generated at intervals of one week for the first six weeks, two weeks for the second six weeks, and one month thereafter from the start of both the heating and cooling phases of the test. The first prediction simulated the 12-month heating option, and the second prediction simulated the 9-month heating option. The results are presented in the form of temperature and liquid saturation profiles, contour and history plots at selected locations. For the medium permeability case, temperatures to 350°C are predicted at the heater borehole after one year of heating. The temperature filed is characterized by steep gradients from the heater borehole axis out to a radius of about 50 cm, after which the gradient begins to flatten. The temperature falls to 200°C at a radius of about 35 cm, and 95°C, the approximate boiling point temperature, at 1.5 m. Although some slightly anomalous decrease in temperature gradient is observed in the neighborhood of the 95°C isotherm, no clear reflux zone is identified.

Temperature predictions for locations closer to the heater are sensitive to bulk permeability. Predicted temperatures close to the heater are significantly higher for the low-permeability case than

for the high-permeability case. At radial distances greater than about 1.7 m from the heater, no significant effect of permeability on temperature is apparent.

The SHT block cools down rapidly once the heater is turned off. For the 12-month heating case, the maximum block temperature is 40°C six months after the heater is turned off. For the 9-month hearing case, the maximum temperature is 65°C one month; and is 45°C three months after the heater is turned off.

A distinct dry-out zone was observed around the heater. The dry-out zone is defined as a zone with liquid saturation less than half the initial value of 0.92. The radius of the dry-out zone was 1.0 m after 9 months of heating, and extended to 1.2 m after 12 months. The dry-out zone for the medium permeability case developed faster and grew slightly larger than the dry-out zones for the other two permeability cases. One limited recondensation was observed, probably because of the high initial liquid saturation.

2.3 SUMMATION OF *FORECAST OF THERMAL-HYDROLOGICAL CONDITIONS AND AIR INJECTION TEST RESULTS OF THE SINGLE HEATER TEST* (Birkholzer and Tsang, 1996)

2.3.1 Introduction

This study models the heating and cooling phase of the SHT with a focus on the TH coupled processes. Also included are simulations of air injection tests which will be performed at different stages of the heating and cooling phase of the SHT.

The most prominent TH response of the rock mass to the heater power output is the initial drying of the rock mass surrounding the heater, the carrying away of moisture in the form of vapor from the heated area, and the subsequent condensation of the vapor in the cooler regions of the rock mass farther away from the single heater. As the power output of the single heater is turned off during the cooling phase, rewetting occurs as water moves back to the vicinity of the heater under the driving force of the capillary suction. These vaporization, drying, condensation and rewetting processes are reflected in the spatial variation and temporal evolution of the liquid saturation in the rock mass, which in turn affect the spatial and time dependence of the air permeability values. In each of the two hydrology boreholes (16 and 18) in the SHT block (see Figures 1-5 and 1-6), four inflatable high-temperature packers have been installed along with pressure and humidity sensors. The above instrumentation allows air injection tests to be performed in different zones in each borehole. The pressure response in each of the eight monitoring sensors to air injection in different zones in both boreholes 16 and 18 measures the integrated air permeability between the injection zone and the pressure monitoring zone.

The numerical simulations (Birkholzer and Tsang, 1996) are performed in three-dimensions with the multi-component, multi-phase flow simulator TOUGH2 (Pruess, 1987 and 1991). The configuration, parameters, initial and boundary conditions of the numerical model are designed to resemble the actual SHT as closely as possible. Furthermore, all site specific characterization data such as laboratory measurements of thermal and hydrological properties of cores from the SHT block, fracture mapping of the drifts in the thermomechanical alcove, in situ air permeability

characterization, and borehole video logs are incorporated into the conceptual model for the numerical simulations of the SHT. Even so, due to the complexity of the multiple physical processes, and uncertainty in key input parameters such as fracture properties, it is to be expected that the simulated results from any one conceptual model will deviate from actual data. Therefore, this report also includes sensitivity studies in both two- and three-dimensions. These sensitivity studies will provide insight as to how individual processes and input parameters affect the TH performance, and will assist the refinement and calibration of the conceptual model.

Air injection tests are to be performed in the hydrology boreholes 16 and 18 throughout the heating and cooling phases of the SHT. Boreholes 16 and 18 are collared on the south wall of the test block in the Thermomechanical Alcove extension. Both boreholes are parallel to and are at approximately the same distance from the west wall: about 4.25 m for 18 and 4.27 m for 16. Borehole 18 is almost horizontal with a length of 4.66 m. Borehole 16 has a slightly positive slope with a length of 5.10 m. The diameter of the boreholes is 7.57 cm. The collar height above floor for boreholes 16 and 18 is 1.56 m and 1.30 m, respectively.

The hydrology boreholes 16 and 18 are each installed with four high-temperature packers. Each packer measures 63.5 cm and the spacing between two packers is 6.35 cm. Behind each packer and in the center of the 6.35 cm interval are housed a high-temperature pressure transducer and a humicap which measures both the relative humidity and the temperature. The top of the first packer P1 is located at a distance of 14 cm and 23 cm respectively from the collar of the boreholes 16 and 18.

An air injection line is associated with each packer so that air can be injected behind each packer. By selectively deflating different packers, various injection zones for each hydrology borehole are formed. The three injection test configurations for either of the two boreholes included in the simulations are: (1) deflate packer P2 and use the air injection line for P1, (2) deflate packer P3 and use the air injection line for P2 , (3) inflate all four packers and use the air injection line for P4. All four packers in the monitoring borehole are always inflated so that pressure response can be monitored in each of the four sensors.

For the TH simulations, the welded tuff is conceptualized as composed of both the matrix continuum with very low permeability, and the fracture continuum with permeability orders of magnitude higher than that of the matrix continuum. Different capillary pressure and relative permeability characteristic curves will be assigned to the matrix and fracture continuum. For the three-dimensional simulations, the matrix and fracture continua are assumed to be in thermodynamic equilibrium, that is, the matrix and fracture are characterized by the same temperature and pressure at all times (Pruess et al., 1990; Bodvarsson & Bandurraga, 1996).

Ambient (preheat) characterization of the SHT block by air injection tests has shown that the local air permeability for the boreholes tested ranges from 5.1 x 10^{-15} m^2 to 5.2 x 10^{-12} m^2 (CRWMS, 1996b). In addition to air injection tests for the entire borehole, some boreholes were also packed off in shorter sections (0.635 m to 3 m), and their local air permeability tested. The air permeability values for all boreholes and straddled sections tested are provided in CRWMS (1996b). The two lowest values of 10^{-16} m^2 are not actual permeability values but, present measurements that show practically impermeable behavior. The median air permeability value is 5.85 x 10^{-14} m^2. Also

shown in CRWMS (1996b) is that in the boreholes with large permeability values, a few discrete fracture zones within the borehole account for all the air flow from the entire borehole.

A further study of the cross borehole interference pressure response of the air injection tests performed prior to turning on the heat reveals the presence of a direct flow path from borehole 11 to boreholes 7, 13, and 12. In other words, an almost identical steady state pressure response is observed in boreholes 7, 13, and 12 as that in borehole 11 when air is injected in borehole 11. While boreholes 11 and 12 both originate from the west face of the test block, boreholes 7 and 13 are collared on the south face of the test block. On the other hand, boreholes 28, 29, 30, and 31 (which are collared also on the west face, and which are situated between boreholes 11 and 12 in very close proximity to borehole 11) register little pressure increase in response to air injection in borehole 11, indicating that they hardly communicate with borehole 11. Fracture mapping and borehole video logs support this observations.

In the three-dimensional simulations, a conceptual model is used for the fracture continuum which is consistent with the interference air injection data. A high-permeability feature with a permeability value of 5.2×10^{-12} m^2 is superposed on the homogeneous background which is given a lower permeability of 5.85×10^{-14} m^2. In addition to this so-called "Base Case", a homogeneous model is studied with the uniform background permeability value assigned to the fracture continuum throughout the SHT block.

2.3.2 Results

Three-dimensional simulations are presented which forecast the TH conditions of the SHT during both the heating and cooling phases. The dominant TH response of the welded fractured tuff to the heater power output is the temperature rise, boiling, vaporization, drying, condensation, and rewetting of the dry-out zones. The manifestation of the above coupled physical processes is the spatial variation and temporal evolution of the liquid saturation in the rock mass. Therefore, these TH processes may be captured by interference air injection tests, provided the air injection and pressure monitoring zones bracket regions in the rock mass where there is significant liquid saturation changes as the SHT progresses.

The configuration of hydrology boreholes (16 and 18) allow the monitoring of the condensation zone, but regrettably not the drying zone close to the heater. Since both the gas pressure build-up as well as relative humidity decrease occur in the dry-out region close to the heater, the eight relative humidity sensors are expected to register approximately 100 percent reading, and the eight pressure transducers will remain practically at ambient pressure conditions during passive testing throughout the heating and cooling period. The only parameter monitored by the sensors in boreholes 16 and 18 that will show changes during the heater test is temperature. The highest predicted temperature is slightly greater than 60°C for sensors 16-4 and 18-4 after one year of heating.

Three-dimensional simulations were performed for air injection tests in boreholes 16 and 18 for nine specific times. Results indicate that the pressure response to air injection is affected by condensation processes and the pressure build-up will be different at different heating and cooling stages of the SHT. Hence, these tests can be very useful to capture the TH evolution of the SHT environment. Additional calculations were carried out for an alternative heating period of nine months. Simulated

results indicate that the change in the TH parameters between nine months and one year of heating is small, and that the TH conditions reflected in the air injection tests at three months after the heater is turned off, whether at nine months or at one year, is very similar. These results suggest that the 9 month, rather than the 12 month heating duration, is probably sufficient.

Because of the uncertainty related to both the complexity of multiple processes, and to various key parameters, three-dimensional simulations were carried out for several plausible conceptual models. For example, although the matrix liquid saturation is 0.92 for the Base Case simulations, it is equally plausible to choose a higher value based on the laboratory analyses of core samples from the SHT area. A higher liquid saturation will promote large changes in the air injection test results at different times of the heater test.

Several other processes and parameters also affect the moisture redistribution in the SHT block from vaporization and condensation, and can produce different air injection results. The sensitivity of the TH conditions to several parameters and model conceptualizations were studied with two-dimensional simulations. Specifically, the processes and parameters were boundary conditions at the alcove wall, mode of vapor diffusion transport, fracture and matrix permeabilities values, and dual continuum conceptualization of the fractured welded tuff.

2.4 SUMMATION OF *THERMOCHEMICAL ANALYSIS OF THE SINGLE HEATER TEST* (Glassley, 1997)

2.4.1 Introduction

During the heating of the SHT block, it is anticipated that vaporized water in the vicinity of the heater will migrate to lower temperature regions and condense. This condensate may enter boreholes either through fracture flow or matrix flow. The water flux and the actual pathway of the condensate remain unknown. Nevertheless, the SHT provides an opportunity to compare predicted and measured water chemistries. This study describes the preliminary attempts to simulate water compositions that may evolve for either fracture flow or matrix flow conditions. The results are compared to measured water compositions from SHT borehole 16, and well J-13.

Since an initial estimate of water composition and mineralogical changes that may occur in the vicinity of the heater is considered important, the most beneficial approach is to bound water chemistry using the most-extreme, but reasonable, conditions. Permeabilities are sufficiently high to allow development of a long-term boiling zone. According to simulations conducted by (Lee, (1996c), a boiling zone may develop at approximately 95°C, and persist for a period of approximately five months, at relatively high permeabilities. These results would apply to all water sampling locations in which high temperature condensate water would be sampled. These results are thus applicable to all sampling locations within the chemistry boreholes. Water sampled that may experience significantly lower temperatures along its flow pathway, would exhibit chemical compositions more dilute, as evident from sensitivity studies in which condensate water-rock interaction was modeled at lower temperature.

The time duration of the simulation covers the maximum anticipated period of boiling. The chemistry of the water expected for shorter time periods (e.g., four months after heating activation),

or for time periods after which the heater has been turned off and the temperature allowed to drop (e.g., 12 months after heating activation, would be more dilute than that obtained for the long term period at high temperature. Hence, the results of the simulations reported in the tables in this report also represent the maximum concentrations expected, regardless of the time periods considered.

Simulations were conducted in which condensate was modeled to flow through tuff for a period of approximately five months under isothermal conditions of 95°C. This represents the most extreme set of conditions, whether for a 4, 9, or 12 month heating period, and is therefore considered applicable for all time periods and temperature conditions in the chemistry boreholes. The code GIMRT was used for the calculations (Steefel and Yabusaki,1995)

The block through which water flow was simulated consisted of Topopah Spring tuff (Tpt) in which two pumice fragments at different locations along the flow path were embedded and a calcite-opal fracture parallel to the flow path were embedded. To be consistent with the geometries of pumiceous material in the Tpt, the pumice fragments were modeled as flattened rectangles with long axes perpendicular to the direction of flow which was assumed to be vertically downward. To evaluate the effects on mineral evolution of location within the flow pathway, one pumice fragment was placed 20 cm from the water inlet location, and the other was placed at approximately 1 m from the water inlet. The overall dimensions for the two-dimensional simulation were approximately 1.5 m along the flow direction, and approximately 1.2 m perpendicular to the flow direction. The fracture was assumed to be 2 cm wide, with a total bulk porosity of 4.5 percent.

Initial simulations were conducted using the indicated surface areas. These values were used as initial estimates, assuming that fracture mineralogy was relatively coarse grained and two-dimensional, and that Tpt mineralogy was very fine grained and spherical. Future simulations will examine the effects of other assumptions related to grain geometry and surface area.

The pumice was assumed to be composed of amorphous silica with an admixture of potassium feldspar and hematite, to account for the high silica rhyolite composition expected for these lithologic materials. Although this admixture provides a reasonable approximation of the composition of high silica rhyolites for these preliminary simulations, future simulations will be conducted with admixtures of materials that more accurately represent these particular siliceous volcanic rocks.

Two infiltration flux conditions (2.667 $mm^3/mm^2/year$ and 26.67 $mm^3/mm^2/year$) were modeled to evaluate the effect of flux on chemistry and mineralogy. The composition of the water was assumed to be virtually distilled water, and at equilibrium with the atmosphere upon initial condensation. There was no control placed on gas composition once water-rock interaction was initiated. Although it was determined that the faster flow rate consistently resulted in lower solute concentrations, those results were not provided in this study.

The 95°C water composition was "cooled" to 25°C using the codes EQ3NR and EQ6. In these simulations it was assumed that equilibrium was maintained with atmospheric CO_2 and O_2 and that appropriate supersaturated or saturated mineral phases precipitated.

2.4.2 Results

For the case considered, the results indicate the composition of water expected to occur within fractures tuff will be significantly more dilute than J-13 well water. The calculated results suggest that the high temperature solutions become supersaturated with respect to quartz, and may precipitate quartz or some other silica polymorph, as the solutions cool. This substantially lowers total Si concentration in solution which is the only significant difference between the 95°C and 25°C water compositions.

The computed water compositions do not closely match the water sampled from borehole 16. This is likely from inappropriate assumptions about effective mineral surface areas, and possibly due to supersaturation of the sampled water resulting from kinetic inhibition of precipitate nucleation sites. Future simulations will be conducted using different surface areas, and constraining secondary mineral precipitation, to determine which set of conditions would produce the best match to borehole 16 water composition.

The secondary mineralogy that may develop along the flow pathways is shown in Glassley (1997b). At the entrance point, where condensate first contacts the rock/fracture system, kaolinite, pyrophyllite, and clinoptilolite form as secondary phases. The clays also occur at elevated levels downstream from the pumice pieces. Quartz occurs as a secondary phase through out the flow field, while the clinoptilolite only develops at significant levels within the Tpt. For all cases, however, secondary mineral development accounts for less than 0.2 percent of the rock volume at any single location. Under these conditions, detection of secondary phase development will be difficult in the SHT block. Future simulations with different effective surface areas will allow refinement of the expected abundance and distribution of the secondary minerals.

3. MEASUREMENTS

This section provides summations of several reports that document initial measurements from the SHT. Most of the measured data is from the initial 100 days after heater activation. The measured data pertains to the four processes under investigation; namely, thermal, mechanical, hydrological, and chemical. Some reports provide overlapping data, but most pertain to unique sets of measurements. The measurement reports are summarized with the intent of providing an adequate overview of the subject matter. Specifically, six subsections discuss in the following types of measurements:

- Thermal-Mechanical
- Gas Permeability
- Neutron Logging
- Electrical Resistance Topography
- Infrared Imaging
- Physical and Chemical (Borehole 16-4 Water)

Detailed presentation of the data has been intentionally omitted since that is the domain of each respective report.

3.1 SUMMATION OF *EVALUATE MEASUREMENTS AND ANALYZE SINGLE HEATER TEST - FIRST QUARTER RESULTS (8/30/96 THROUGH 11/30/96)* (SNL, 1997)

3.1.1 Introduction

A brief description of each instrument/equipment was developed into a Technical Data Information Form (TDIF) as documented in SNL (1997) in which the data tracking number (DTN) is SNF35110695001.003.

This report presents measurements of heater power, temperature, rock displacement, rock mass modulus, and rock bolt loads. These measurements primarily represent SNL-installed gages and activities; however, temperature data from LLNL-installed RTDs are also presented. Selected data from measurements of heater power and temperature are presented first, followed by displacement, borehole jacking (rock mass modulus), rock bolt load, and finally miscellaneous measurements and activities. Figures summarizing plan and SHT block surface views of gage locations are presented for each type of measurement. Data are presented through November 30, 1996. Specific details regarding serial numbers, calibration records, etc. can be found in the Scientific Notebook covering this work.

3.1.2 Heater Power

The heater assembly for the SHT consists of two single-ended 4000 watt heating elements centered in a 5.4-cm (2.125-in.) diameter copper tube with a copper end cap at the bottom end. The two heating elements are contained in a nominally 2.5-cm (1-in.) diameter carbon steel inner casing. The heating elements are made of nicrome and are each 5-m long with a 180° bend at the bottom end. The design of the SHT heater allows for one of the heating elements to act as a secondary heating source in the event that the other fails, or if additional heat must be added to the rock. The heater includes a control loop which allows for automatic switching from the primary element to the secondary element if the heater power drops below a prescribed set point. Currently, on one of the heating elements is operating.

The heater power, voltage, and current were monitored using a Magtrol power monitor. The SHT called for the heater power to be nominally 4000 watts for a period of 9-12 months, followed by a cool down period where the heater is off completely. The heater power data are illustrated in Figure 3-1. Tabulated data are presented in SNL (1997). Power was applied to the heater starting on August 26, 1996 at 18:30:30 according to the clock in the data logger, which corresponds to approximately 13:30:30 Pacific Daylight Time. Time zero in Figure 3-1 corresponds to the time of heater activation. Between the time of activation and November 30, 1996 but omitting anomalous data intervals discussed in SNL (1997), the heater power output averaged about 3841 watts. Naturally, the heater power is influenced by other electrical activities in the tunnel such as tunnel boring machine (TBM) operation. Spikes in heater power have occurred five times since the heater was activated. These large fluctuations in heater power do not significantly influence the temperature distribution in the SHT block because they are infrequent and occur over brief time internally.

3.1.3 Temperature

The TC probes used in the SHT consist of Type-K thermocouples enclosed within 304 stainless steel, 0.64-cm (0.25-in.), diameter sheaths that were manufactured by STI in Houston, TX. The thermocouples within the sheaths are insulated from each other with magnesium oxide. The TC probes were installed in seven boreholes in the rock mass around the heater to monitor temperature changes away from the heater. Three additional TC probes were installed on the top, side, and bottom of the heater canister to monitor heater surface temperatures. Five of the boreholes were drilled roughly parallel to the heater axis to a depth slightly exceeding the planned heater installation depth. Within these five boreholes, probes TMA-TC-1, TMA-TC-2, TMA-TC-3, TMA-TC-4, and TMA-TC-5 were located at nominal radial distances from the heater borehole of 0.33 m, 0.66 m, and 1.48 m, corresponding with the numerically-predicted, maximum-temperature isotherms of 200°C, 150°C, and 100°C respectively (TRW, 1996a).

Within each of these five boreholes, two TC probes were installed. Two probes were required during test planning because it was feared that the drift width was too narrow (about 5.5 m) to allow installation of 8 m long TC probes. Therefore, for each of these boreholes, two probes were used: one about 6 m long with 10 Type-K thermocouple junctions spaced along its length and one about 2 m long with five Type-K thermocouple junctions spaced along its length. The other two TC probes (TMA-TC-6 and TMA-TC-7) were drilled perpendicular to the heater borehole from the Observation

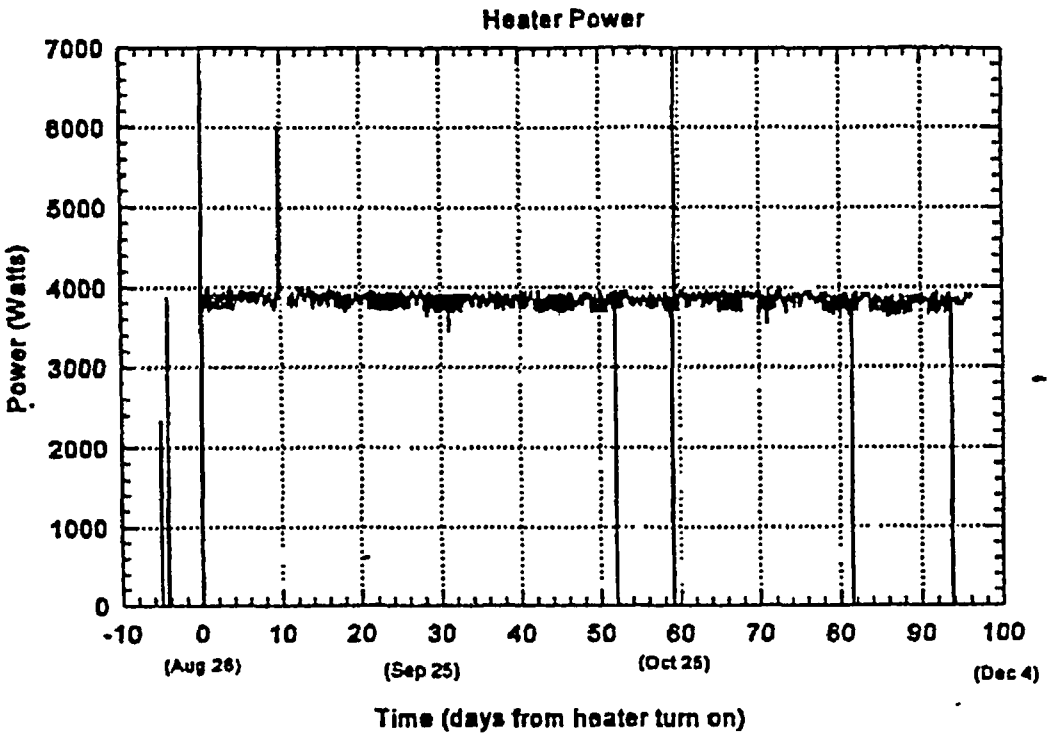

Figure 3-1. Chronology of Heater Power During the Initial 100 days of the SHT

Drift and the Thermomechanical Alcove Extension. Each of these two boreholes includes a single TC probe with 10 Type-K thermocouple junctions spaced along its length. The locations of the individual thermocouple junctions were determined from the survey and corrected borehole collar coordinates, from the field notes for installation (e.g., installed depth to various points on the probes), and from the manufacturers' and SNL specifications for the probes.

Temperatures are also being measured on each of the free surfaces of the SHT block using individual Type-K thermocouple junctions. Twelve individual thermocouples were installed on each face of the SHT block. The location for each of these thermocouples was measured manually in the field using a metric tape measure. Temperatures are also being measured between the two layers of insulation on each of the three free surfaces of the SHT block using individual thermistors. Five individual thermistors were installed between the layers of insulation on each face of the SHT block. The location for each thermistor was measured manually in the field using a metric tape measure. The locations of the 319 temperature sensors are cited in Appendix A. Of the 319 temperature

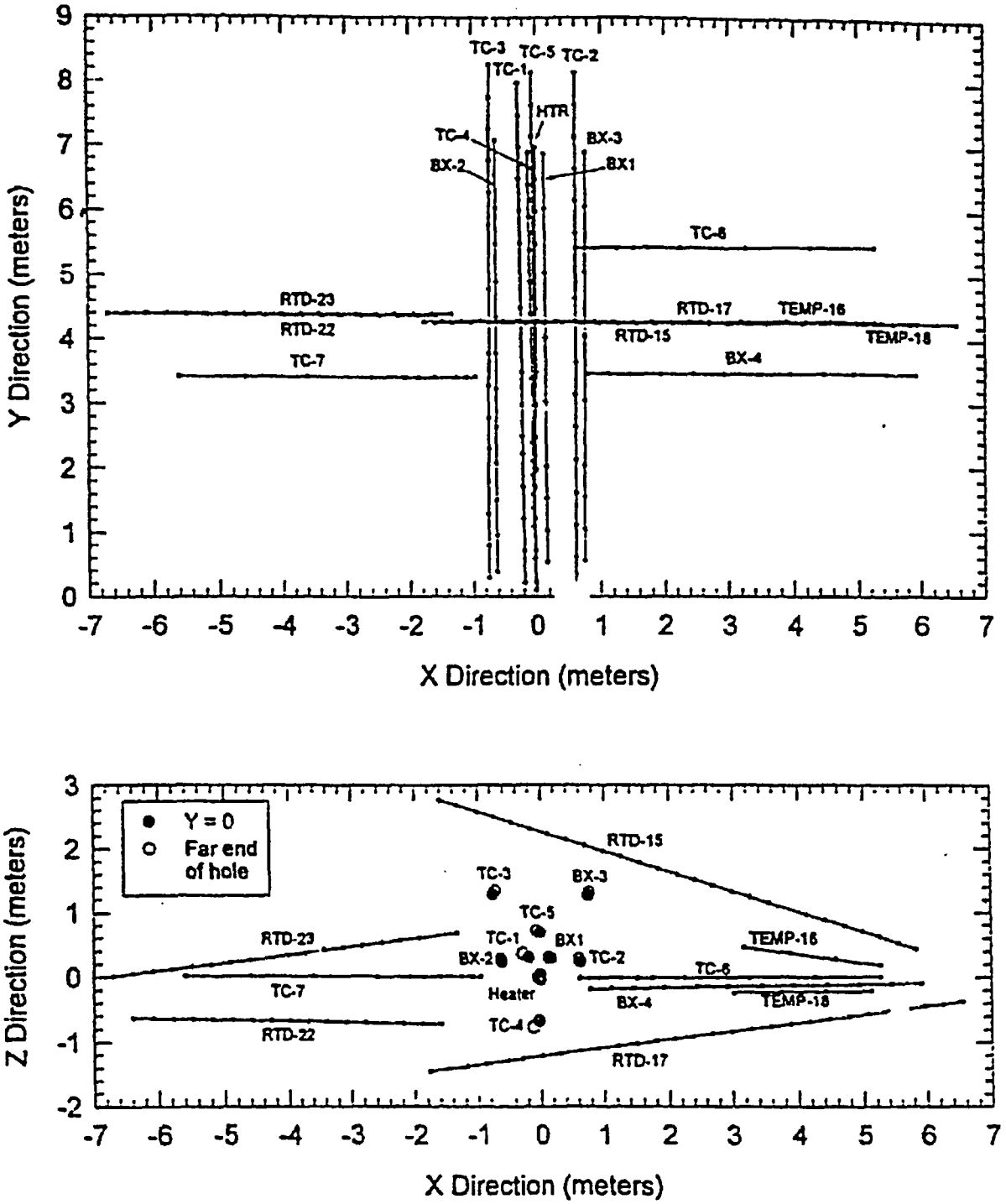

Figure 3-2. Map and Cross-section Views of the SHT Block Showing the Locations of Interior Temperature Gages

sensors, nine have malfunctions and probably will not provide any more data. Their locations are illustrated in Figure 3-2.

For the purpose of creating summary data plots, the 310 reliable gages were divided into 27 sets. Each set contains the gages from a single probe, a single borehole, or in the case of the surface thermocouples and the thermistors in the surface insulation, data from a particular rock face. Figures 3-3 and 3-4 provide an example illustration from SNL (1997) of data from TMA-TC-1. The curves in Figures 3-3 illustrate (1) the median daily temperature as a function of spatial position along the direction parallel to the axis of the heater every three days; and (2) the median daily temperature as a function of time for each temperature gage in a set.

The response of TMA-BX-1 (Figures 3-3 and 3-4) is quite different from that of TMA-TC-1 (SNL, 1997) even though they are both the same radial distances from the heater. The most significant differences occur during the time interval from day-9 to day-18, during which time the temperatures in the borehole were increasing through the boiling point of water. During this time, and particularly on day 10, the spatial temperature distribution in TMA-BX-1 between Y=2 m and Y=6 m was virtually isothermal at about 96°C. It is likely that this results because TMA-BX-1 is installed in an open borehole. As the temperatures in the surrounding rock passed through the boiling point, vapor phase heat transport within the borehole created the observed isothermal conditions in the borehole, which may not accurately reflect the temperature in the adjacent rock. TMA-TC-1 did not respond in this manner because the temperature sensors are grouted in the borehole and there is no open borehole in which vapor phase transport could occur. After all water in the rock adjacent to the TMA-BX-1 had evaporated, the convective heat transfer in the borehole was reduced, and the temperature response returned to a conduction-dominated regime. Another noteworthy feature about TMA-BX-1 is that the spatial temperature distribution is significantly asymmetric about the center of the heater.

3.1.4 Displacement

Displacements were measured both within and on the surfaces of the SHT block. These measurements support numerical model evaluations related to TMH coupling as well as provide data for determination of rock mass thermal expansion. All measured displacements follow the convention of extension being positive.

Four boreholes were instrumented with multiple-point borehole extensometers (MPBXs): three boreholes drilled parallel to the heater axis and one borehole drilled perpendicular to the heater axis. The MPBXs include six of seven anchors spaced along the length of the borehole. Displacements are measured using high temperature linear variable displacement transformers (LVDTs) for BX-2 only and vibrating wire displacement transducers for BX-1, 3, and 4. For three of the boreholes, GeoKon C-ring 6-anchor MPBXs were used with carbon fiber extension rods transmitting the displacements of each of the six anchors to the head, which was fixed into the borehole collar. The displacements measured for each of the anchors is expressed as the relative displacement between the anchor and the borehole collar (head). BX-2 is a seven-anchor Roctest BOF-X extensometer with screw-type mechanical anchors between which a high temperature LVDT was installed.

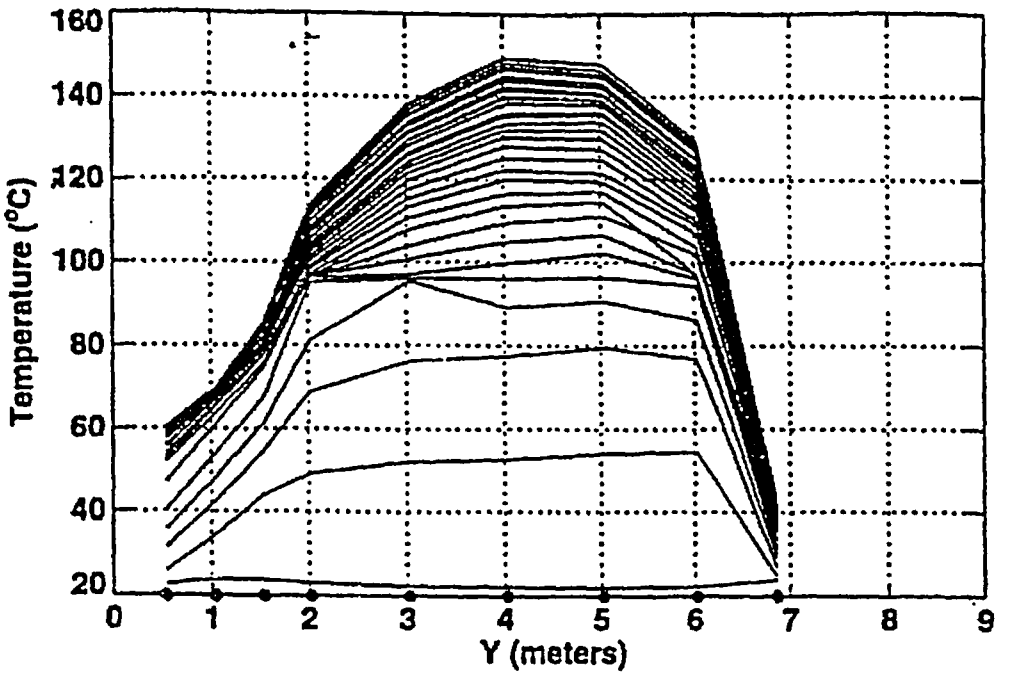

Figure 3-3. Representative Temperature Profile for Thermocouple Designated as TMA-BX-1

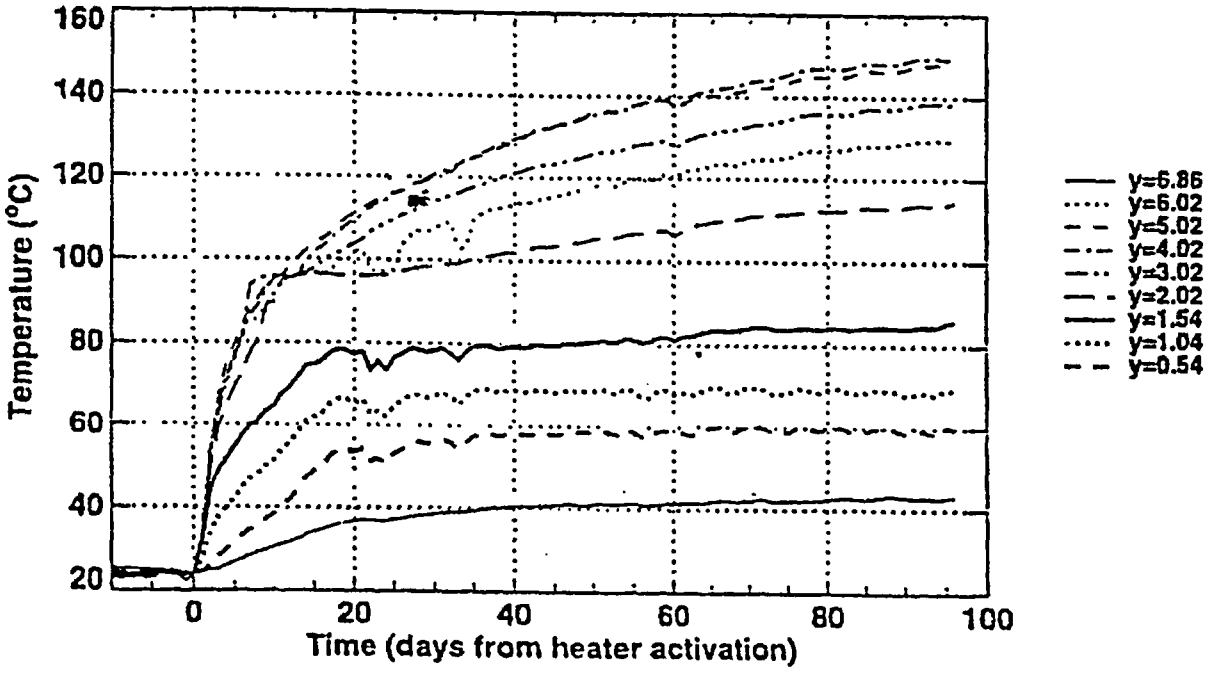

Figure 3-4. Temperature History for the Nine Sensors of Thermocouple Probe TMA-BX-1

Extension rods between the LVDTs and adjacent anchors were constructed from Invar tubing. The displacements measured for each of the LVDTs represent the discrete displacements between each set of adjacent anchors. Total displacement along the BOF-X borehole is the sum of the displacements measured between each set of adjacent anchors. Temperature measurements were made along the length of each MPBX to provide temperature compensation for thermal expansion effects. The locations of the anchors and individual thermocouple junctions were determined from the survey and corrected borehole collar coordinates, from the field notes for installation (e.g., installed depth to various anchors and points on the MPBXs), and from the manufacturers' and SNL specifications for the MPBXs.

Wire extensometers and tape extensometer pins were installed on the three free surfaces of the SHT block. The wire extensometers consist of spring-loaded linear potentiometers mounted on brackets welded to steel rebar segments. These segments are grouted into the rock near the top of the SHT block at six locations (two on each of the three free surfaces of the SHT block). The wires are then stretched roughly vertically downward to another anchor located near the base of the SHT block. Tape extensometer pins are also located roughly along the midpoints of each of the six vertical lines defined by the wire extensometers. These six tape extensometer stations include six pins on the SHT block and six pins on the opposite ribs. As-built locations for each of these gages were determined from tape and level measurements referenced to known points of reference. Also, the rock surfaces represented by each of the three free surfaces were simplified to be represented by planar surfaces for numerical modeling efforts. Because the pins are mounted in shallow holes, they can be strongly influenced by movement of discrete blocks near the surface. The data from these measurements should be used only for qualitative purposes.

Figures 3-5 and 3-6 show the locations of the MPBX boreholes and anchor locations. The figures also show wire and tape extensometer pin locations on the SHT block. MPBX-1, MPBX-2, and MPBX-3 are located in boreholes drilled parallel to the heater from the TMA (Figure 3-6, west face of the SHT block). Two wire and tape extensometer stations are located on each of the three free surfaces of the SHT block. On the west face, station locations are WX-1, WX-2, WXM-1, and WXM-2. The designator "M" in WXM describes manual (tape extensometer) pin locations. On the south face of the SHT block (TMA- extension), MPBX-4 is located in a borehole drilled perpendicular to the heater. WX-3, WX-4, WXM-3, and WXM-4 wire and tape extensometer stations are located on the south face. Wire and tape extensometer stations WX-5, WX-6, WXM-5, and WXM-6 are located on the north face of the SHT block along the Observation Drift.

An example of the displacement measurements through November 30, 1996 for the MPBXs is presented in Figure 3-7. Figure 3-7 shows displacement data for TMA-BX-3, which is located approximately 1.5 m above and to the south of the heater The y-coordinates for each of the anchors are spaced approximately 1 m apart from the bottom of the borehole (anchor BX-3-1 at 6.887 m to anchor BX-3-6 at 2.047 m along the y-coordinate axis). The data from TMA-BX-3 exhibit very consistent results, with the deepest anchor (BX-3-1) displacing the most and the anchor nearest the collar (BX-3-6) displacing the least. The data presented in Figure 3-7 show an increase in gage length (extension) for all anchor positions through about the first 70 days. After 70 days, anchors BX-3-3, BX-3-4, and BX-3-5 exhibit a gradual decrease in gage length. Total uncorrected

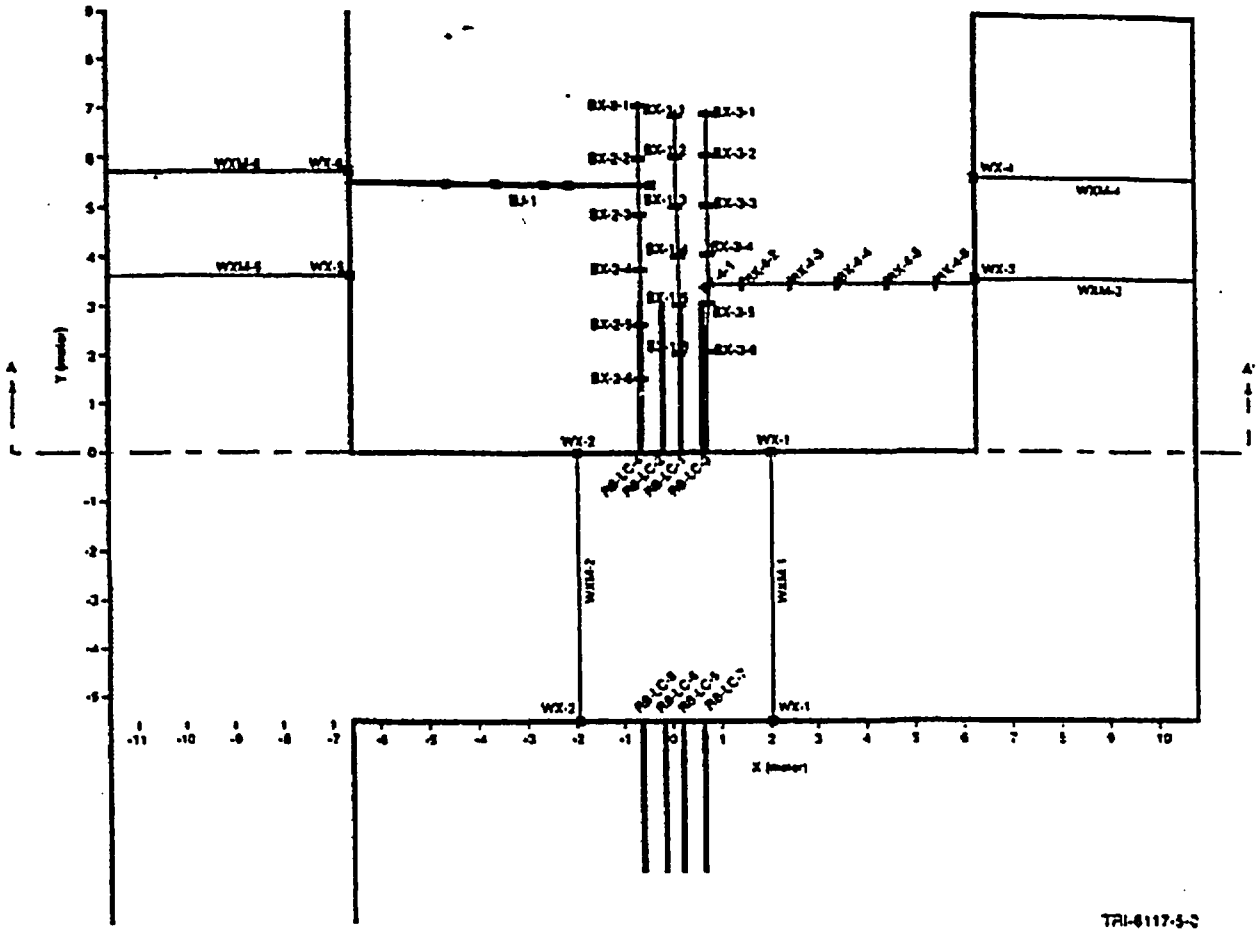

Figure 3-5. Plan View Showing Locations of Boreholes, MPBX Anchors, Wire Extensometers, Rock Bolt Load Cells, Borehole Jack, and Tape Extensometers in the SHT Block

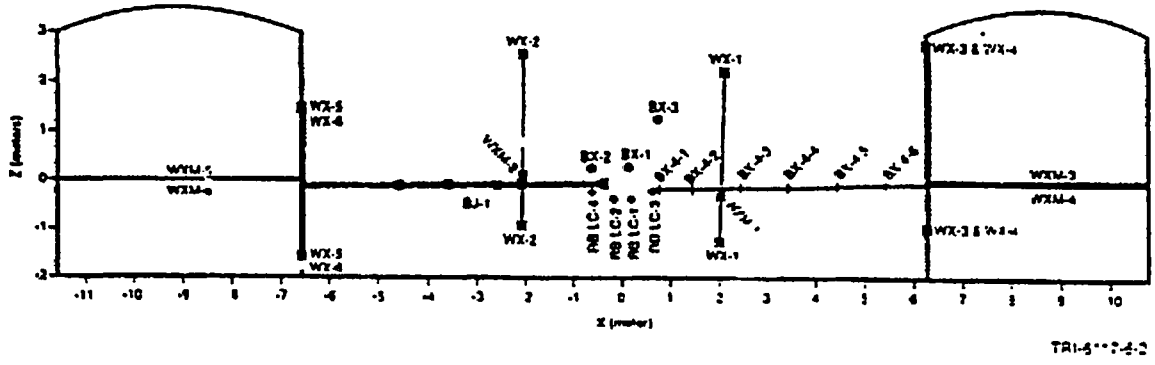

Figure 3-6. Cross-section Showing Locations of Boreholes, MPBX Anchors, Wire Extensometers, Rock Bolt Load Cells, Borehole Jack, and Tape Extensometers in the SHT Block

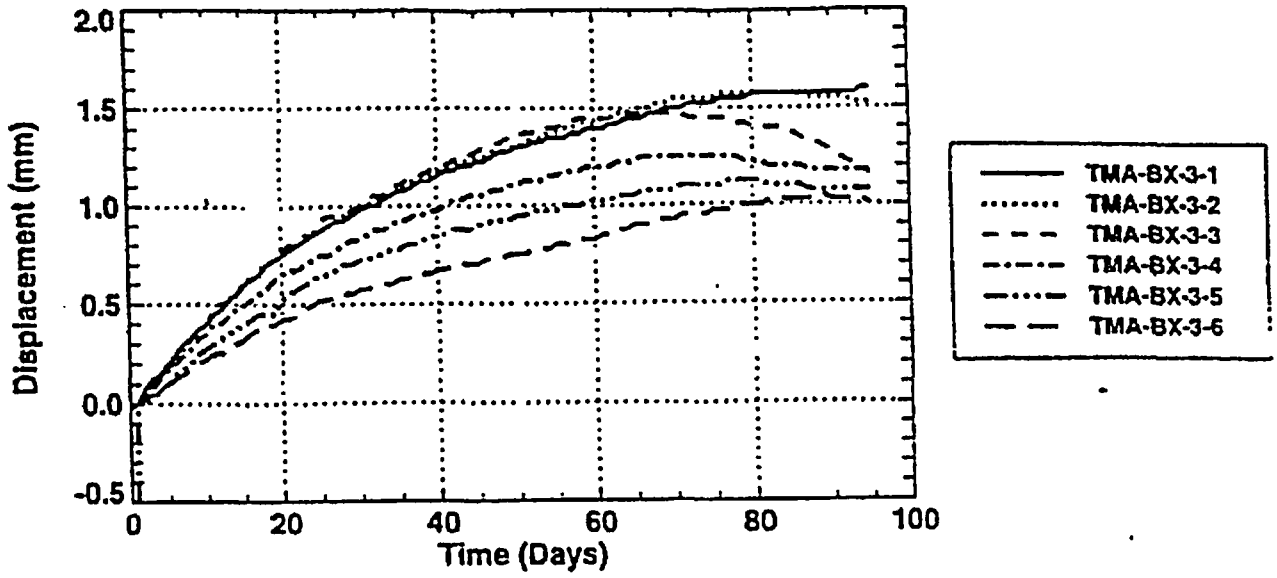

Figure 3-7. Displacement History for ESF-TMA-MPBX-3 (Uncorrected for Thermal Expansion of Rods; Extension Positive)

displacements for all anchors are small, less than 2 mm. It should be expected that anchor BX-3-1 would exhibit the greatest displacement and BX-3-6 the least over any time period because they represent the longest and shortest gage lengths, respectively. It is not yet known what caused the change in displacement sign for anchors BX-3-3, BX-3-4, and BX-3-5. The change in slope of most of the anchor responses after about 70 days may be the result of matrix thermal expansion closing existing fractures, thus limiting additional thermally driven displacements until a greater volume of rock is heated.

Corrections have not been made for thermal expansion of the extension rods for the data presented in Figure 3-7. For TMA-BX-3, nine temperature measurements were made, one on each of the six anchors and three on the extension rods near the collar. The thermal expansion coefficient for carbon fiber is 1.48 ppm/°C, GeoKon (1997). A preliminary estimate of the expansion of the extension rods can be made from the measured temperature changes from startup, the thermal expansion coefficient of carbon fiber, and the lengths of extension rod. The measured displacements reported in Figure 3-7 will be corrected for thermal expansion. For each anchor, the thermal expansion of the extension rod is determined by integrating the temperatures from the anchor to the collar.

Naturally, the largest thermal correction is for anchor BX-3-1 because it includes the greatest length of extension rod. The thermal expansion corrections are relatively small. The carbon fiber is a well-characterized, uniform material with linear response over the temperature range of interest. The thermal correction for BX-3 rod expansion is straightforward and provides reasonable, realistic

displacements. The response of TMA-BX-3 will continue to be monitored closely to determine whether the trends observed through November 30, 1996 continue. The data will be reevaluated in future data transmittals.

Wire and tape extensometer pins were placed on the three free surfaces of the SHT. These surface displacements are intended to augment the displacement data collected from the MPBXs and to provide qualitative "control" of the SHT free surfaces to support future modeling efforts. Because the measurements are made from short pins installed near the rock surface, they can be influenced by discrete block movement. Example data from the WX-1 wire extensometer is shown graphically in Figure 3-8. The data show general extension of about 0.2 mm through November 30, 1996, although the displacements are relatively erratic. This type of behavior can be expected from shallow-mounted surface pins. The response of WX-1 will continue to be monitored closely to determine whether the trends observed through November 30, 1996 continue. The data will be reevaluated in future data transmittals. Discussion of the other informational measurements is provided in SNL (1997).

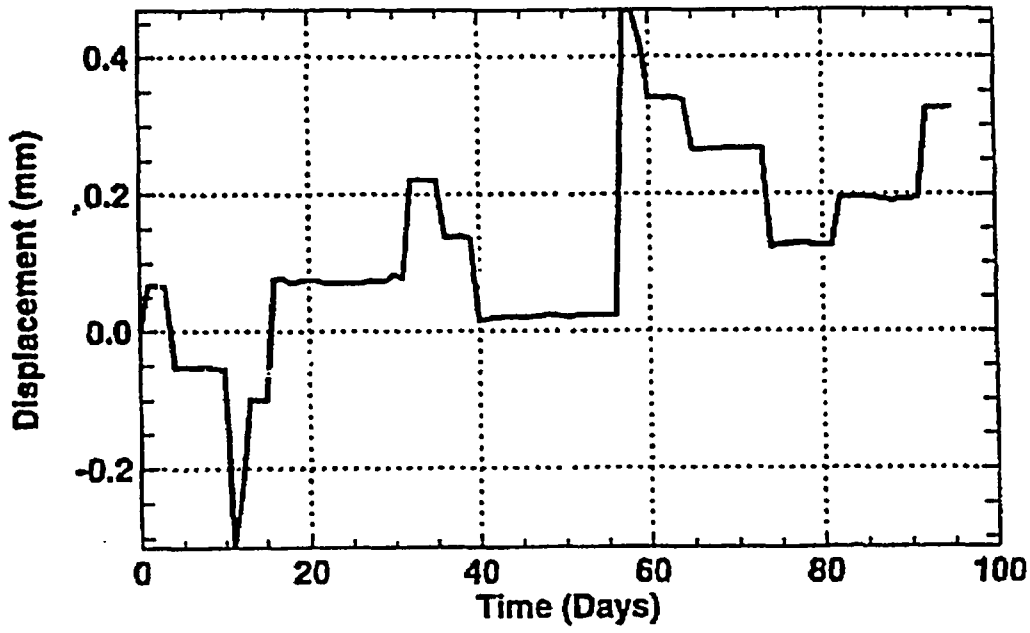

Figure 3-8. Displacement History for Wire Extensometer ESF-TMA-WX-1 (Extension Positive)

3.1.5 Borehole Jack

A single borehole (ESF-TMA-BJ-1) was drilled roughly horizontal and perpendicular to the SHT heater borehole (see Figures 3-5 and 3-6) for operation of the NX borehole jack (Goodman jack). This nonpermanent borehole instrument is periodically inserted into the borehole and pressurized at various distances along the hole. Jack pressure and loading platen displacements are monitored, and rock mass modulus is determined from the pressure/displacement curve. For the SHT, Goodman jack tests were conducted three times during the first three months of heating, before heater activities (August 26, 1996), on October 10, 1996 and November 26, 1996. Temperatures were measured in the borehole prior to insertion of the jack using a portable Type-K thermocouple probe at various points, and by manually taking temperature readings using a hand-held thermocouple reader. Jacking tests were run along the borehole at depths (from the collar) of 2.0 m, 3.0 m, 4.0 m, 4.51 m, and 6.2 m, although not all locations were tested on each of the dates. All borehole jack testing followed ASTM 4971-89 (Reapproved 1994) (ASTM, 1996) with minor exceptions. These exceptions include performing multiple loadings on only 50 percent of the ambient (preheating) runs. No multiple loadings were conducted during the October 10, 1996 or the November 26, 1996 tests to limit thermal effects on the jack.

Borehole ESF-TMA-BJ-1, located about 5.5 m from the front (west) face of the SHT block, is collared in the Observation Drift and is oriented toward the heater. As such, the borehole is expected to exhibit a transient temperature gradient from the bottom to the collar as the test is conducted. This allows for evaluation of the effect (if any) of increased temperature on the measured rock mass modulus.

The NX-borehole jack consists of two hydraulically activated steel loading platens approximately 20.3 cm long, which apply a unidirectional load to a nominal 7.62-cm diameter borehole wall. The maximum jack pressure is 69 MPa, and the maximum platen displacement is 0.63 cm. The total displacement of both platens is 1.27 cm, with total jack diameter of 8.25 cm. Platen displacement is measured using LVDTs (one for each platen). The platens pressurize 90° of the borehole wall on each side. Jack pressure is applied using an Enerpak hand pump. Typically, the jack is pressurized to 34.5 MPa, then to 55.2 MPa, then back to zero, with LVDT readings recorded during both loading and unloading.

The historical use of the borehole jack has shown that corrections must be taken into consideration for the mismatch between borehole and platen radii, longitudinal bending of the platens, and tensile cracking of the intact rock or opening of existing fractures. The use and interpretation of the borehole jack is discussed at length in several references: ASTM (1996), Heuze and Amadei (1985), and elsewhere. The jack is inserted in the borehole and platens are slowly expanded until the pressure just begins to rise. The resulting LVDT readings represent the initial borehole diameter and are used for calculations of borehole wall displacement under pressure. The jack pressure is increased in increments to the desired maximum pressure and then decreased in similar increments. Because of the necessary data corrections, as described in ASTM D4971-89, the calculated minimum pressure to achieve "full platen contact" based on the approximate borehole diameter (7.57 to 7.90 cm.) was about 21 MPa. For the tests conducted on August 26, 1996 the maximum pressure applied to the rock by the jack was limited to about 34.5 MPa. For all subsequent tests, the maximum pressure was limited to about 55 MPa. Also, it should be noted that Equation 1 in ASTM

D4971-89 is incorrect. Equation 6 from Heuze and Amadei (1985) was used to determine the calculated modulus.

The calculated rock mass moduli are given in Table 3-1 along with the rock temperature at the time of the test. The results from the borehole jack testing show that the measured rock mass modulus ranges from about 3 to 10 GPa. These values are considerably less than the intact modulus of about 32.4 GPa measured on intact samples of the Topopah Spring Welded Tuff and from the rock mass value of about 30 GPa estimated using the Rock Mass Rating (RMR) (CRWMS M&O, 1996a) and the technique outlined in Serafim and Periera (1983). It is not known what impact these lower moduli have on the overall SHT block performance; however, the potential impact will be evaluated in upcoming evaluations. The data presented in Table 3-2 include italicized results in which the two LVDT readings (far and near) differ by slightly greater than 0.02 in. at the maximum test pressure. According to ASTM D4971-89, these data should be discarded because of uneven loading. The fractured nature of the rock surrounding the borehole made it difficult in some cases to "set" the Goodman jack at those locations. However, the data presented represent only slight deviation from the ASTM D4971 criteria and are presented to qualitatively assess modulus difference along borehole BJ-1. The italicized data should not be used in calculations requiring rock mass modulus.

Table 3-1. Estimated Rock Mass Modulus in Borehole TMA-BJ-1 Using the Goodman Jack

Date	Distance from Collar				
	2.0 m	3.0 m	4.0 m	4.51 m	6.2 m
	Rock Mass Modulus GPA (Temp °C				
8/26/96	*6.9 (25)*	3.71 (25)	No test	No test	No test
10/10/96	10.3 (27.5)	10.3 (27.7)	*8.3 (30.2)*	6.0 (34)	No test
11/26/96	*Results Discarded (31.1)*	10.2 (35.9)	*5.71 (46.4)*	*5.01 (55.4)*	8.4 (141.8)

Note: Italicized calculated moduli are based on field data in which the difference between the two Goodman jack LVDT readings slightly exceeded the limits set in ASTM D4971-89. The fractured nature of the rock made setting the jack difficult.

Table 3-2. Decrease in Rock Bolt Load Cell Readings (8/26/96 – 11/30/96)

Gage	RBLC-1	RBLC-2	RBLC-3	RBLC-4	RBLC-5	RBLC-6	RBLC-7	RBLC-8
Change in Load	1254 lb.	299 lb.	166 lb.	197 lb.	1889 lb.	42 lb.	42 lb.	270 lb.
% Change	5.53	2.01	0.74	1.18	0.73	0.29	0.85	1.60
Location	hot side	hot side	hot side	hot side	Ambient side	Ambient side	Ambient side	Ambient side
	Average % change = 2.37				Average % change = 0.87			

The rock mass modulus information presented in Table 3-1 do not exhibit identifiable trends either spatially, temporally, or thermally. The data base is insufficient to draw specific conclusions; however, it is clear that the measured modulii are all about 10 GPa or less. The reported values could be the result of the relatively small volume of rock energized (~0.15 m^3) and as such could be overly influenced by nearby fractures. Additional tests will be conducted along the length of borehole BJ-1. The data will be evaluated to determine if the change in temperature influences rock mass modulus. Measurements will continue to be made on a periodic basis and will be presented in future data evaluations.

3.1.6 Rock Bolt Load Cells

Eight rock bolt load cells were installed on Williams B7X Hollow Core rock bolts as part of the SHT. The objective is to evaluate qualitatively the effects of elevated temperature on bolt performance by (1) monitoring load changes during the test, (2) post-test evaluations of the bolt/grout/rock interface, and (3) pull testing selected bolts to failure after heating and subsequent cooling. Each rock bolt included one vibrating wire load cell (load washer) that was installed between cover plates and adjustable angled washers. This entire assembly was bolted to the Williams bolt on the cold side of the insulation

Four of the rock bolts were installed on the heated side of the Thermomechanical Alcove below the level of the heater. Another four rock bolts were installed on the opposite cold side of the Thermomechanical Alcove. The rock bolts and load cells were installed during July 1996. Initial readings were taken using a hand-held GeoKon readout box, prior to connection to the data acquisition system (DAS). The load cells each contain three strain gages, and the total load acting on the cell is calculated by averaging the measurements from all three.

The locations of the rock bolts instrumented with rock bolt load cells (RBLCs) are shown in Figures 3-5 and 3-6. Four RBLCs were installed on the heated side of the west face of the SHT block (RB-1, RB-2, RB-3, and RB-4), and four were installed on the opposite ambient side of the Thermomechanical Alcove (RB-5, RB-6, RB-7, and RB-8).

The load cells are actually washers that fit over the rock bolts and are held in place by flat steel plates on either end and loaded with a nut. Each wedge washer includes three strain gages whose outputs must be averaged. Each RBLC was torqued to an initial load. Also, each of the three strain gages in each RBLC was monitored during torquing to maintain relatively uniform loading. If the loading was nonuniform, the wedge washers were adjusted and the nut retorqued. The important consideration in evaluating the rock bolt performance is the change in load from day zero, as well as the difference between the response of the heated versus the ambient rock bolts.

The data shown in Table 3-2 show a general decline in load measured in all the RBLCs. Although measurable, the decreases are all less than 6 percent of the initial load. The average percent decrease for the ambient RBLCs is 0.87 percent, whereas the average decrease for the heated RBLCs is 2.37 percent, although this decrease is most influenced by the 5.53 percent decrease observed in RB-LC-1. Also, the two highest decreases are seen in the RBLCs that are nearest the heater (RB-1 and RB-2) and are therefore the hottest. It is too early in the testing to reach final conclusions; however,

the RBLCs will continue to be monitored, particularly the heated side. Newly evaluated data will be documented in future data transmittals.

3.1.7 Miscellaneous Instrumentation

Miscellaneous instrumentation and equipment include power, current, and voltage monitors; air temperature (ambient) monitors in the Thermomechanical Alcove Extension, Thermomechanical Alcove, and Observation drift; and insulation and vapor barrier installed on the three free surfaces of the SHT block.

Power, current, and voltage (EMF) were monitored continuously using a Magtrol power monitor (SNL, 1997). The temperatures of the ambient air within the testing facility were measured using Type-K thermocouples. The ambient temperatures, heater power, heater current, and heater voltage were recorded on the DAS. In addition, two 7.6-cm thick layers of insulation were installed on the three vertical surfaces of the SHT block. This insulation is aluminum foil-backed fiberglass insulation on the inner layer (which serves as the vapor barrier), and vinyl-backed fiberglass insulation for the outer layer. The insulation was attached to the rock surface using short copper "nails" attached to the rock surfaces at approximately regular intervals using high-temperature adhesive.

3.1.8 Performance of Measuring Systems

An important consideration for long-term thermal testing at Yucca Mountain is the reliability of the installed measurement systems. It is anticipated that some gages will fail or produce unreliable data during tests conducted in harsh thermal environments for extended periods of time. Identification of unreliable measurement systems is necessary for evaluation of data and for planning future tests. This section summarizes the failed, unreliable, and suspect thermomechanical gages and measurement systems associated with the SHT, through November 30, 1996. Table 3-3 presents failed, unreliable, and suspect thermomechanical gages installed in the SHT based on data through November 30, 1996.

Table 3-3. Unreliable Temperature Gages from the SHT Block

Temperature Gage	Reason for Omission
TMA-H-1-TCE-4	No data after heater activation
TMA-TC-2A-4	Erratic temperature readings
TMA-TC-4A-1	Eratic temperature readings
TMA-BX-3-TC-9	Erratic temperature readings; no data after day 90
TMA-BX-4-TC-3	No data in data file (TC extension wire broken during installation)
TMA-RTD-15-20	Erratic temperature readings
TMA-RTD-15-23	Erratic temperature readings
TMA-RTD-23-11	Erratic temperature readings
TMA-TEMP-16-4	Erratic temperature readings
TMA-BX-1-2	Suspect displacement (unexpected decrease)
TMA-BX-1-6	Suspect displacement (unexpected decrease)

The total number of failed, unreliable, and suspect thermomechanical measurement systems (11 gages) identified in the SHT through November 30, 1996 represent about three percent of the measurement systems installed. This represents quite a small percentage for such an experiment, although it is too early in the test to fully assess the performance of the measurement systems. Monitoring of the measuring systems will continue and their reliability documented in future reports.

3.2 SUMMATION OF *FIRST QUARTER RESULTS OF MEASUREMENTS IN HYDROLOGY HOLES IN SINGLE HEATER TEST AREA IN THE ESF* (Freifeld and Tsang, 1997)

3.2.1 Introduction

...al field measurements were performed with qualified personnel and calibrated equipment under the LBNL QA program. All data presented are to be considered qualified data. The data files are referenced with the data tracking number LB9701001231?2.001. A TDIF was developed for the formal submission of this measured data as documented in LBNL (Freifeld and Tsang, 1997)

Measurements of changes in gas permeability during heating and cooling of the SHT block can help to determine the extent of moisture movement caused by the thermal load applied. Constant mass flux air injection tests, in addition to the continuous monitoring of relative humidity and temperature, are being conducted in the SHT block in boreholes 16 and 18. The results reveal the TH response of the SHT block to heating, and give insight into the hydrologic response of the host rock to an emplaced waste package. This report contains a preliminary analysis of the data collected during air injection tests conducted just prior to and three months after heating was started in the SHT block.

3.2.2 Procedure

Boreholes 16 and 18 are instrumented with relative humidity, temperature, and pressure transducers. Each borehole contains four pneumatically inflated packers, labeled in Figure 3-9 as P_1, P_2, P_3, and P_4, designed to sustain the high temperatures expected during the SHT heating phase. Instrumented intervals are numbered from the closest to the collar of the borehole 1, to the deepest zone, behind the last packer in the string, borehole 4. The eight instrumented intervals are referred to by borehole number followed by the zone number, i.e., 18- is the third instrument cluster from the collar in borehole 18. The pressure, temperature, and relative humidity sensors are all located just below (deeper in the borehole) the packer and are assigned the same numeric identifier as the packer just above them.

Each interval between packers, and one interval past the end of the last packer, is fitted with a one-quarter inch Teflon injection tube. Nominally dry and clean compressed air is regulated using mass flow controllers and injected into the designated zone. By selectively deflating different packers, various injection zones for each hydrology borehole are formed. Three possible test configurations are as follows: 1) deflate packer P_2, and use air injection line for P_1; 2) deflate packer P_3 and use air injection line for P_2; and 3) inflate all four packers and use the air injection line for P_4. These three configurations are denoted as injection zones zone 1, zone 2, and zone 3. All four packers in the

monitoring borehole are always inflated so that pressure response can be monitored in each of the four sensors.

3.2.3 Results

The temperature and pressure are continuously monitored while a test is conducted. During injection testing, data was collected at five second intervals early in the test period and as the test approached steady state, the data logging interval was increased. Calculated permeabilities are shown in Table 3-4 for each test conducted. Permeabilities taken before and after heating are compared in Table 3-5.

Table 3-4. Injection Test Conducted in the SHT Block

Date	Test Description (In the order they were conducted)	Q (SLPM)	dP (kPa)	Length (m)	Permeability (m^2)
25-Nov-26	Inj Behind 16-4	0.39	15190	2	2.58E-15
25-Nov-96	Inj Behind 18-4	9.96	12770	2	7.93E-14
25-Nov-96	Inj Between 16-2, 16-4	0.39	26000	0.762	2.83E-15
25-Nov-96	Inj Between 16-1, 16-3	9.95	21300	0.762	9.03E-14
25-Nov-96	Inj Between 18-1, 18-3	0.99	18000	0.762	1.08E-14
7-Aug-96	In Behind 18-4	2	1100	2	1.97E-13
7-Aug-96	Inj Behind 18-4	10	6300	2	1.167E-13
7-Aug-96	Inj Behind 16-4	2	18000	2	1.10E-13
7-Aug-96	Inj Behind 18-4	9.98	6100	2	1.73E-13
7-Aug-96	Inj Behind 16-1 (Open hole behind)	9.98	17400	4.1	3.28E-14
7-Aug-96	Inj Between 16-1, 16-4	9.98	21300	1.46	5.75E-14
7-Aug-96	Inj Between 16-1, 16-3	10	21800	0.762	8.85E-14
7-Aug-96	Inj Between 18-1 (Open hole behind)	10	5800	4.1	1.05E-13
8-Aug-96	Inj Between 18-1, 18-4	1	16900	1.46	7.43E-15
8-Aug-96	Inj Between 18-1, 18-3	0.99	17400	0.762	1.12E-14
8-Aug-96	Inj Between 16-2, 16-4	0.5	16800	0.762	5.27E-15
8-Aug-96	Inj Behind 18-4	10	5800	1.46	2.30E-13
8-Aug-96	Inj Behind 18-4	10	5700	1.46	2.34E-13

Table 3-5. Comparison of Air Permeability Before and After Heating of the SHT Block

Location	Permeability (m^2) Pre Heating	Permeability (m^2) 25-Nov	Ratio
Inj Behind 16-4	1.10E-14	2.58E-15	0.23
Inj Behind 18-4	1.73E-13	7.93E-14	0.46
Inj Between 16-2, 16-4	5.27E-15	2.83E-15	0.54
Inj Between 16-4, 16-3	8.85E-14	9.03E-14	1.02
Inj Between 18-4, 18-3	1.12E-14	1.08E-14	0.96

In Table 3-5 data in the first two rows correspond to the test configuration where the air injection is in zone 3 (Figure 3-9), data in the third row correspond to air injection in zone 2, and data in the fourth and fifth rows correspond to air injection in zone 1. It is noted that the most reduction in air permeability after three months of heating occurs in zone 3 of boreholes 16 and 18, while the permeability remains practically unchanged for injection in zone 1. These results can be understood from the TH simulations of the SHT (Birkholzer and Tsang, 1996). The most prominent TH response of the rock mass to the heater power output is the initial drying of the rock mass surrounding the heater, the carrying away of moisture in the form of vapor from the heated area, and the subsequent condensation of the vapor in the cooler regions of the rock mass farther away from the single heater. The vaporization, drying, and condensation processes are reflected in the spatial variation and temporal evolution of the liquid saturation of the rock mass, which in turn affect the spatial and time dependence of the air permeability values. Simulations show that the majority of drying from the heater occurs within one meter of the heater, and both boreholes 16 and 18 are too short to sample this region of vigorous boiling and drying (Birkholzer and Tsang, 1996). However, the increase of liquid saturation from condensation does occur in the region of the two hydrology boreholes, and the effect is more prominent the closer it is to the heater. Birkholzer and Tsang (1996) predictions indicate that the greatest reduction in air permeability during heating will come from air injection in zone 3 behind Packer P_4; while the saturation build up, and therefore the reduction in permeability in zone 1 is minimal. Simulations of air injection test results for injection in zones 1 through 3 in boreholes 16 and 18 are presented by Birkholzer and Tsang (1996). They are consistent with the measured data presented in Table 3-5.

The large reduction of the air permeability, by a factor of five after three months of heating for zone 3 in borehole 16, is indicative that the liquid saturation in the fractures has increased significantly due to condensation (Table 3-5). Enough water has been mobilized so that significant quantities may be transported into the boreholes.

On November 25, 1996, while preparing to conduct cross borehole air permeability measurements, as reported above, fluid was noticed in the air injection tube leading to zone 3 in borehole 16. This zone is situated between 3.05 m from the collar of the borehole to the bottom of the borehole at 5.10 m and has a volume of approximately 9.2 liter. Nalgene sample bottles provided by the TCO were used to collect all the fluid that would drain by gravity, approximately 5.5 liters. The fluid sample was brought to the Sample Management Facility for storage under Specimen ID 00520850 for later analysis.

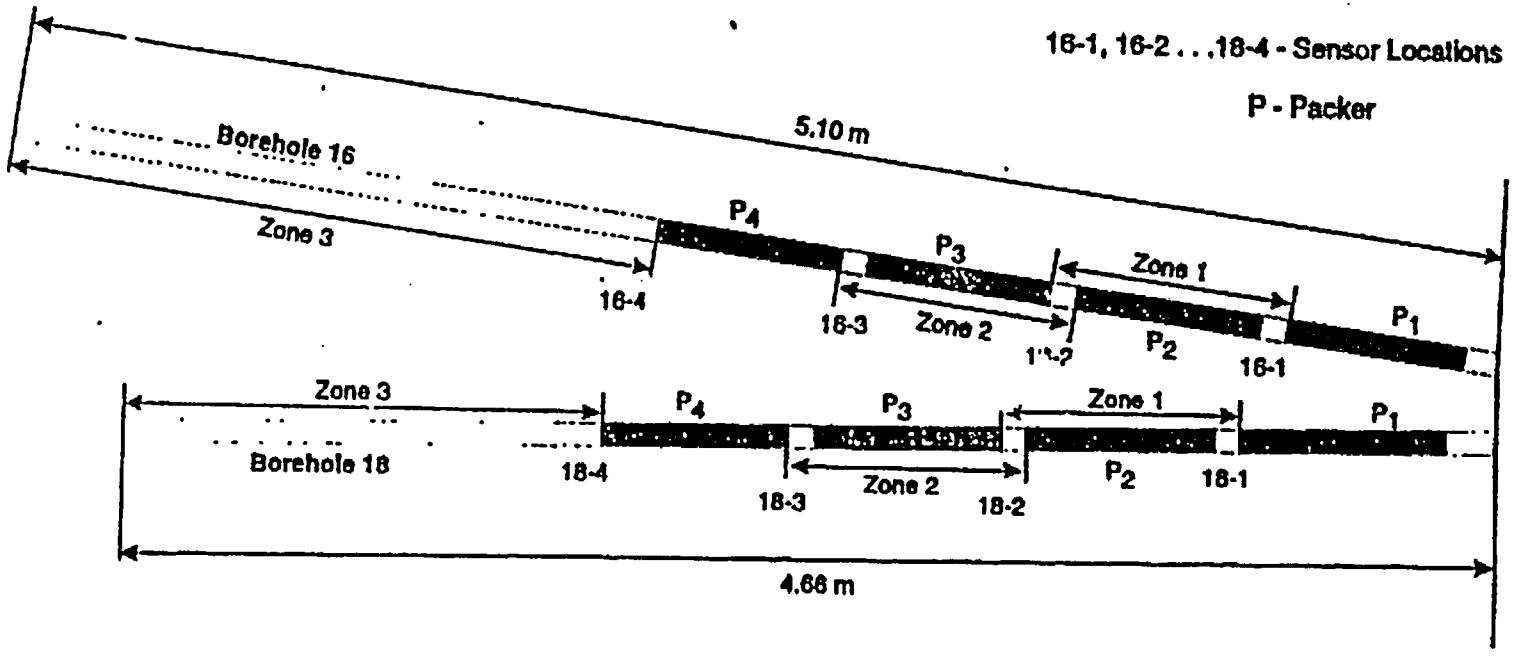

Figure 3-9. Geometry of the Air Injection Test Boreholes and Instrumentation

3.2.4 Summary

Cross borehole air injection tests are being conducted in the SHT block. Passive monitoring and active testing of the hydrology boreholes will continue during the heating and subsequent cooling phases of the SHT. Significant reductions in gas permeability are apparent in the zones closes to the heater, and liquid water has been found in borehole 16, zone 3. The modeling and predictive efforts that have been applied to the SHT will continue to be used to interpret field data, to gain better insight into the TH processes controlling the near field environment under thermal loading conditions.

3.3 SUMMATION OF *NEUTRON LOGGING MEASUREMENTS ... THE SINGLE HEATER TEST* (Lin and Roberts, 1997)

3.3.1 Introduction

A TDIF was not developed for this submission of the measured data since this procedure has not yet been properly calibrated.

Thermal neutron logging is a method used to determine moisture content in rocks and soils and was used to monitor moisture content in boreholes 15, 17, 22, and 23 during the SHT. The neutron probe contains a source of high energy neutrons and a detector for slow (thermal) neutrons. Water present in rocks slows down the neutrons because of the presence of hydrogen which makes the neutrons detectable. Thus, higher counts (a positive difference in counts relative to background or pretest levels) indicate relatively higher water content. The probe used in this test is a Campbell Pacific Nuclear CPN model 503DR. The 1.5 inch diameter probe was utilized for the SHT (SN H37067677). Under most ambient conditions the sampling volume has a diameter approximately 15 cm surrounding the probe, increasing as moisture content decreases. Measurements are sensitive to the presence of elements that have large neutron capture cross-sections, such as chlorine and boron.

For the SHT, a Teflon tube was inserted into the boreholes and grouted into place. The Teflon tube permits easy insertion, placement, and removal of the tool. The grout can potentially affect the moisture content readings, but by assuming that changes in the grout moisture content are similar to changes in the moisture content of the rock, one can interpret changes in counts relative to a background or pretest set of measurements as indicating changes in moisture content of the surrounding rock. Quantitative determinations rely on an appropriate set of calibration measurements.

3.3.2 Procedures

The following procedure describes the method of collecting neutron data during the SHT. The 1.5 inch diameter probe and a counting time of 16 seconds. Standard counts were measured and recorded immediately prior to, and subsequent to performing measurements. The neutron probe was placed in a borehole at a specific location and the neutron count recorded in a scientific notebook as well as electronically in the device memory. Upon completion of the test, data were downloaded

to a computer and the data values checked against the hand recorded values. Data were recorded at depth intervals of 10 cm in each borehole.

Neutron logs were recorded on the following dates: August 21, 1996, September 19, 1996, October 24, 1996, and November 26, 1996. The first date is a pre-test measurement, performed before heater activation.

3.3.3 Results

A fairly high level of variation of counts exists within an individual borehole. These variations are most likely a result of fractures, lithophysal cavities, or the centralizers used to center the Teflon tube. Other observations include modest decreases in counts relative to pretest levels between 5.6 to 6.6 m (borehole 15), 4.4 to 7.0 m (borehole 17), and 4.4 to 5.2 m (borehole 23). The decreases are most evident in the October 24, 1996 and November 26, 1996 data sets. The most pronounced decrease in counts is that observed for borehole 17, which is the borehole that passes closest to the heater (at an approximate depth of 6.2 m) This depth also closely corresponds to the peak temperature along borehole 17. Increased counts indicative of increased water content are noted in borehole 17 (1.6 to 3.6 m), borehole 22 (1.8 to 4.0 m), and borehole 23 (1.8 to 3.5 m).

3.3.4 Performance of Measuring System

The measurement system has performed as expected. Changes in the neutron counts over time can be related to the movement and redistribution of water in response to changing thermal conditions in the SHT. Further analysis should provide a quantitative measure of moisture content. Anomalous readings were recorded on August 21, 1996 during the logging of borehole 17. Similar anomalous readings were documented in a scientific notebook on September 5 and 6, 1996. The entire unit was then inspected and a potential intermittent short found and corrected. No anomalous readings have been noted since this repair and the system is operating normally.

3.4 SUMMATION OF *ELECTRICAL RESISTIVITY MONITORING OF THE THERMOMECHANICAL HEATER TEST IN YUCCA MOUNTAIN* (Ramirez et al, 1997)

3.4.1 Introduction

A TDTF has been submitted and the DTN is LL9701004244.026.

Of the several thermal, mechanical, hydrological, and chemical measurements being used to monitor the rockmass response, in the SHT electrical resistance tomography (ERT) is being used to monitor the movement of liquid water with a special interest in the movement of condensate out of the system. Four boreholes, containing a total of 30 ERT electrodes, were drilled to form the sides of a 30 foot square with the heater at the center and perpendicular to the plane. Images of resistivity change were calculated using data collected before and during the heating episode. The changes recovered show a region of decreasing resistivity approximately centered around the heater. The size this region grows with time and the resistivity decreases become stronger. The changes in resistivity are caused by both temperature and saturation changes. The observed resistivity changes suggest

that the rock adjacent to the heater dries as heating progresses. This dry region is surrounded by a region of increased saturation where steam recondenses and imbibes into the rock.

ERT surveys are conducted during the SHT to map the changes in moisture content caused by temperature changes. The formation and movement of condensate within the fractured rock mass is of particular interest. Electrodes were positioned along four inclined boreholes drilled around the region of interest. A subset of the electrodes shown in Figure 3-10 was used to conduct ERT surveys around the heater.

ERT is a geophysical imaging technique which can be used to map subsurface resistivity. Rock mass heating creates temperature and liquid saturation changes which result in electrical resistivity changes that are readily measured. The ERT measurements consist of a series of voltage and current measurements from buried electrodes using an automated data collection system. The data are then processed to produce electrical resistivity tomographs using state of the art data inversion algorithms. These tomographs show the spatial distribution of the subsurface resistivities.

Some of the important features of the two-dimensional algorithm for ERT measurements are described briefly. For additional details, the reader is referred to Morelli and LaBrecque (1996). The algorithm solves both the forward and inverse problems. The forward problem is solved using a finite element technique in two-dimensional. The inverse problem implements a regularized solution which minimizes an objective function. The objective of the inverse routine is to minimize the misfit between the forward modeling data and the field data, and a stabilizing functional of the parameters. The stabilizing functional is the solution's roughness. This means that the inverse procedure tries to find the smoothest resistivity model which fits the field data to a prescribed tolerance.

To calculate the changes in the rock's electrical resistivity, a data set obtained after heating started, was compared to a corresponding data set obtained prior to heating. The analysis could be performed by subtracting, pixel by pixel, two images corresponding to two different times. However, this approach could not be used because the resistivity structure was three-dimensional, i.e., several boreholes containing metallic instruments, were located near the plane of interest. These metallic instruments caused large conductive anomalies and made the resistivity structure three-dimensional.

3.4.2 Results

Figure 3-11 presents two-dimensional tomographs collected during the SHT. The location of the heater is indicated on the figure. The images show the areas of the rock in which the electrical resistivity changed as a result of changes in temperature and saturation. Each image shows the changes detected for a given time relative to preheating conditions (data collected on August 22, 1996). The image labeled "repeat test" (top left image) shows changes detected using two data sets collected two hours apart. No changes were expected at this time because heating had not yet begun. Any changes observed in this image would be indicative of the effects of measurement error on the inversion process. On average, these "noise" images showed the resistivity ratio to deviate from 1.0 (i.e., perfect result when no changes occur) by +/-0.05. This analysis showed that changes of about five percent could be expected on the basis of measurement error. Therefore, the changes observed during heating need to be substantially bigger than five percent in order to be considered reliable.

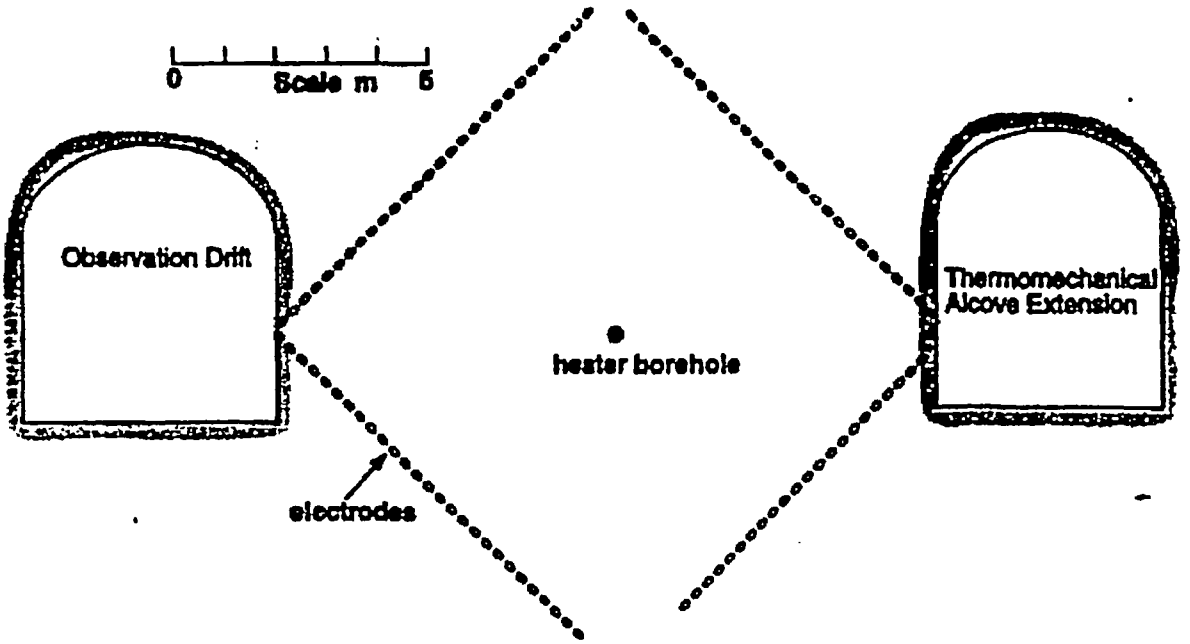

Figure 3-10. Location of the Heater Borehole Relative to the Electrode Boreholes and Underground Openings

The remaining images in Figure 3-11 show the resistivity changes after heating started. On August 29, 1996 (top right image), three days after heating started, the changes observed are of the same order as those expected to be caused by measurement error. The September 3, 1996 image (center left image), shows resistivity decreases relative tot he pre-heating data as implied by ratio of less than unity, which are considered reliable. The changes are roughly centered around the heater, as expected for a radially symmetric temperature field. The decreases grow stronger (i.e., ratio gets smaller) in September 19, 1996 image as heating continued for another 16 days; also, the anomaly is approximately radially symmetric. The lower left image in Figure 3-11 shows the strongest resistivity decrease after almost two months of continuous heating. In this image, the resistivity decreases are no longer radially symmetric. The images in Figure 3-11 and the 3-12 plots can be used together to interpret the resistivity changes in terms of saturation, if the temperatures are known.

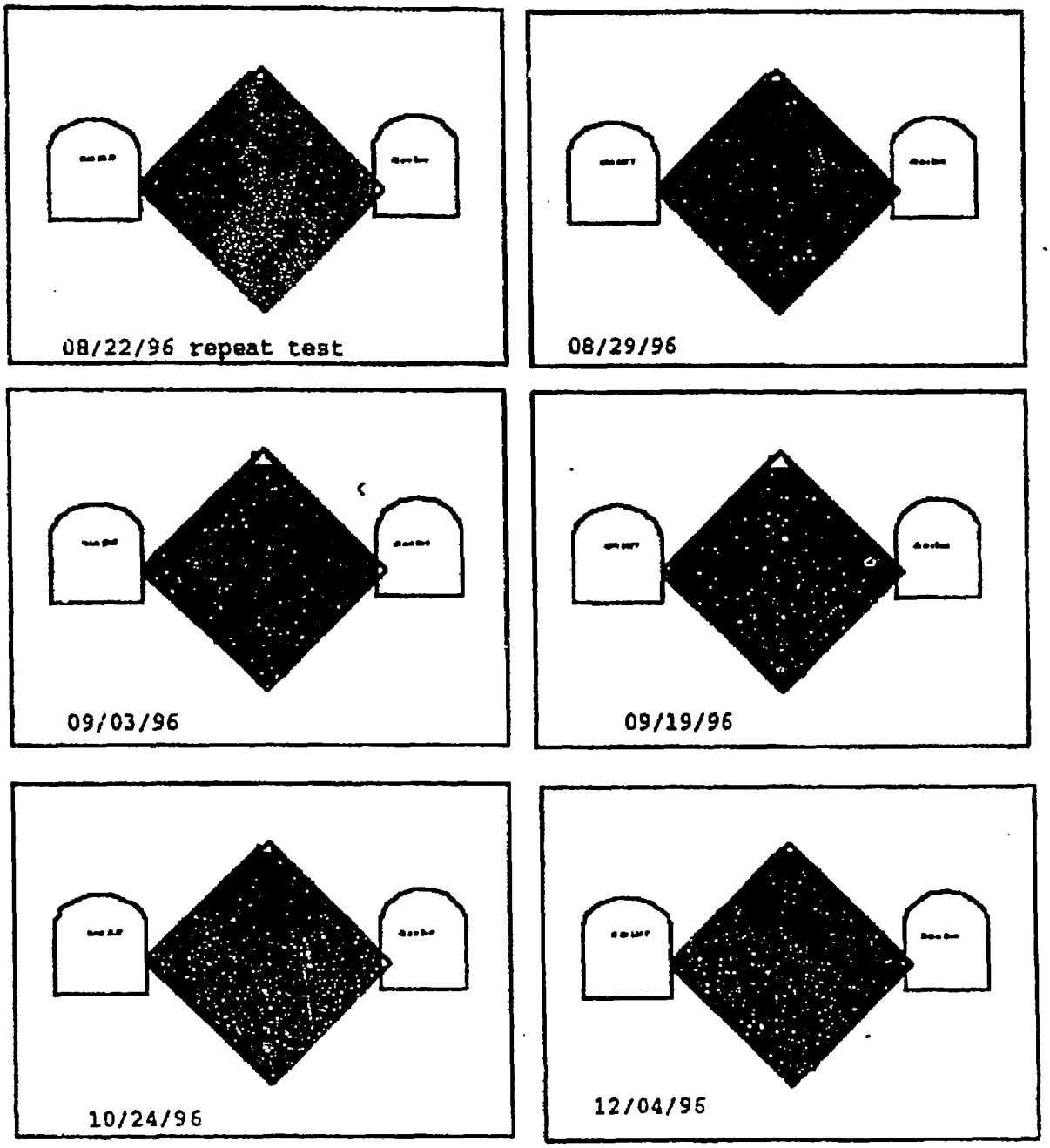

Figure 3-11. Chronology of Two-Dimensional ERT Tomographs

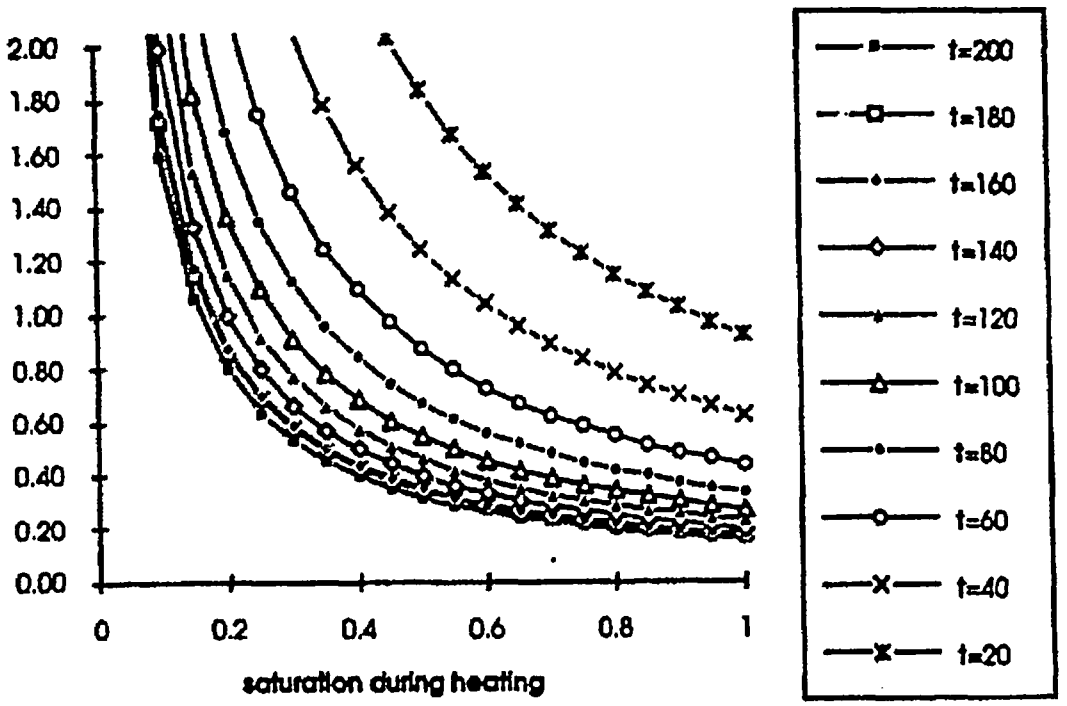

These plots assume that $Sw_i = 0.92$ and $T_i = 25°C$.

Figure 3-12. Liquid Saturation During Heating Versus Resistivity Ratios

The data collected on and after October 25, 1996 indicate that the region of maximum change (lowest ratio) in Figure 3-13 is no longer centered around the heater. This region is now located below the heater. Only temperature and saturation are assumed to change to resistivity. Other studies have shown that heat transfer in this rock is conduction dominated. Since the thermal properties of the rock are reasonably homogeneous, the temperature field is expected to be circular in shape and centered on the heater. If temperature increases were solely responsible for the changes in resistivity in Figure 3-13, then the resistivity changes would result in similar geometry. The images for September 3 and 19, 1996 show anomalies that are roughly circular and approximately centered on the heater. The change in anomaly geometry between September 19, 1996 and October 25, 1996 suggests that changes in saturation may be responsible. As water boils near the heater and recondenses in cooler regions, increases in saturation occur. Drainage of some of this condensate is expected along the predominantly vertical fractures present. The condensate can then be imbibed by the partially saturated rock surrounding the fracture. The differences in behavior of the condensate above and below the heater are probably the cause of the asymmetry in Figure 3-13. Previous experimental and numerical modeling work shown in Wilder (1996) is consistent with this interpretation.

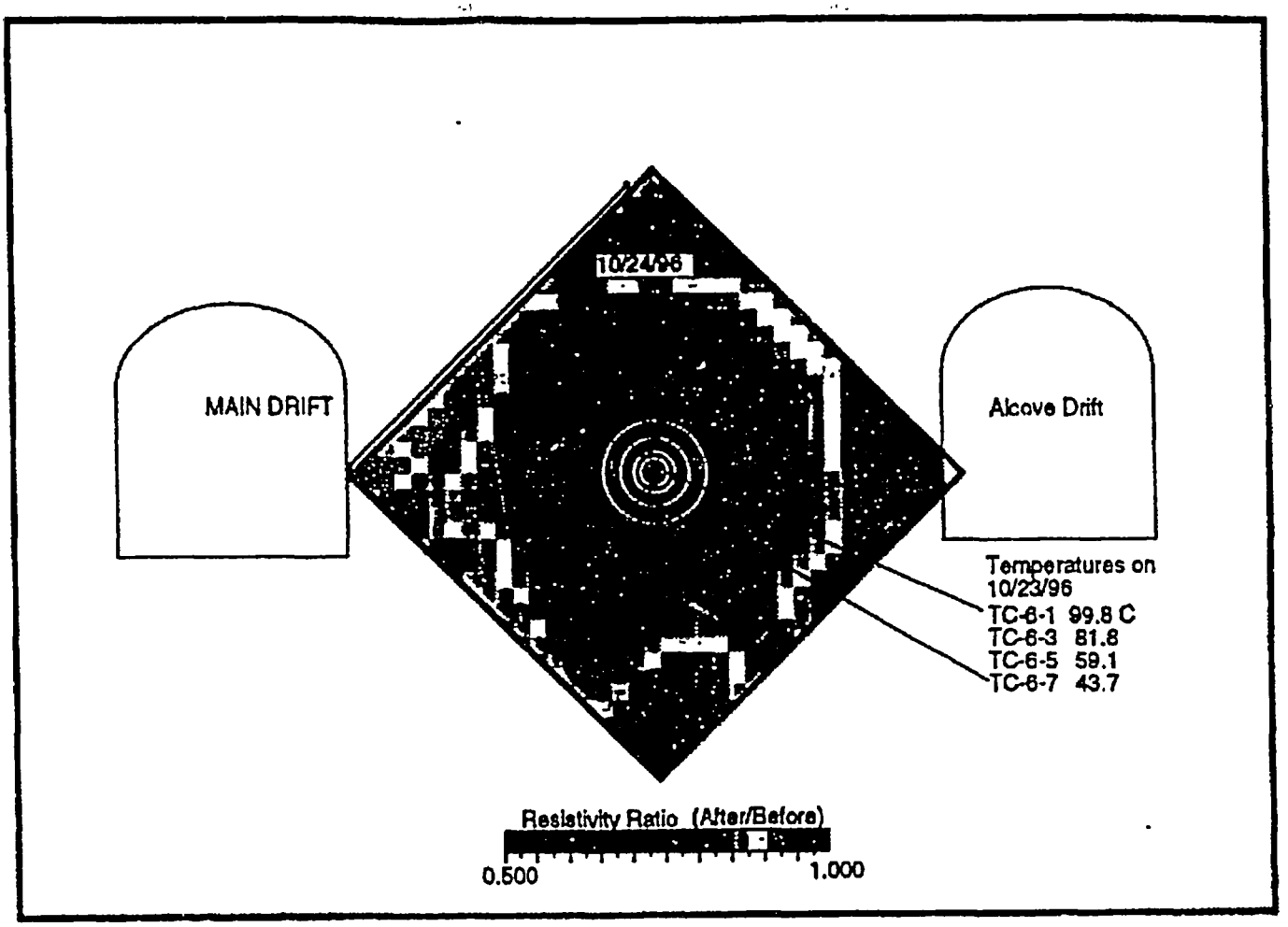

Figure 3-13. Two-Dimensional ERT Tomograph Corresponding to 10/24/96

We consider the saturation estimate for rock adjacent to the heater an *upper bound* for the following reasons: 1) The inverse algorithm finds the smoothest model that fits the data. This implies that when there are sharp gradients in resistivity ratio values (as expected near the heater), the inverse problem will tend to find a more gradual gradient of values. In addition, the region of minimum resolution is located near the center of the image; this also would tend to "smear" any gradients that exist. We believe that these two effects result in resistivity ratios closer to 1.0 (smaller change) around the heater than the true values. 2) Also, when a region of very dry rock develops around a heater, its likely surrounded by a region that is much wetter and very hot. The wet hot region is much more electrically conductive than the very hot and dry rock adjacent to the heater and completely surrounds it. This type of resistivity structure may not be detectable because the electrical energy tends to flow in the conductive annulus formed by the hot, wet rock and bypass the highly resistive core of hot dry rock adjacent to the heater.

3.4.3 Summary

To calculate the changes in the rock's electrical resistivity, a data set obtained after heat activation is compared to a corresponding data set obtained prior to heating. The changes recovered show a region of decreasing resistivity approximately centered around the heater. The size of this region grows with time and the resistivity decreases become stronger. The changes in resistivity are caused by both temperature and saturation changes. The early tomographs show an anomaly centered on the heater and roughly radially symmetric. The largest resistivity changes occur closest to the heater. Later tomographs show that the anomaly is no longer centered on the heater; the largest resistivity changes appear somewhat below the heater. This change in position is interpreted to mean that the condensate is preferentially draining downward. The observed resistivity changes suggest that the rock adjacent to the heater dries as heating progresses. This dry region is surrounded by a region of increased saturation where steam recondenses and imbibes into the rock.

3.5 SUMMATION OF *INFRARED IMAGING IN THE SINGLE HEATER TEST AREA* (Cook and Wand, 1997)

3.5.1 Introduction

The TDIF has been submitted and the DTN in LB970100123142.

For the duration of the SHT the rock surfaces on the SHT block are periodically examined using an infrared camera to determine what effect the heater has on the block surface temperatures. The monitoring is performed to assess whether the thermal distribution from the heater can be observed on the block surface, to determine if this can be related to any known or unknown physical features in the SHT block. Such features could include surface outlets for pathways of fluids or gases that undergo thermally induced changes. A tripod-mounted portable IR camera was used to obtain sets of infrared images in the SHT block on April 12, 1996, August 28, 1996 (Day 2), and December 17, 1996 (Day 113).

The thermal images cover roughly one square meter at the distance from which they were taken at the opposite wall and each contain 256 x 256 pixels stored in digital format. The IR intensity from each pixel is converter into nominal temperature readings which can be compared over time for given locations to obtain temperature differences. Focus in manual. The nominal temperature resolution per pixel is 0.1°C but the immediate temperature readings are strictly for visual comparison purposes. Individual frames, however, can be manipulated to correct for emissivity and background radiation so as to match independently known temperatures of objects in the images. As currently used, these adjustments are not altered from default and held fixed for all images so that meaningful comparisons of temperature over time can be made. Spot measurements of temperature can be taken for given features. For better visual cues of the temperature distribution, the images, which in the native form are grayscale, can be arbitrarily color-keyed to match a desired colored temperature legend. For overall heat distribution, the exposed block surface can be best visualized and observed for known features when the individual images are montaged. Montages in grayscale and color-code have been assembled for the area above the SHT collar.

Currently, the SHT block is covered with an insulating blanket from the invert to near the crown of the drift, leaving only areas not directly in line with the heater uncovered for observation. Those uncovered areas of the drift closes to the heater are the invert, the ..iling around the block, and the east wall of the thermomechanical extension drift. The invert is largely covered with muck and so is not regarded as a viable study area. The transition from block to crown is curved with a one to two meter radius providing a surface of bare rock above the insulation from which to obtain thermal images. The end of the thermomechanical extension drift has a metallic frame fitted to provide spatial reference points in the IR images. The insulation does not transmit any heat from the block but does reflect spurious heat signatures from the surroundings.

3.5.2 Results

The current focus is on the set of image files which were created from the ceiling transition area above the SHT heater collar on August 28, 1996 (Day 2) and December 12, 1996 (Day 113) shown in Figure 3-14. This latter set is the only one to show significant effects on the block surface temperature from heating. The August pictures show only small differences from the April set, mainly due to drying of construction water, and thus provide good baseline data even though they were acquired shortly after the heater was turned on. All changes in the December set itself occurred in pictures taken in the area directly above the SHT.

A comparison between the Day 2 and Day 113 montages clearly demonstrates the effect of the heater on the temperature of the exposed rock. The temperature in the Day 2 pictures is almost uniformly 25°C to 7[illegible]°C. The only large anomalies in temperature at this time are from reflections of the surroundings such as lamps, off the shiny insulation cover. In the Day 113 data there is a clearly defined halo of heat centered directly above the SHT. The halo is not uniform but has some extensions distributed to the left and slightly to the right of the heater. These extensions do not seem to correspond to any readily visible features in the rock surface, they could be artifacts of channeled heat rising between the insulation and the rock face.

One type of feature that does show on both the visual and IR images is that of rockbolts. Rockbolts have a good thermal connection to the rock mass and are also readily observable in the thermal images. In the August frames it apparent that the bolts' hollow interiors, which are essentially black bodies with good thermal connection to the rock mass, are slightly color (0.3°C to 0.4°C) than the collars. In the December frames however the difference is *reversed* and greater in magnitude (0.7°C).

3.6 INVESTIGATIONS OF WATER ACCUMULATION IN BOREHOLE 16-4

On November 25, 1996, while preparing to conduct cross-borehole air permeability measurements in the SHT block, fluid was observed in an injection tube running into zone 16-4 of borehole 16 (see Figure 3-9). Zone 16-4 is about 2 m in length. Borehole 16 also has a slight incline of about 7.5 degrees, so that the bottom of the borehole is about 0.7 m higher in elevation than its collar. Approximately 5.5 liters if fluid, that would drain by gravity, was collected on November 25, 1996.

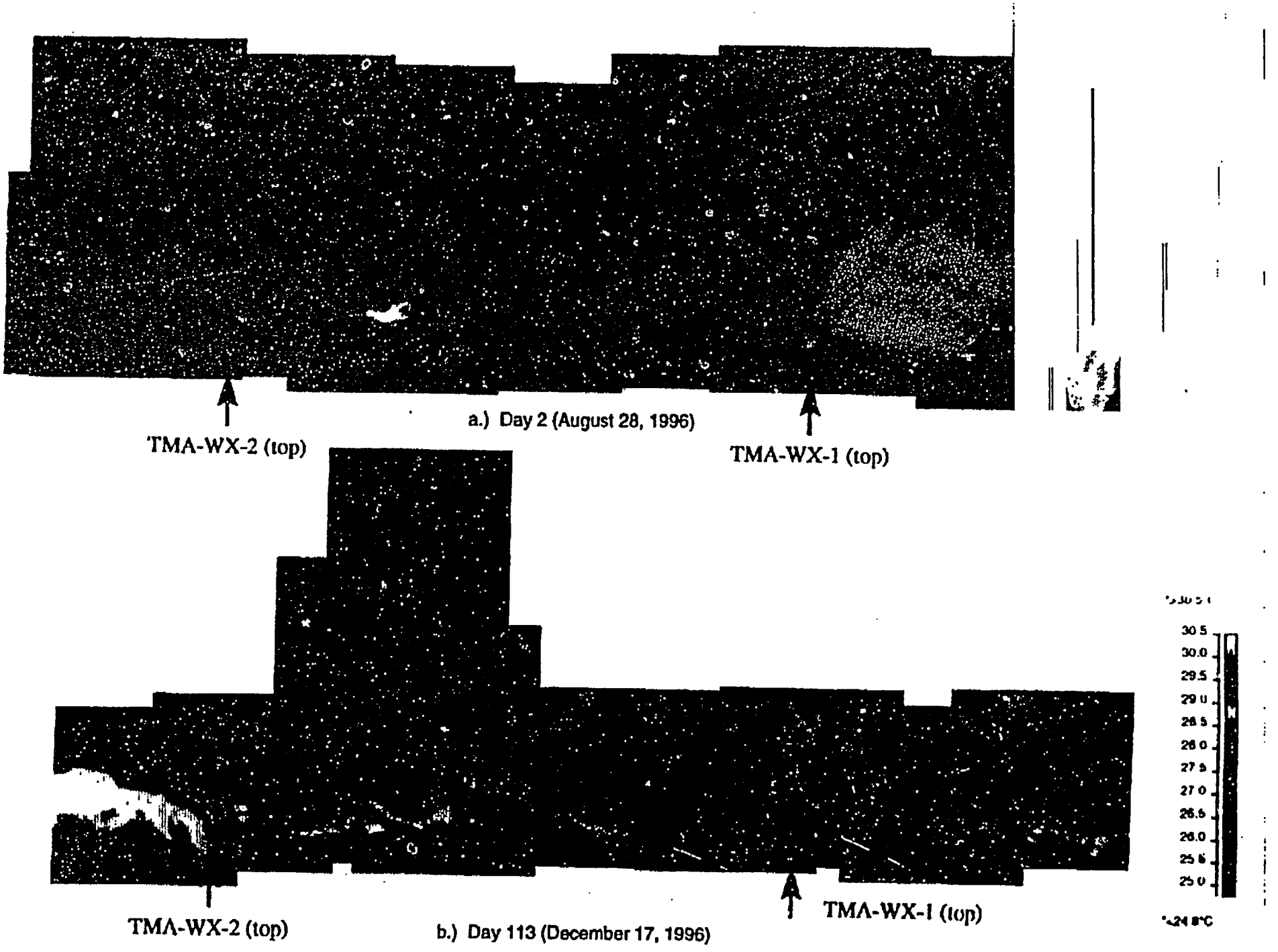

Figure 3-14. Infrared Images Above the SHT Heater Collar at Day 2 and Day 113

3.6.1 Hydrological

The first discovery of water in zone 16-4 occurred after three months of heating in the SHT. At three months, the 100°C isotherm is approximately 0.8 m from the heater borehole. Assuming that the pore water was vaporized in a cylindrical volume of 0.8 m radius and 5 m length (heater length) were vaporized, the estimated amount of moisture which could be condensed in the cooler region translates to about 10 cubic meters of rock mass. Therefore, about 1000 liters of pore water would exist for a matrix porosity of 0.11 and ambient liquid saturation of 0.92. Thermohydrological simulations (BNL 1996) show that 16-4 lies in the condensation zone, and liquid saturation is near unity. As liquid saturation builds up in the rock mass surrounding zone 16-4, it is conceivable that totally saturated regions exist adjacent to the borehole walls. Under these conditions, capillary pressure becomes nonexistent thus allowing water to drip freely into the borehole. The packer 16-4 serves as a stopper to the water accumulating behind it in zone 16-4. Borehole 16 has a diameter of 7.57 cm, therefore the capacity of 16-4 is about 9.4 liters. Since water was collected by drainage through the air injection tube, which was located near the center of the borehole, it is possible that zone 16-4 was entirely filled with water.

On February 4, 1997 another 5.5 liters of water was removed from zone 16-4 prior to scheduled cross-borehole air-injection test in boreholes 16 and 18. Since 5.5 liters of water was collected both times, it is likely zone 16-4 was filled to capacity. Furthermore, the liquid saturation in the rock mass immediately surrounding zone 16-4 had the opportunity to reach unity in the time interval between November 25, 1996 and February 4, 1997. Also, zone 16-4 was drained two hours later and another 75 ml of water was collected. An attempt was made to drain more water from 16-4 the next morning (February 5, 1997) but none could be collected.

An explanation for water accumulation in zone 16-4 is summarized below. Vapor from the boiling of water near the heater flows outward and condesenses around zone 16-4. The liquid saturation in the rock mass reaches unity, in at least some area adjacent to the borehole, so water can drip freely into zone 16-4. The exact period of time required to fill up 16-4 is not known but certainly is less than 69 days. Once zone 16-4 is filled to capacity, liquid saturation in the rock mass near 16-4 can increase not only from the condensation of vapor, but also from the imbibition of water from the more saturated rock mass surrounding the borehole.

Upon draining zone 16-4 space became available for more water inflow. Immediately after 16-4 is drained, water from a thin layer of fully saturated rock mass can freely drip into the borehole, accounting for the additional 75 ml of water collected within two hours of the previous drainage. However, once the thin layer of rockmass in the immediate vicinity of the borehole is drained, it forms a capillary barrier which will prevent any further dripping until liquid saturation of the rock mass adjacent to the borehole reaches unity from imbibition. However, imbibition is a very slow process, which may explain the absence of water available for collection on February 5, 1997.

3.6.2 Chemical

3.6.2.1 Introduction

Water was collected from the SHT borehole 16 on November 25, 1996 (see above). Chemical and isotopic analyses of that water were conducted over several weeks. The reported results are presented in the accompanying Table 3-6.

Mechanisms for water entry into boreholes is expected to be predominately via fracture flow although some component of flow may result from water migration through the rock matrix. A wide range of minerals have been observed in fractures sampled from surface-based boreholes and the Exploratory Studies Facility (Lin and Daily, 1984; Carlos, 1987, 1989, 1994; Daily et al., 1987; Lin, 1991; Lin et al., 1995; Glassley and Boyd, 1995). Previous simulations of borehole 16 water were hampered by a lack of field-based pH measurements. The results presented here take advantage of more recent data in which field-based pH measurements were obtained. Consideration is given to water-rock interaction for fracture linings containing calcite and a silica polymorph (opal-CT or quartz). Other minerals, such as clays, zeolites, and oxides will be considered at a future time. This assemblage is considered first because it is common in samples from the Large Block Test (Glassley and Boyd, 1995), and in samples of high porosity, cemented, breccia zones in drill core recovered from the SHT and DST alcoves.

3.6.2.2 Results

The analysis of the first water sample from borehole 16 was made difficult by the absence of a pH measurement at the time the sample was collected. However, more recent samples (collected on February 4, 1997) suggest a pH of 6.2 (R. Datta, personal communication/electronic mail, February 5, 1997). Using this value, the in situ HCO_3- can be computed on the basis of charge balance. The resulting HCO_3- is shown in Table 3-6. Based on these values, the sampled water is saturated with respect to hematite quartz, and nontronite (a clay; $[(Na,K)_{0.33-2x}(Ca,Mg)_xFe^{+++}{}_2Al_{0.33}Si_{3.67}O_{10}(OH)2]$), at temperatures between 40 and 90 C, according to EQ3/6 simulations (Wolery, 1992).

The borehole 16 water clearly cannot be pure condensate since such water would essentially be distilled water with very low concentrations of dissolved species. As mentioned previously, however, (June Fabryka-Martin, personal communication/electronic mail, December 6, 1996), the Cl concentration is less than any previously observed water within Yucca Mountain, and the low Br/Cl ratio is much lower than that in construction water. These results indicate that the water is probably predominately condensate that has interacted to some degree with fracture lining minerals.

Table 3-6. Comparison of Results From Chemical Analyses of Borehole 16 Water and Other Water Source

Constituent (mg/l)	SHT Hole 16 LLNL Data	Log Molality LLNL Data	SHT Hole 16 LANL Data	EQ3/6 1st Attempt[a]	EQ3/6 2nd Attempt[a]	J-13[b]	G4[b]	Rainier Mesa Fracture Water
Na	16	-3.16E+00		0.0116	n. e.	45.8	57	35
Si	16.8	-3.22E+00		27.24	18.8	28.5	21	25
Ca	13	-3.49E+00		0.44	12.3	13	13	8.4
K	2.5	-4.19E+00		5.31E-04	n. e.	5	2.1	4.7
Mg	1.63	-4.17E+00		2.40E-04	n. e	20.1	0.2	1.5
pH	6.2			7.6	6.44	7.4	7.7	7.5
HCO_3[c]	84.4	-2.86E+00		42.3		129	139	98
F	0.44	-4.64E+00				2.16	2.5	0.25
Cl	2.54	-4.14E+00	2.1			7.1	5.9	8.5
S	0.71	-4.65E+00						
SO_4	1.83	-4.72E+00	1.5			18.4	19	15
PO_4	<0.03					<10		
Nitrite	<0.01							
NO_3	1.1	-4.75E+00				8.8		
Li	<0.03					0.048	0.067	
B	0.37	-4.47E+00				0.134		
Al	<0.06					0.02		
Fe	0.74	-4.88E+00						
Sr	0.2	-5.64E+00				0.04		
Br	<0.02		0.008					
del ^{18}O	-98.2					-98	-103	
del O	-13					-13	-13.8	

[a] EQ 3/6 simulation discussed in text
[b] From Harrar et al., 1990
[c] Computed from charge balance
n.e. = not evaluated

The stable isotope data are virtually identical to that of water from J-13. The values measured fall within the range of other measured values at Yucca Mountain, and are consistent with meteoric water. Meteoric waters unaffected by high-temperature water-rock interaction tend to correlate closely with the well-established meteoric water line, (Craig 1961). The isotopic characteristics of condensate depend on the actual temperature history followed by the evolving fluid and its initial isotopic composition. During the initial period of evaporation/boiling, the residual water would become relatively enriched in D and ^{18}O (i.e. displaced to the right of the meteoric water line), and the condensate would become relatively depleted in D and ^{18}O (i.e. displaced to the left of the meteoric water line). As evaporation continues, the condensate signature would become progressively enriched as the residual water evaporated. After the water had evaporated, the condensate isotope characteristics would be indistinguishable from that of the original meteoric water.

The water from borehole 16 appears to come from nearly complete boiling and condensation of pore water in the vicinity of the heater with a resulting minimal shift in initial isotopic signatures. This interpretation is also consistent with stable isotope data collected by LBNL on a separate aliquot of the November 25, 1996 sample. However, there are minor discrepancies between the LLNL and LBNL data which will be resolved in the analyses of the February 4, 1997 samples. The water composition is generally more dilute than water from either the saturated zone (note J-13 and G-4 analyses, Table 3-6) or from fracture water (Rainier Mesa, Table 3-6). However, the pH is significantly lower than other observed waters. This behavior could be interpreted that the water has not achieved chemical equilibrium with the rock since the other waters are close to chemical equilibrium with the host rock mineralogy.

3.6.2.3 Modeling

The extent of water-rock interaction can be bounded by modeling reaction of condensate water with coexisting matrix or fracture minerals. Initial simulations focused on calcite-silica interactions, as they are the dominant minerals in most fractures; future simulations will add alumino-silicates (e.g., feldspars, zeolites, and clays) and halide sources (e.g., halite) to account for the alkali metals and chloride, respectively. Because the flow path followed by the solution is unknown, it was assumed that condensate formed on fracture walls lined with calcite (90 mole percent) and amorphous silica (5 mole percent). Surfaces areas were assumed to be approximately proportional to molar abundances.

In conducting sensitivity analyses of the time-dependent solution compositions as a function of mineral abundances, dissolution rate constants were varied within the range of values reported for the individual phases. However, the values were also constrained by the limited amount of time available for the minerals to react with the water (the heater was turned on August 26, 1996 and the water collected on November 25, 1996; 91 elapsed days), thus defining effective minimum dissolution rate constants. Although effective surface areas were assumed to be approximately proportional to molar abundance, the effect on concentration of variation in the surface area was also considered.

The solutions collected were at approximately 45°C. Since condensate would initially form at approximately 95°C, it was also assumed that most mineral-water interaction took place at

approximately 90°C. It was also assumed that upon cooling to approximately 45°C there was no precipitation of mineral phases. This assumption needs further evaluation.

3.6.2.4 Comparative Analyses

Table 3-6 shows the summary results of previous attempts to model the fracture-flow water from borehole 16 (Glassley, 1997). These results (EQ3/6-First Attempt) were conducted without solution pH information. In these simulations it was assumed that the solution was in equilibrium with atmospheric gases, thus constraining the pH. The match between measured and calculated compositions was poor.

In the current simulations, it was found that the measured pH values cannot be achieved unless there is an elevated CO_2 partial pressure relative to atmospheric values. The results presented in Table 3-6 are for a simulation in which the CO_2 partial pressure was 3.98E-2 bars; atmospheric CO_2 partial pressure is approximately 3.16 E-4 bars. With this two order of magnitude difference, the pH, Ca, and Si concentrations are closely approximated after approximately 70 days of interaction with the calcite-amorphous silica fracture mineralogy. [Note: Preliminary Sr isotope data from LBNL also suggest that the water has undergone significant interaction with fracture calcite.] Although further modification of reaction rates and effective surface areas could give an exact match, the absence of actual measurements of effective surface areas does not justify such an approach. Further refinements in the simulations will be made by including Na-, K-, Mg-, and Cl-bearing phases to reproduce all the cation and anion concentrations.

The CO_2 source remains unknown. Elevated CO_2 partial pressures could result from micro-biological activity in a warm, humid environment; breakdown of naturally occurring carbonates; and/or CO_2 release from curing grout during heating.

3.6.2.5 Conclusions

Close match between calculated and measured water composition for pH, Ca, and Si can be achieved for borehole 16 water samples if elevated CO_2 partial pressures are present, and interaction of condensate with fracture-lining carbonate and silica occurred. Further simulations are in progress to establish the source for Na, K, Mg, and Cl in the solutions.

The source for the elevated CO_2 remains unknown. It is important that this be established to determine the extent the relevant processes have been incorporated in previous conceptual models of the near-field environment.

3.7 STATUS OF CHEMICAL MEASUREMENT

Except for the chemical analyses of water samples collected from Borehole 16-4, chemical measurements have been limited. Chemical sensors included in the SEAMIST (CRWMS, 1996a) system became defective early in the test because of the harsh thermal environment and are not anticipated to produce any meaningful data. Water chemistry of samples taken from absorbent pads located in the SEAMIST will be conducted and reported at a later date.

4. INTEGRATED (COMPARATIVE) ANALYSES

This section compares the predicted data presented in Section 2 with the measured data presented in Section 3. These comparisons represent an integral component of satisfying the primary objective of the ESF Thermal Test. Specifically, the primary objective is to develop a more in-depth understanding of the coupled TMHC processes which are linked directly to the isolation of radionuclides. These comparisons are considered interim or preliminary in that most measured data are from the initial 100 days of heating and the comparisons examine only a cross-section of the TMHC behavior. A more comprehensive comparison of predicted and measured data is planned for the final report.

4.1 THERMAL

A history of temperatures measured by gages TMA-TC-4A-6 and TMA-TC-5A-7, and the temperature predicted by the high and low permeability cases (Sobolik, et al., 1996) at nearby grid points, are plotted in Figure 4-1. A history of temperatures, measured by gage TMA-TC-1A-7 is compared to both the low and high permeability cases (see Section 2.1) at a nearby grid location in Figure 4-2. In Figure 4-2 during the first few days of heating, the temperature rises conductively in both models but rises slightly more quickly in the high permeability case than in the low permeability case. This behavior reflects the existence of modest groundwater convection in the high permeability case. When the rock temperature reaches the boiling point, the models exhibited small to negligible temperature increases for nearly one month. During this time interval, the water in the pores of the rock is boiling such that liquid water and steam coexist. In the high permeability case, the steam can readily escape from the rock so the pore pressure remains near atmospheric. In the low permeability case, the steam is more inhibited from escaping from the rock so the pore pressure increases sufficiently which raises the boiling point of the water. Correspondingly, the temperature of the adjacent rock is also increased.

In Figures 4-1 and 4-2 the predicted temperatures rise faster than the measured temperatures until at least the boiling temperature. This thermal behavior is likely the result of a low thermal conductivity for wet rock. A higher thermal conductivity would allow heat to escape from the rock more quickly, thereby causing its temperature to rise more slowly. A constant thermal conductivity value of 1.671 W m^{-1} $°C^{-1}$ was used for both wet and dry rock. This value is derived from measurements on rock samples which had been stored in a warehouse for some period of time and hence had likely dried somewhat compared to their *in situ* saturation. The actual saturation of the measured samples is unknown but most likely was comparatively dry. In the sub-boiling portions of the block, there is substantial liquid saturation and the thermal conductivity is likely significantly higher than the selected input value.

Also, the measured temperatures rise relatively smoothly as a function of time even as the temperatures passed through the boiling point. The isothermal region evident in the high permeability case and the inflection points from the low permeability case do not exist in the measured temperature agreement is good in some locations data. This thermal behavior suggests that convection in the SHT block is minor and conduction is the primary mode of heat transfer even in temperature regions above the boiling point for water.

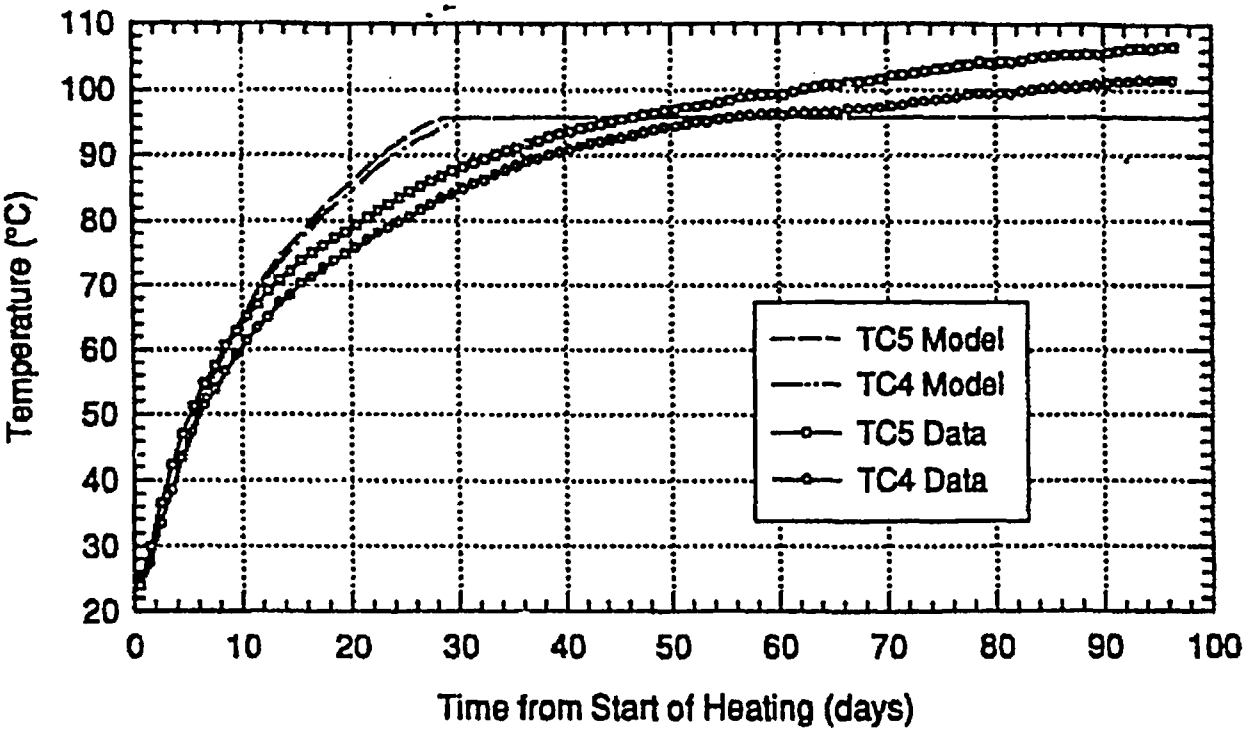

(a) High Permeability Model

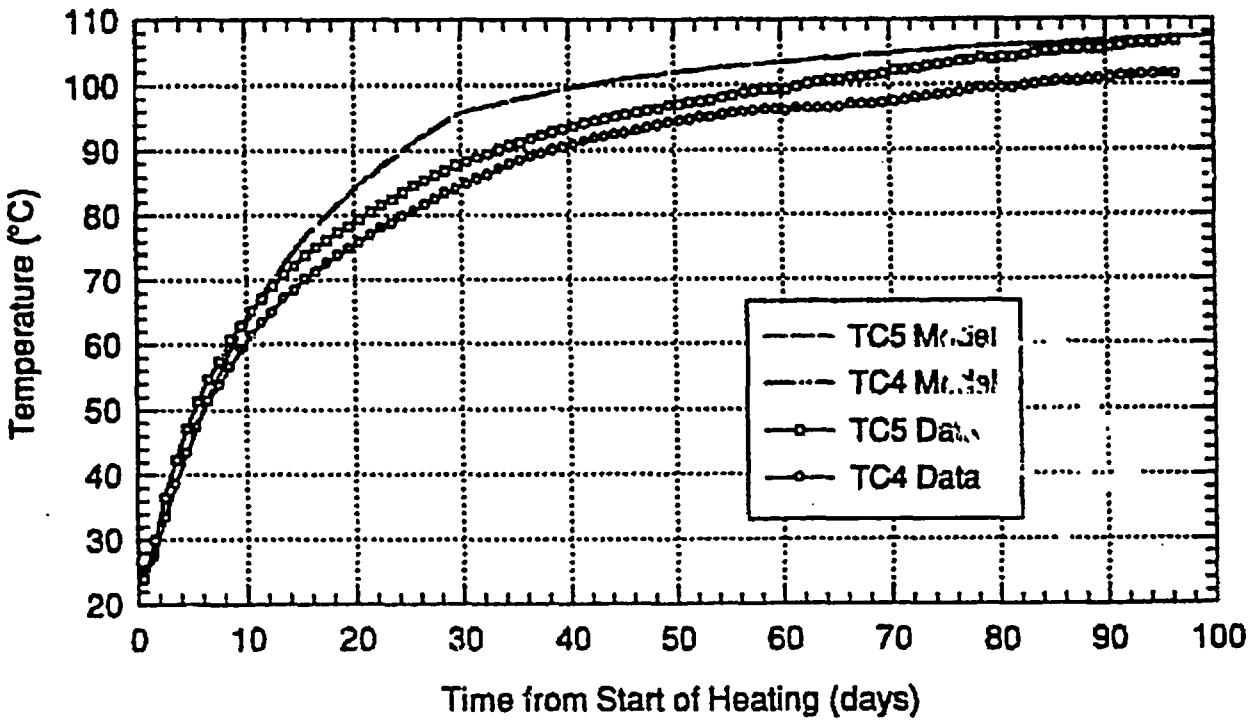

(b) Low Permeability Model

Figure 4-1. Predicted and Measured Temperature Histories Corresponding to TMA-TC-4A-6 and TMA-TC-54-7 at the Heater Mid-length

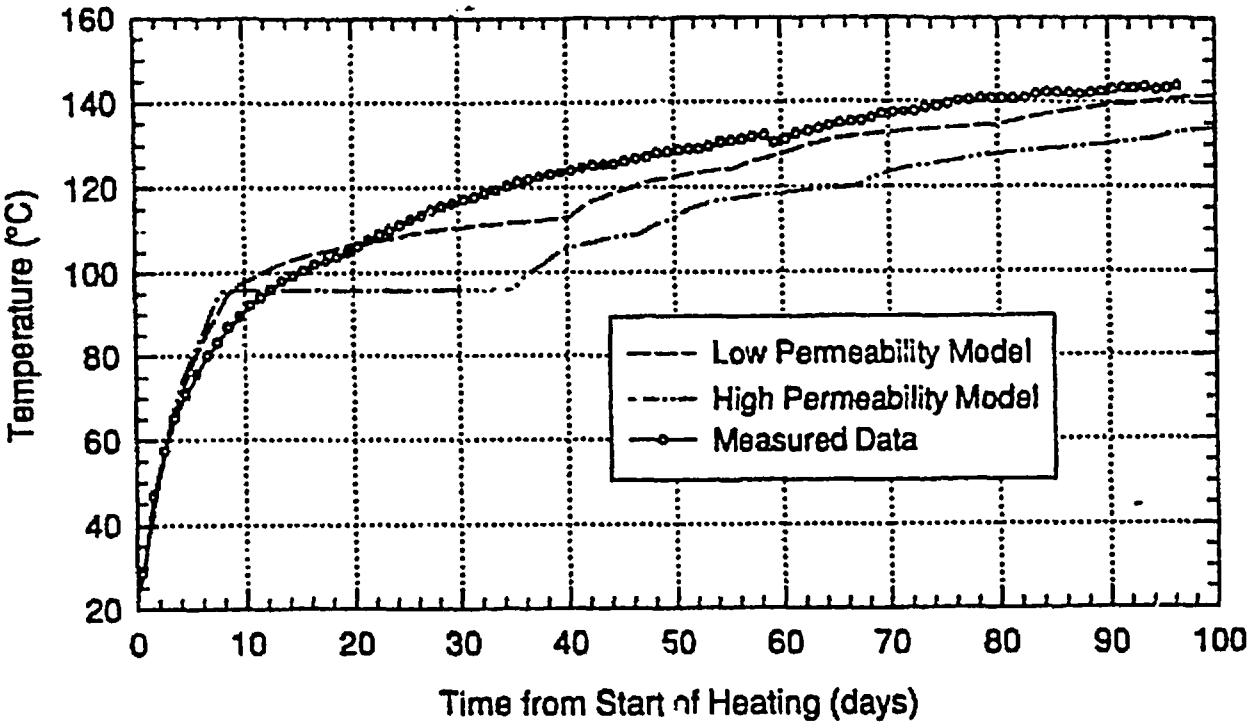

Figure 4-2. Predicted and Measured Temperatures Corresponding to TMA-TC-1A-7

The measured temperatures after 96 days of heating are compared to predicted temperatures in Figures 4-3 through 4-17. The predicted temperatures are interpolated for each sensor location. In each figure, the measured data are compared to both the high permeability and the low permeability pretest prediction models. The agreement between the measured and predicted data are mixed. While measured temperature agreement is good in some locations such as TMA-TC-1 and TMA-BX-4-TC, discrepancies are significant in other locations such as TMA-TC-3.

The thermal sensor TMA-TC-6 provides a typical example for an assessment of measured and predicted temperatures as presented in Figure 4-8. These sensors are emplaced in a horizontal borehole perpendicular to the heater, which approaches the heater from the positive X direction. These sensors illustrate the temperature distribution with respect to radial distance from the heater. At radial distances from the heater greater than about one meter, predicted temperatures are below the boiling point of water and agreement with measured temperatures is good. At radial distances less than a meter, the predicted temperatures exceed the boiling point of water and vapor phase heat transport in the high permeability model is significant. This thermal behavior accounts for the approximately 20-cm-thick, nearly-isothermal region near 96°C. In this region, steam and liquid water coexist at near atmospheric pressure and hence the temperature is nearly constant at 96°C.

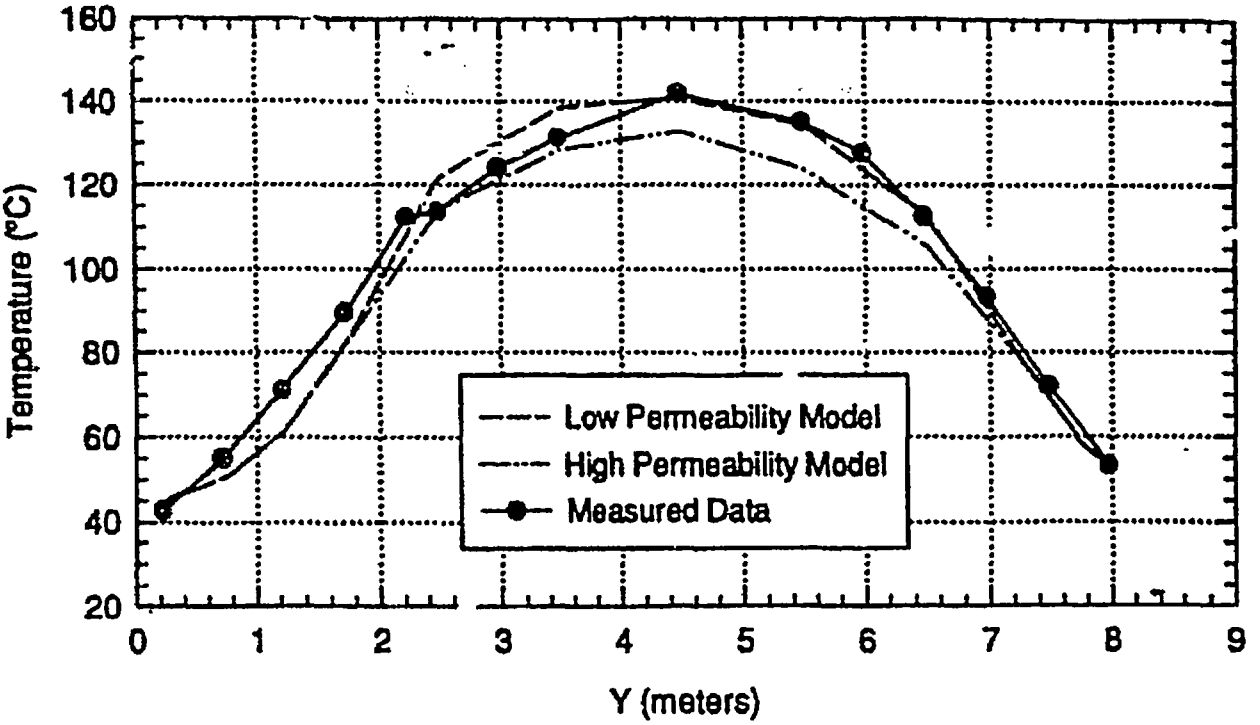

Figure 4-3. Predicted and Measured Temperatures Corresponding to TMA-TC-1

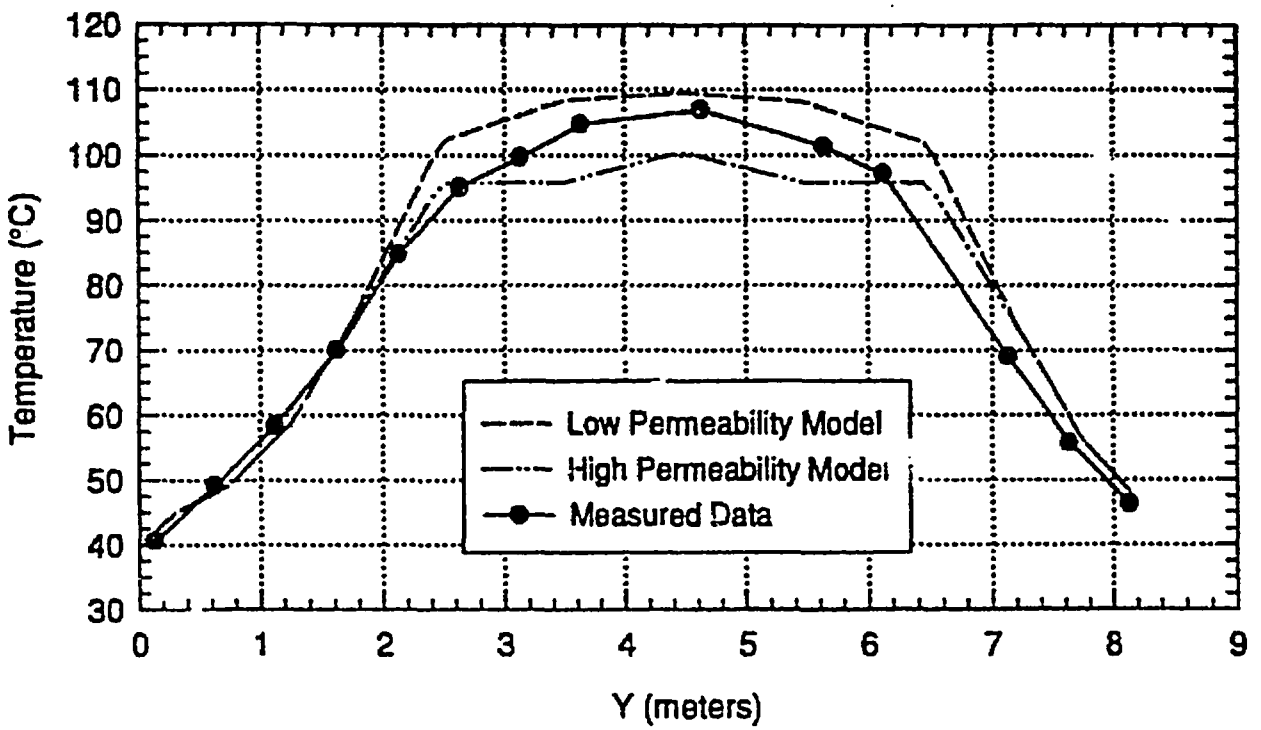

Figure 4-4. Predicted and Measured Temperatures Corresponding to TMA-TC-2

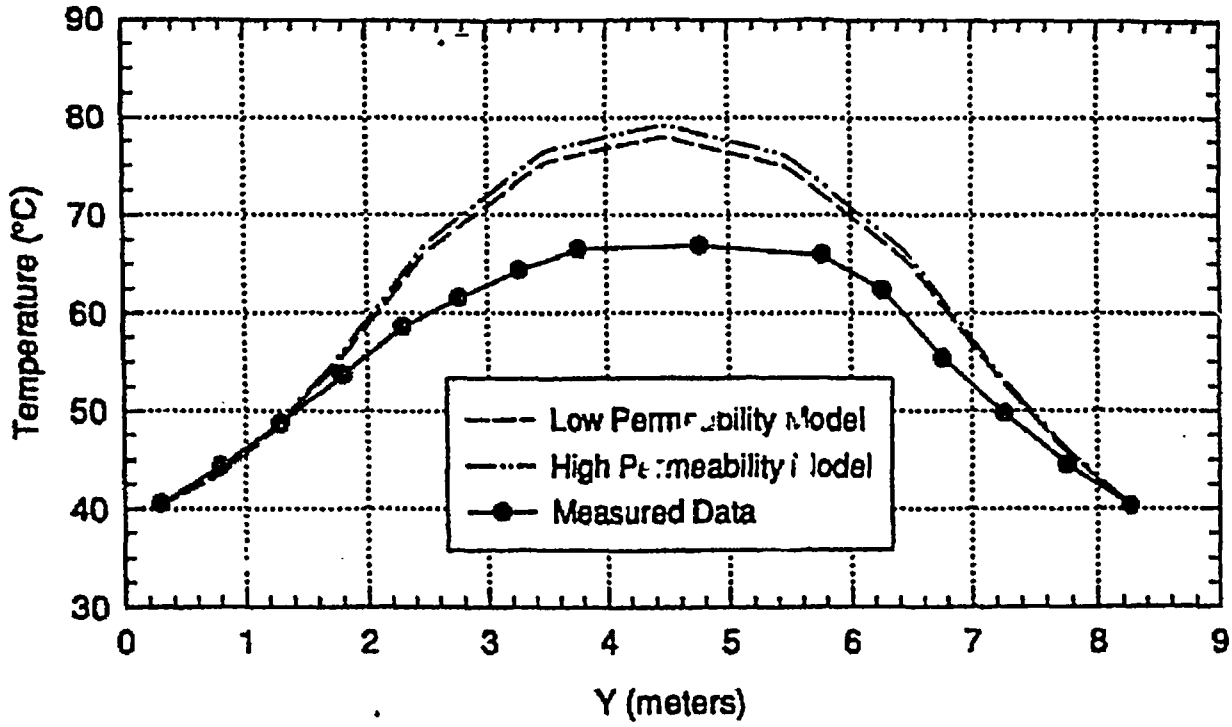

Figure 4-5. Predicted and Measured Temperatures Corresponding to TMA-TC-3

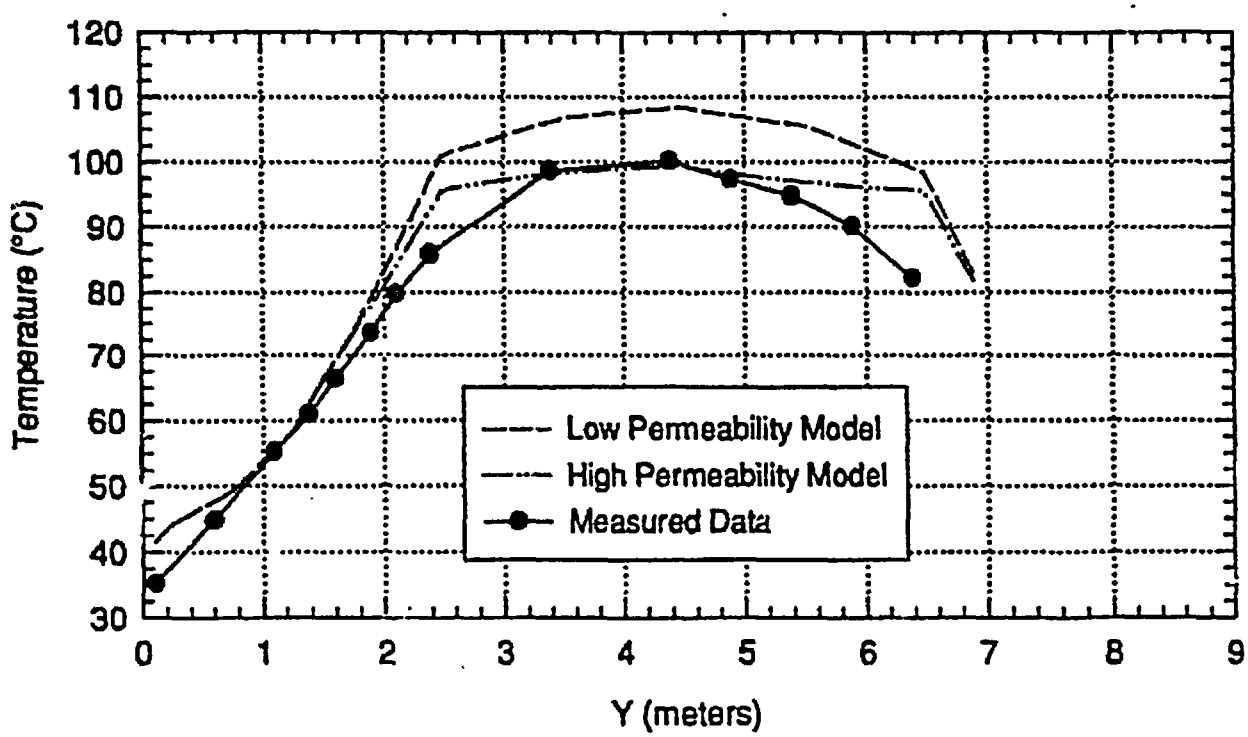

Figure 4-6. Predicted and Measured Temperatures Corresponding to TMA-TC-4

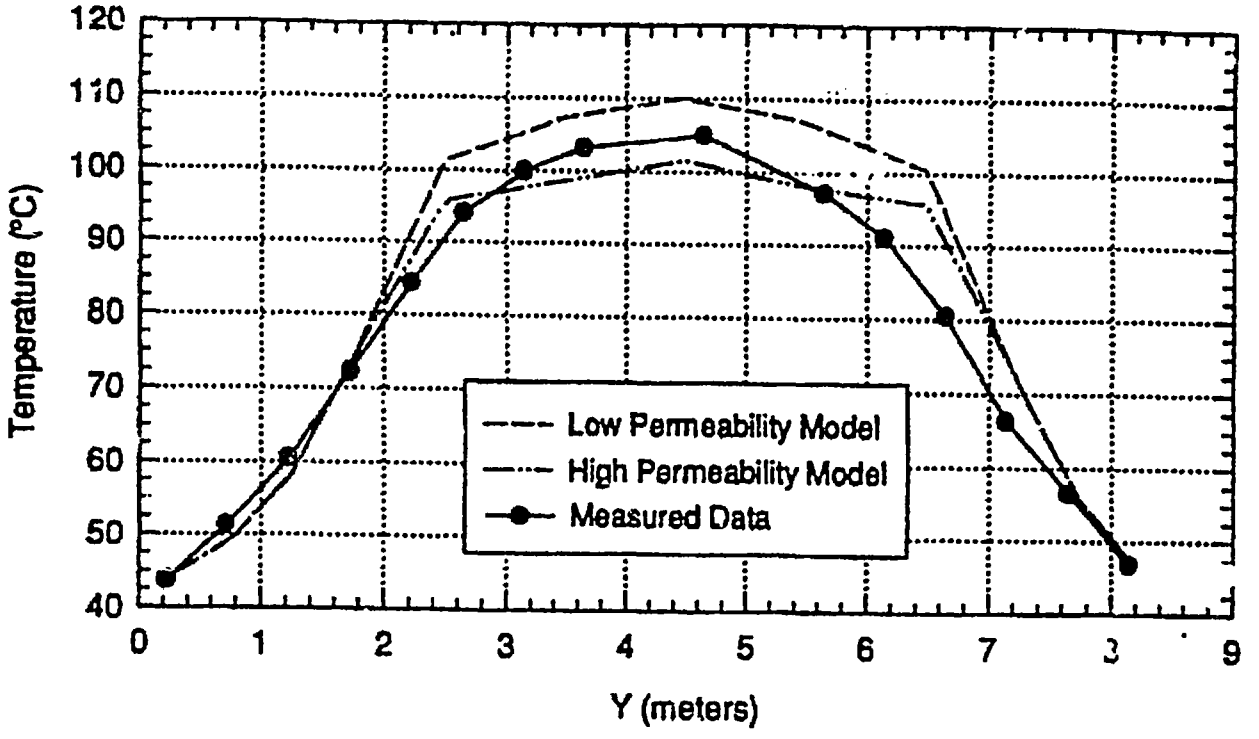

Figure 4-7. Predicted and Measured Temperatures Corresponding to TMA-TC-5

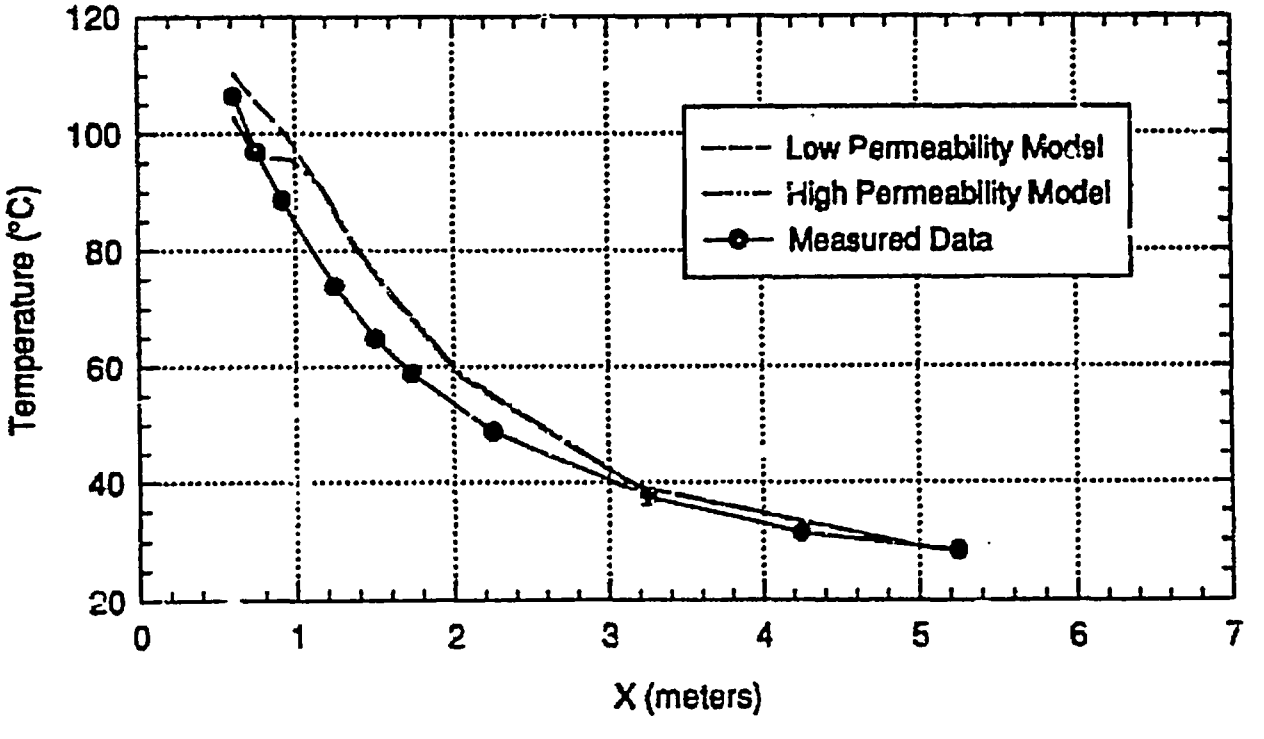

Figure 4-8. Predicted and Measured Temperatures Corresponding to TMA-TC-6

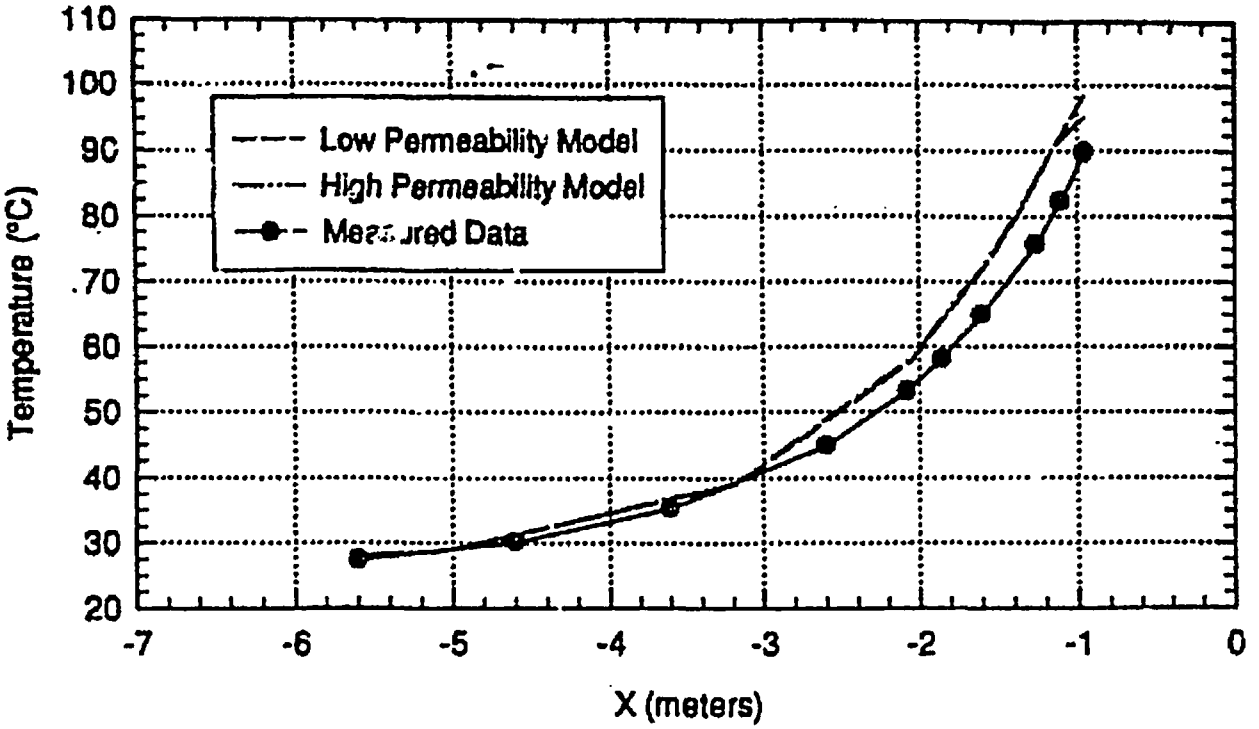

Figure 4-9. Predicted and Measured Temperatures Corresponding to TMA-TC-7

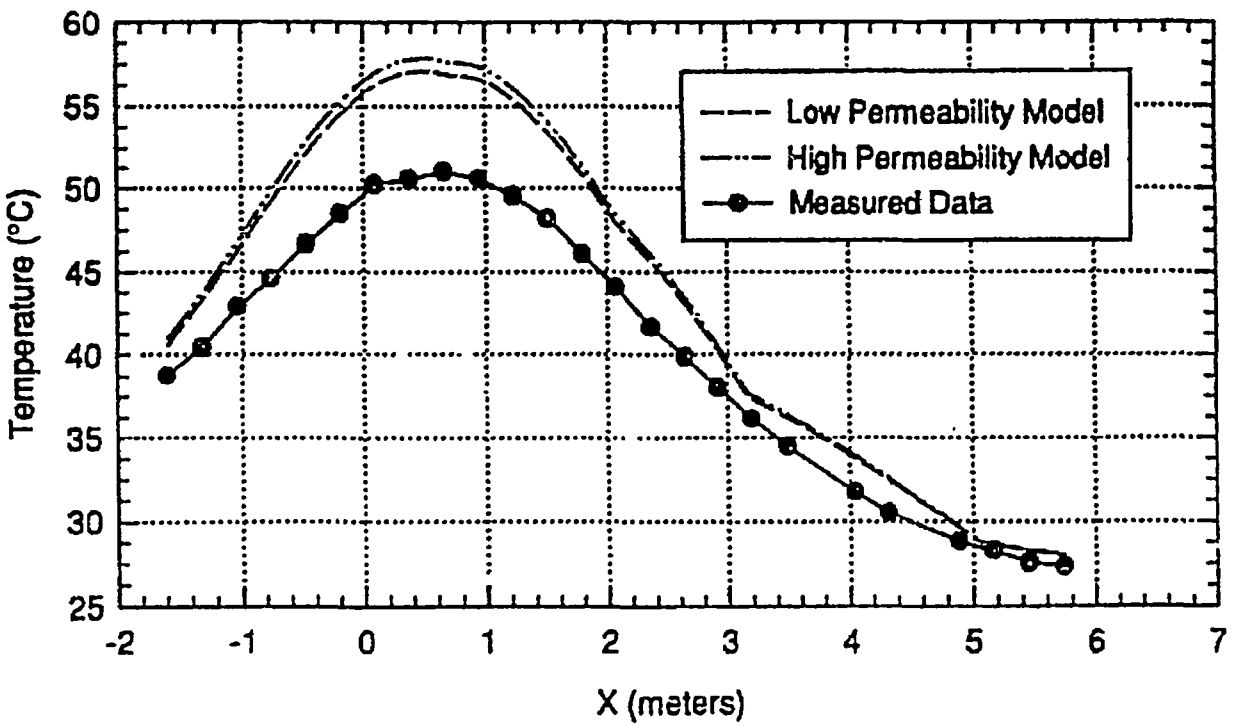

Figure 4-10. Predicted and Measured Temperatures Corresponding to TMA-RTD-15

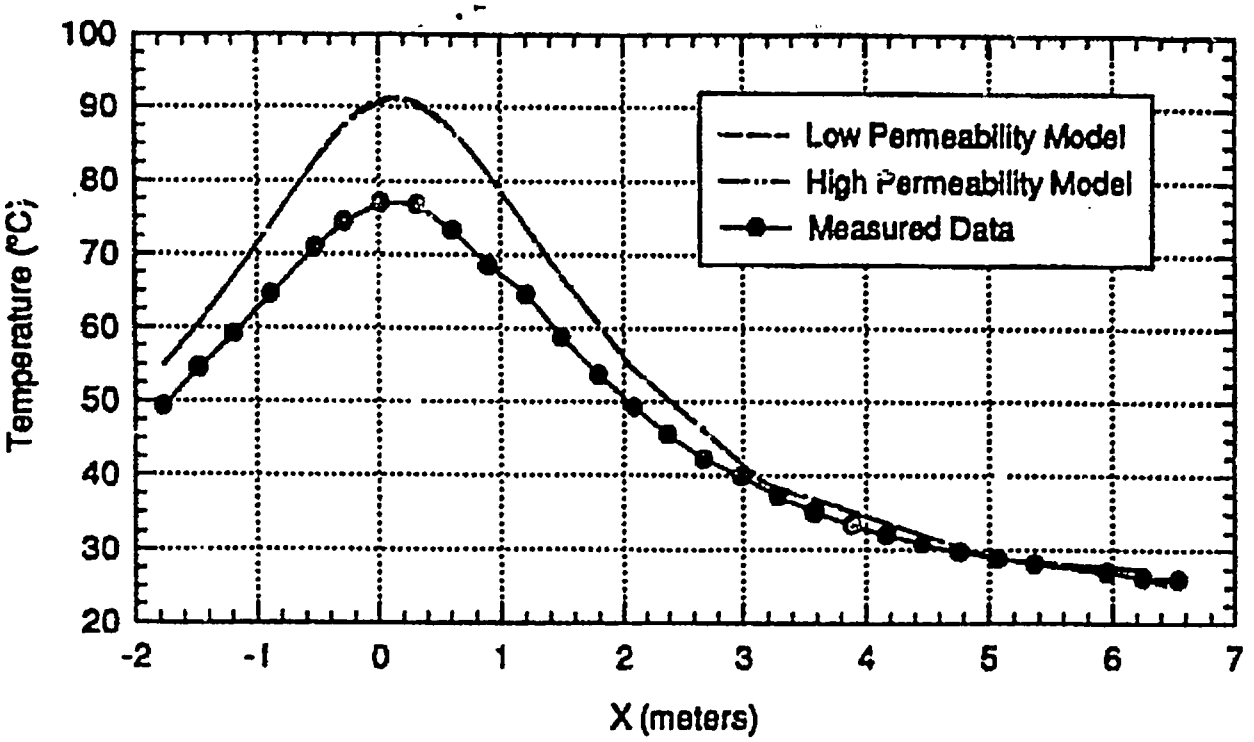

Figure 4-11. Predicted and Measured Temperatures Corresponding to TMA-RTD-17

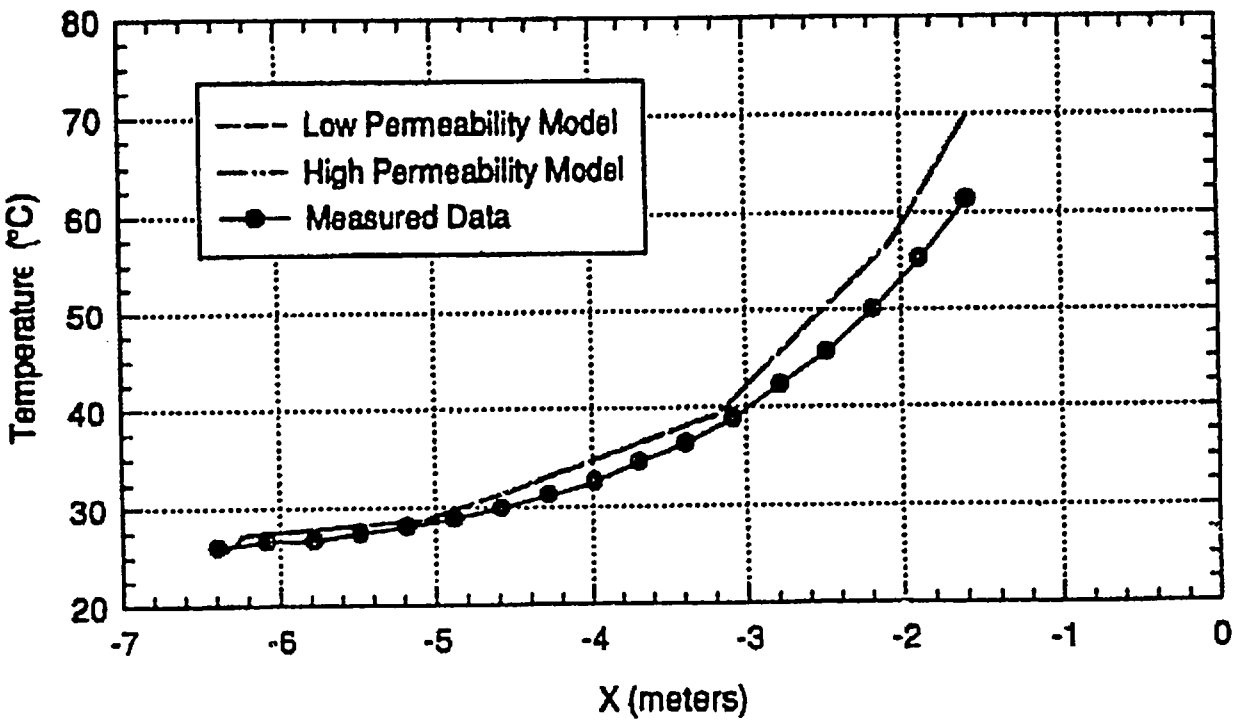

Figure 4-12. Predicted and Measured Temperatures Corresponding to TMA-RTD-22

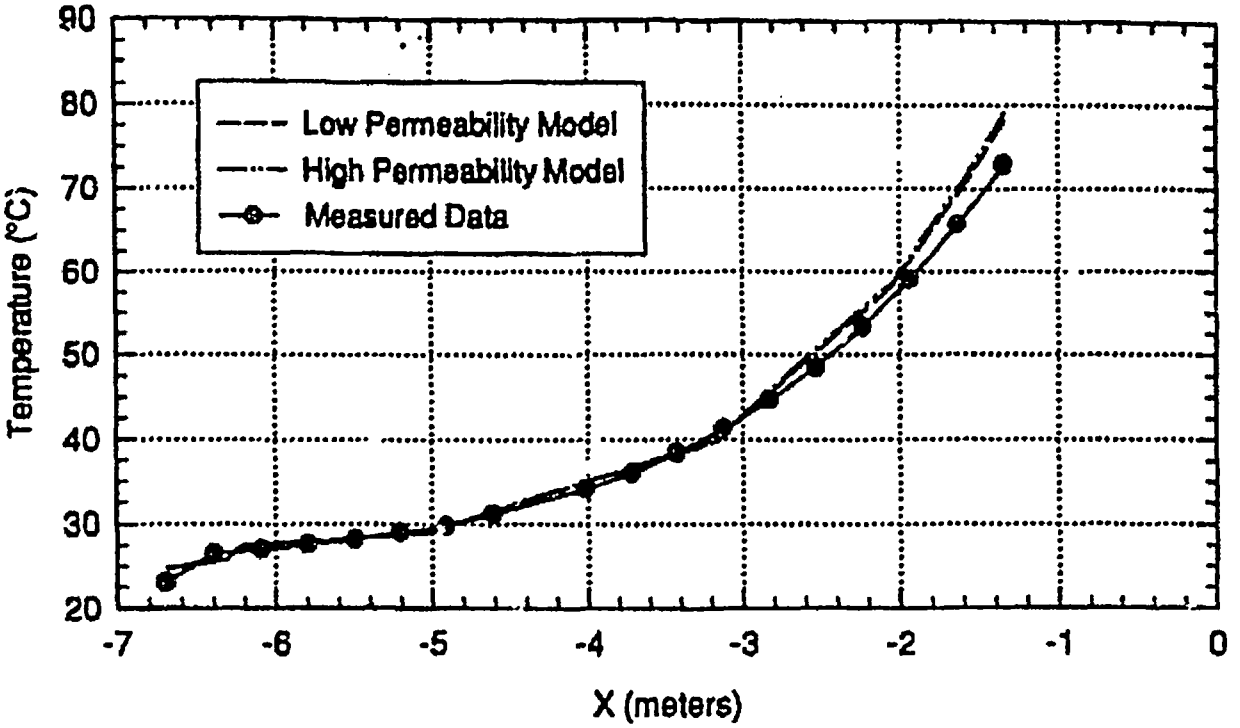

Figure 4-13. Predicted and Measured Temperatures Corresponding to TMA-RTD-23

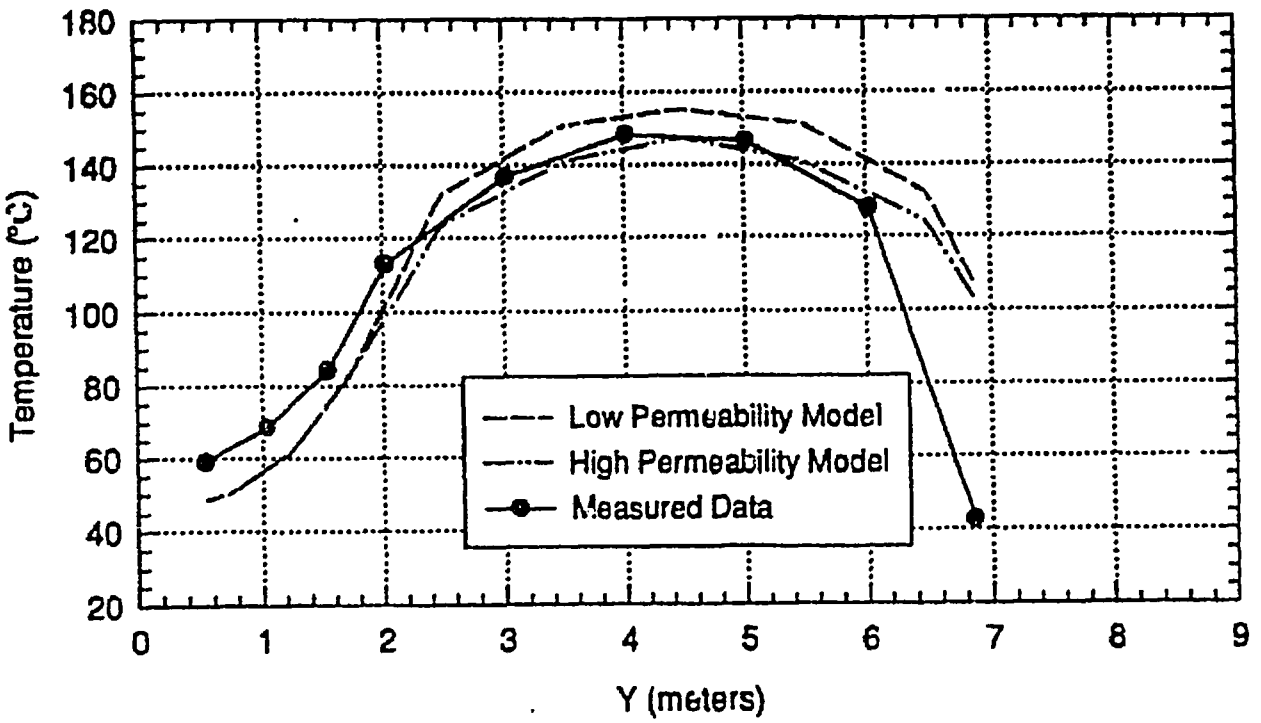

Figure 4-14. Predicted and Measured Temperatures Corresponding to TMA-BX-1-TC

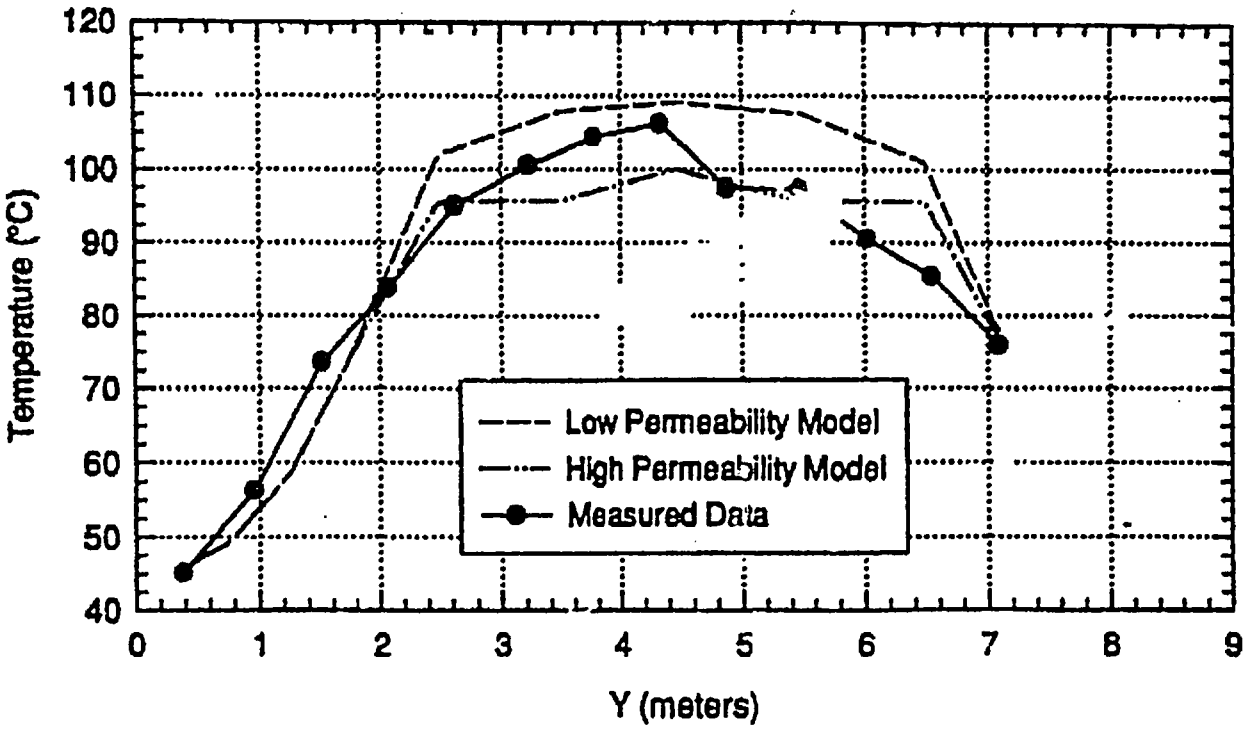

Figure 4-15. Predicted and Measured Temperatures Corresponding to TMA-BY 2-TC

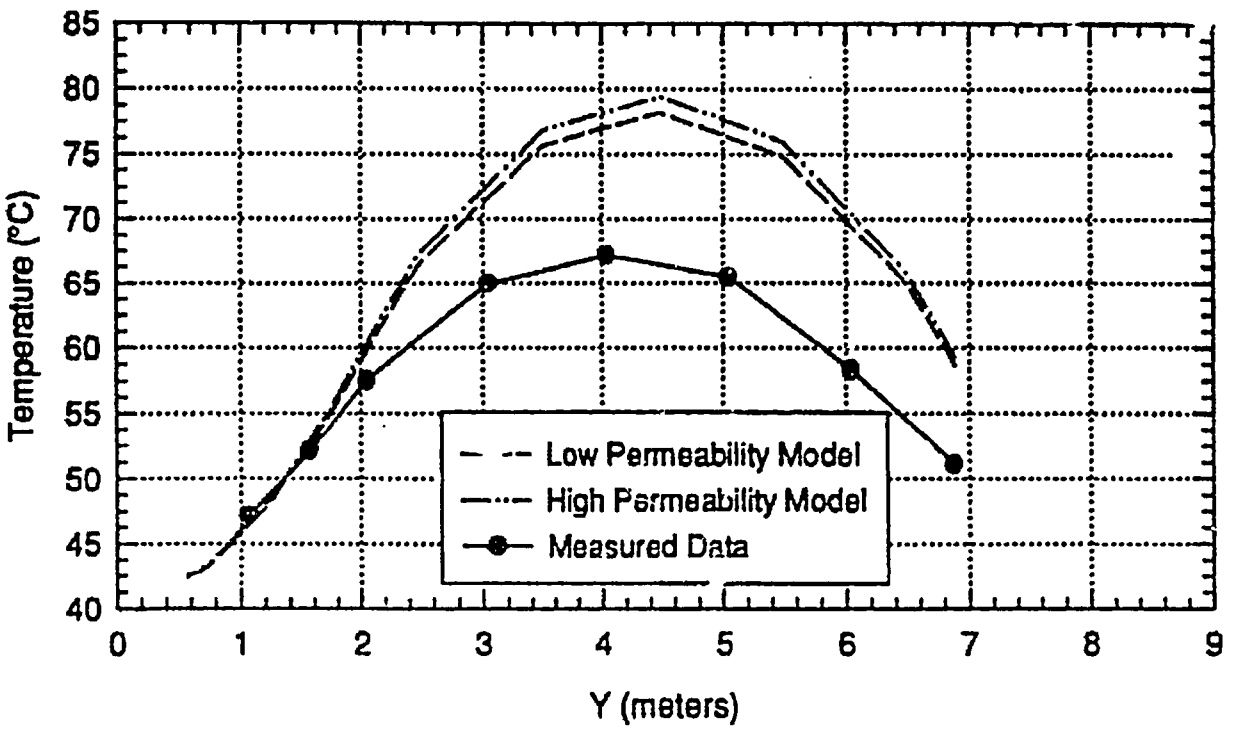

Figure 4-16. Predicted and Measured Temperatures Corresponding to TMA-BX-3-TC

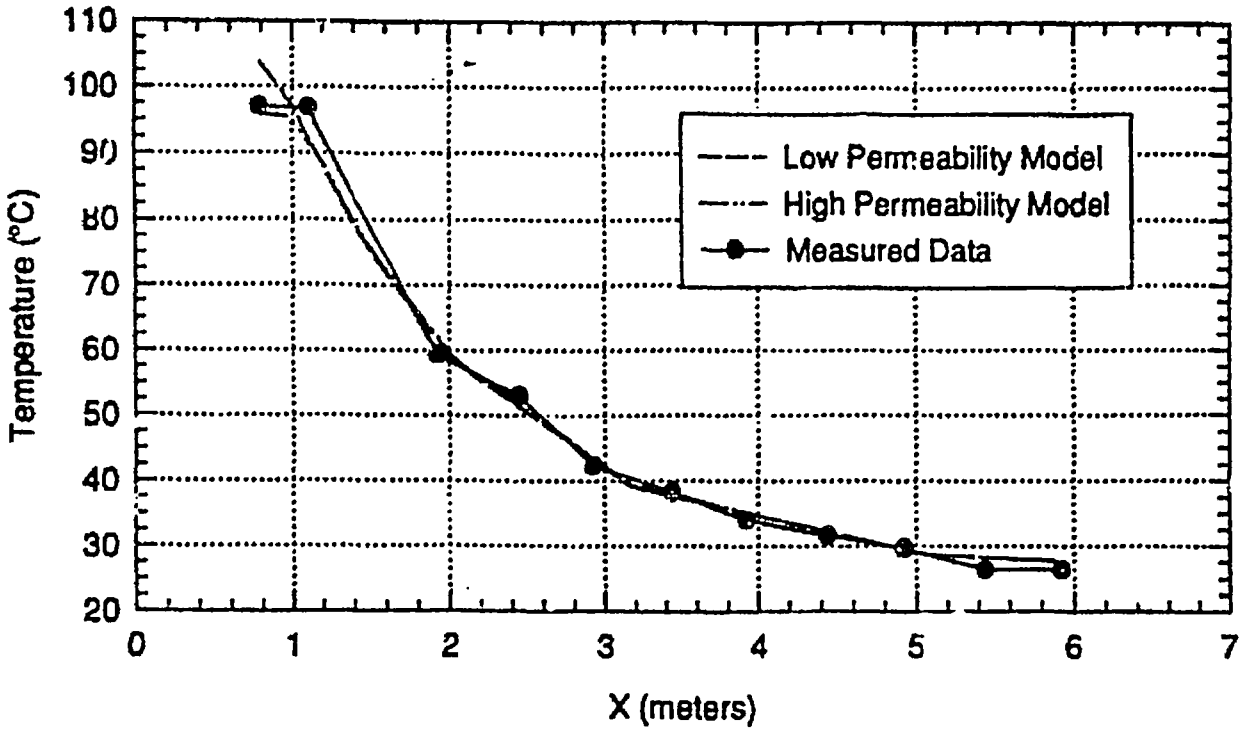

Figure 4-17. Predicted and Measured Temperatures Corresponding to TMA-BX-4-TC

For the low permeability case, the effects of vapor phase heat transport are much less. There is a slight inflection in the radial temperature distribution, but an isothermal annular region does not exist as it does in the high permeability case. When the temperature, at a given location, in the low permeability model reaches the boiling point, a small portion of the water in the pore space evaporates but cannot readily escape from the pores because of the low permeability. The inhibition of vapor phase heat transport from low permeability substantially reduces the heat flux away from the heated region when compared to the high permeability case, thereby producing higher rock temperatures near the heat source. However, some vapor phase heat transport still occurs which explains the slight reduction in the predicted radial temperature gradient compared to that from a solely conductive model. The temperature can increase above 96°C even though water and steam coexist in this region because the increased gas pressure raises the pore pressure substantially, thereby also raising the boiling point.

Two prominent characteristics of the comparison of predicted and measured data exist. The first is that predicted temperatures are too high at radial distances from the heater greater than 0.8 meters, where the temperature is below the boiling point. A plausible explanation for these high temperatures is a low thermal conductivity for the rock in the sub-boiling portions of the block. Low thermal conductivity inhibits conductive heat transport away from the heated region resulting in higher temperatures.

The second prominent characteristic in Figure 4-E is that the measured radial temperatures do not exhibit any appreciable inflection point at the boiling point as do the predicted radial temperatures. This observation implies that the models are allowing too much heat to escape from the SHF block which is below boiling, thereby depressing the modeled temperatures in regions above boiling. This

discrepancy between the predicted and measured temperatures is more severe for the high permeability case than for the low permeability case since radial heat transport away from the heated region is more enhanced by convective heat transport in the high permeability case than in the low permeability case.

The discussion so far has focused on the temperatures around probe TMA-TC-6. To compare temperatures from a more regional perspective, the low permeability case temperature was interpolated at every gage location in the interior of the SHT block and then the measured temperature was subtracted from it. The result is the difference between the predicted and measured temperatures after 96 days of heating (see Figure 4-18). Data from the four BX boreholes have been omitted in Figure 4-18. These thermal sensors are emplaced in open boreholes and intra-borehole vapor phase heat transport has significantly impacted these measured temperatures. Also omitted from Figure 4-18 are sensors located beyond the ends of the heater. The predicted and measured temperatures closely agree at temperatures less than 40°C, which are not surprising since the temperatures are not elevated much above ambient. In the range from 40 to 95°C, the predicted temperatures significantly exceed the measured temperatures, with a maximum discrepancy at about 80°C where the difference is about 17°C. As discussed previously, this thermal behavior probably reflects the use of a low thermal conductivity for wet rock. At temperatures above 100°C, the data and the models agree quite well. Given the elevated model temperatures at greater radial distance ranges, however, this agreement is considered both fortuitous and misleading.

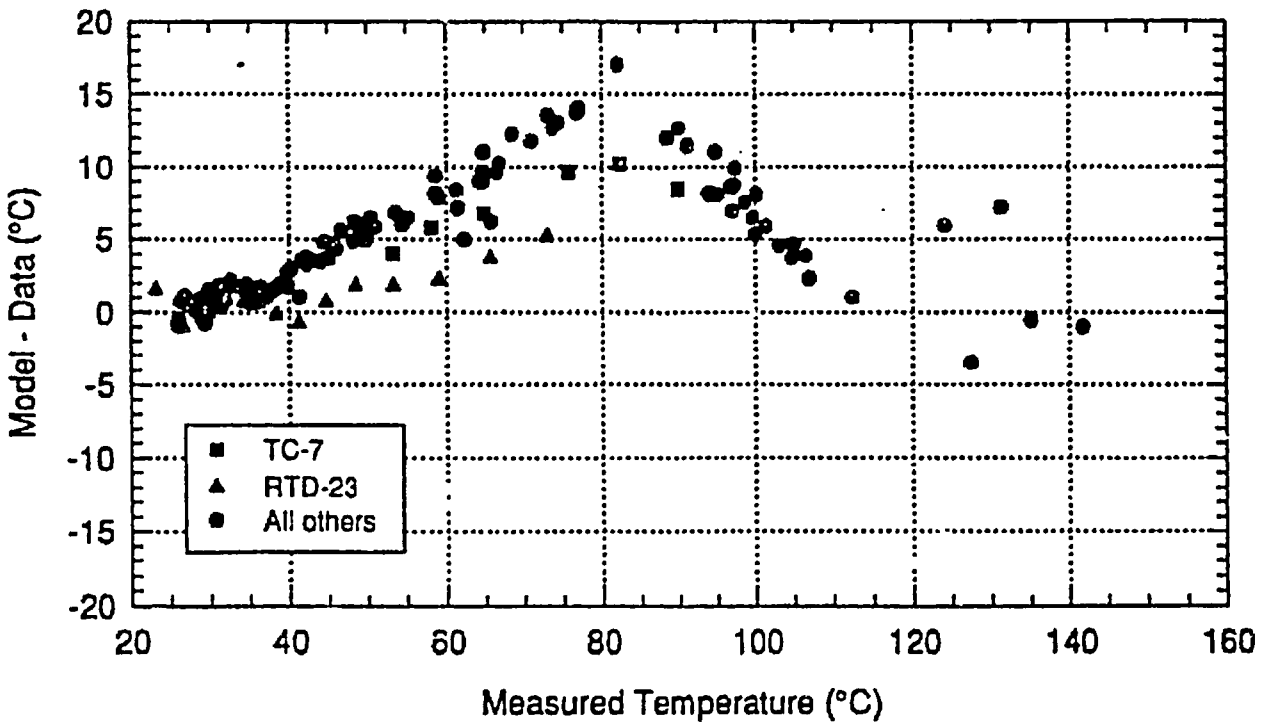

Figure 4-18. Comparison of Predicted and Measured Temperatures Along the Heater Axis (Kwet = 1.671 W/m-K)

To investigate the effect of increasing the wet thermal conductivity value, the low permeability model reported in SNL (1996) was rerun using a thermal conductivity of 2.1 $W m^{-1} °C^{-1}$ for wet rock. The new and old predicted temperature distributions at the location of probe TMA-TC-6 are compared in Figure 4-19. The higher thermal conductivity decreases the predicted temperatures by as much as 15°C for TMA-TC-6 which results in much better agreement. Note however that the change does not entirely remove the slight inflection in the predicted radial temperatures near the boiling point.

The discrepancy between the new model and the measured temperatures, as a function of the measured temperature, is illustrated in Figure 4-20. The use of a more appropriate wet thermal conductivity brings sub-boiling predicted temperatures into much better agreement with the measured temperatures. Above boiling, however, the discrepancy between the predicted and measured temperatures, which was minimal in the original model, is now substantial. The new model under predicts the temperature by as much as 15 to 20°C at the location of probe TMA-TC-1. This observation indicates that the model is allowing too much heat to escape from the region where the temperatures are above boiling. Currently, the cause of this discrepancy in behavior is pending more study. Changes to the models which might work include adjusting: the bulk permeability; the relative permeability of the gas phase as compared to the liquid phase; and/or the dry thermal conductivity of the rock.

In conclusion, the overall agreement between the predicted and measured temperatures is encouraging at this interim stage of the SHT. Heat conduction appears to be the primary mode of heat transfer throughout the SHT block. The early temperature data from the SHT block do not appear to exhibit significant convective heat transfer. Nonetheless, the models, even the low permeability cases, are influenced by heat convection. After the effects of increasing the wet rock thermal conductivity in the model are considered the numerical models predict temperatures in the sub-boiling regions quite well but they significantly under predict the temperatures in the above boiling regions. Numerical simulations, which are currently underway, will investigate this disparity including a more in-depth assessment of appropriate ranges of thermal and hydrologic rock properties. It is anticipated that the bulk permeability of the rock in the region of the block at or above boiling is substantially lower than originally estimated; lower even than the bulk permeability used in low permeability pretest models. A plausible explanation for a lower bulk permeability is that the fracture permeability of the rock has been substantially reduced during the heating process as a result of fracture closure from thermal expansion of the rock and/or chemical precipitation.

4.2 MECHANICAL

The thermomechanical predictions were described in Sobolik et al. (1996) and the thermomechanical measurements documented in Sobolik et al. (1996). Details regarding the thermomechanical predictions and measurements should be referred to the original sources. Preliminary estimates of rock mass thermal expansion are given for different temperatures and scales. Because the comparisons encompasses only the first three months of heating, the comparison of predicted and measured TM behavior is considered preliminary. More detailed analyses and discussions are planned when a complete set of measured data becomes available. This discussion will focus on displacement comparisons and then discuss the other TM measurement results.

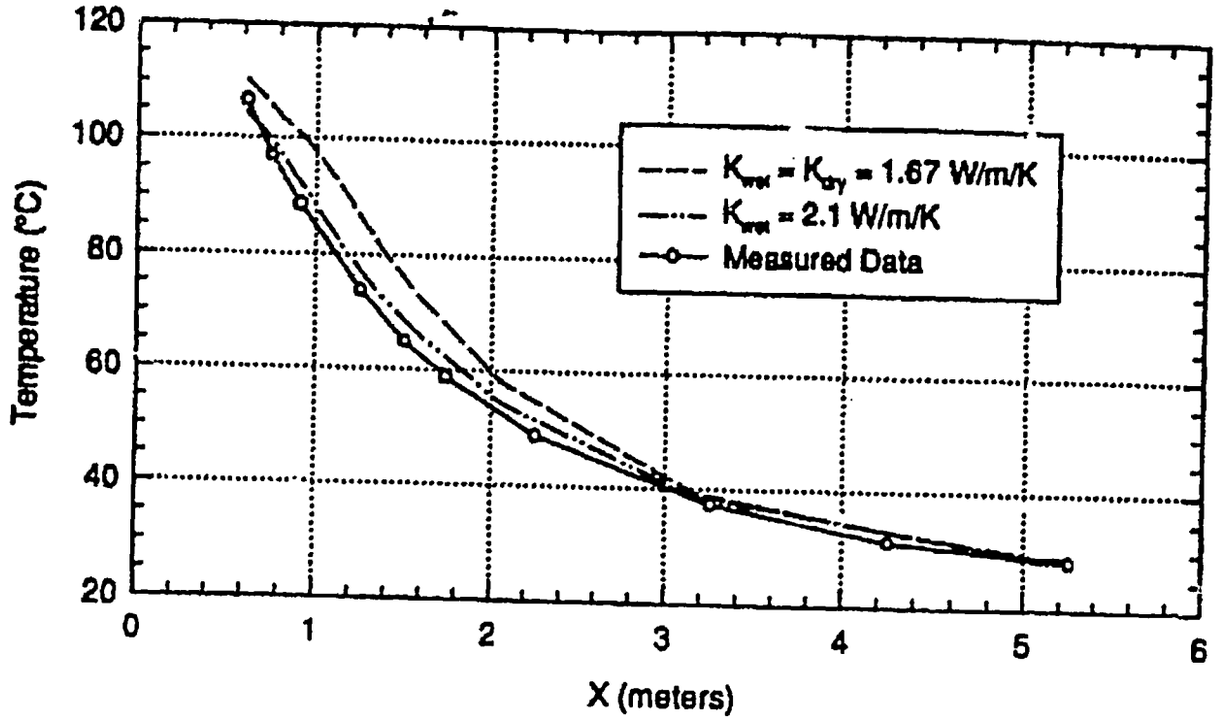

Figure 4-19. Evaluation of Thermal Conductivity at TMA-TC-6 (Low Permeability Case)

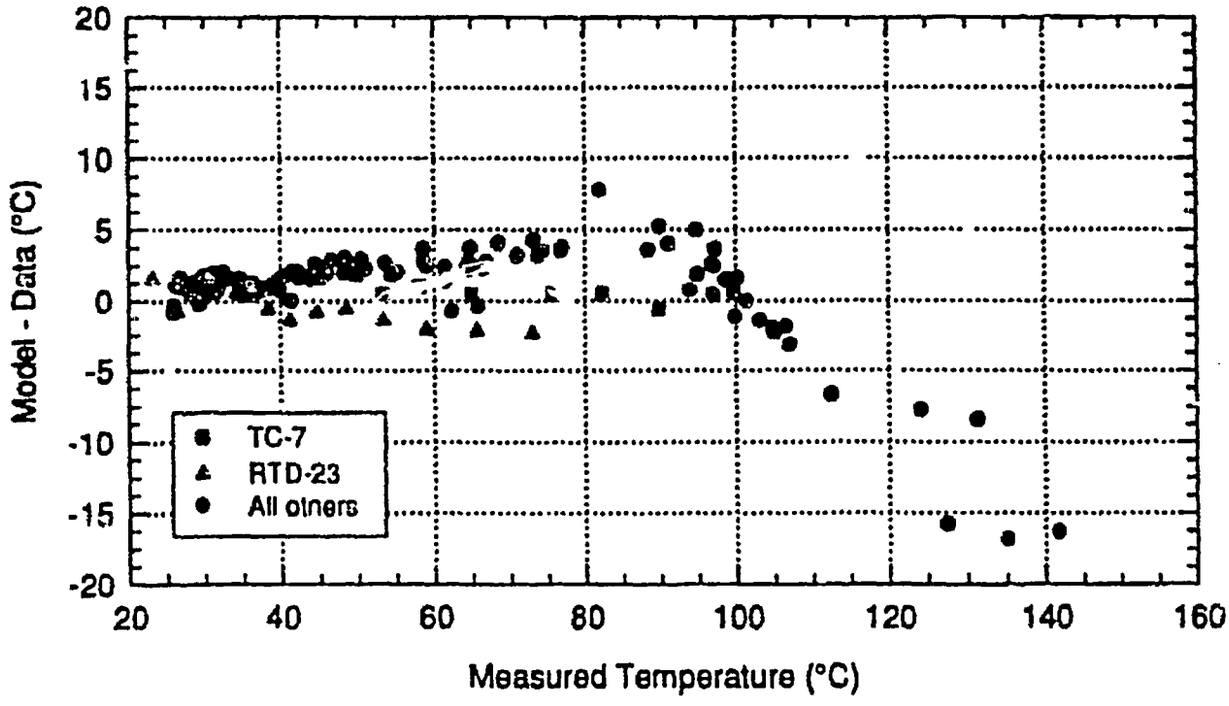

Figure 4-20. Comparison of Predicted and Measured Temperatures Along the Heater Axis (Kwet = 2.1 W/m-K)

The displacements measured using the TM instrumentation are caused by both ambient-gravity driven and thermally-driven processes. Because the numerical analyses incorporate both processes, the following discussion will not differentiate between them. In some cases, the two processes are additive (e.g., MPBX displacements and tape extensometer displacements) in which both processes will tend to cause rock mass to move toward the excavations. In other cases the processes compete with each other (e.g., wire extensometers) in which the thermal component tends to extend the block vertically, and the gravitational component tends to compress the block. The following discussion will compare predictions and measurements for two of the four MPBXs (MPBX-3 and MPBX-4) which should be representative of general rock mass TM behavior.

The predicted and measured displacements for MPBX-3 are shown in Figures 4-21 and 4-22, respectively, Figure 4-21 shows the measured displacements uncorrected for the thermal expansion of the extension rods (Note: Comprehensive corrections for thermal expansion are planned for subsequent analyses). The displacements corrected for rod thermal expansion would increase the measured displacement of the deepest anchor, TMA-BX-3-1 by about 0.32 mm and the shallowest anchor TMA-BX-3-6 by about 0.06 mm through day 96 (November 30, 1996). The plots show generally good correspondence between the predicted and measured displacements with differences of less than about 20 percent for anchor TMA-BX-3-1 after accounting for rod thermal expansion. The discrepancy is greater between the predicted and measured values for the shallowest anchor TMA-BX-3-6 where the predicted value is low by about 50 percent. The general displacement relationship at various anchor locations compare closely with the deepest anchor showing the greatest displacement, the shallowest anchor the least, and intermediate anchors aligned according to their relative position in the borehole. Also, the measured displacements exhibit the same general reduction in the rate of change as is shown in the predicted values. Possible reasons for these differences will be discussed later.

The predicted and measured displacements for MPBX-4, which is horizontal and oriented perpendicular to the heater, is of much interest. The predicted and measured displacements are shown in Figures 4-23 and 4-24. Predicted and measured displacements corrected for rod thermal expansion would increase the measured displacement of the deepest anchor, TMA-BX-4-1, by about 0.22 mm and the shallowest anchor TMA-BX-4-6 by about 0.02 mm through day 96 (November 30, 1996). The figures show good agreement between the predicted and measured displacements. The general displacement relationship between the various anchors indicate the deepest anchors have the greatest displacement, the shallowest anchor the least displacement, and intermediate anchors aligned according to their relative position in the borehole.

The general relationships between the measured and predicted behaviors of anchors TMA-BX-4-1 and TMA-BX-4-2 is noteworthy. Initially, TMA-BX-4-1 sees the most compression followed closely by TMA-BX-4-2. After about 15 days, the compression of TMA-BX-4-2 overtakes TMA-BX-4-1. At about day 15 anchor TMA-BX 4-1 begins to experience general extension. Anchor TMA-BX-4-2 continues to experience compression until about day 21 and then reverses to extension. Similar behavior is exhibited by the remainder of the MPBX-4 anchors. As discussed in Sobolik et al., (1996) and SNL (1997), the initial predicted and measured compression in MPBX-4 could be from thermally driven compression in the confined rock in the heated region around the heater. The outer anchors do not move because the driving forces from the thermal expansion have

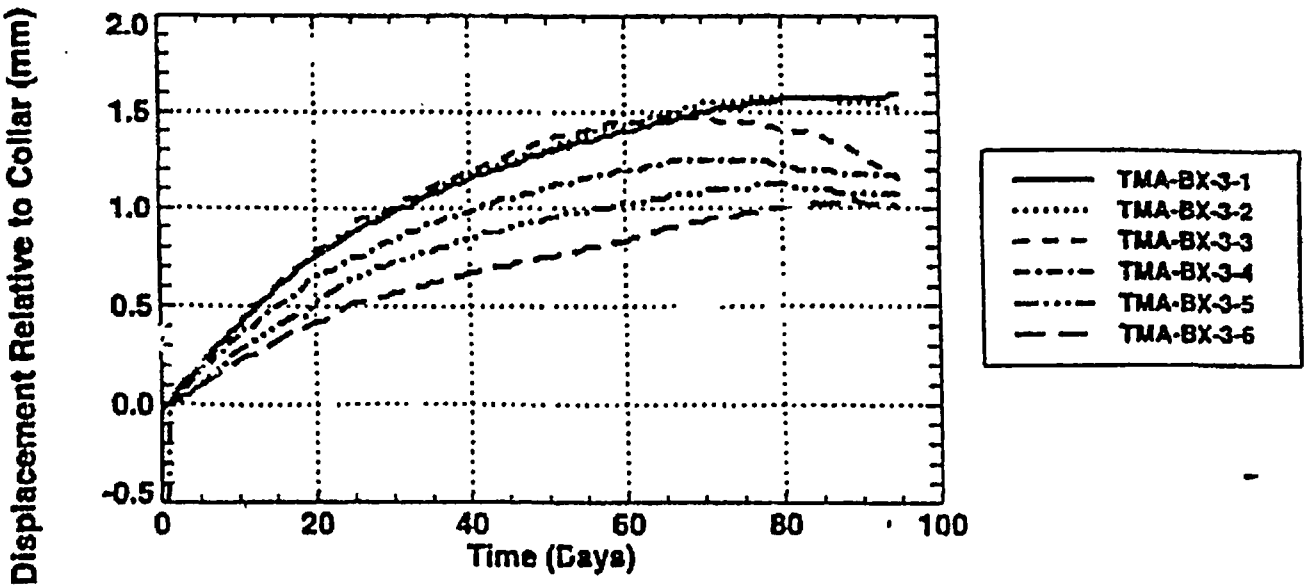

Figure 4-21. Displacements for TMA-MPBX-3 (Uncorrected for Thermal Expansion of Rods; Extension Being Positive)

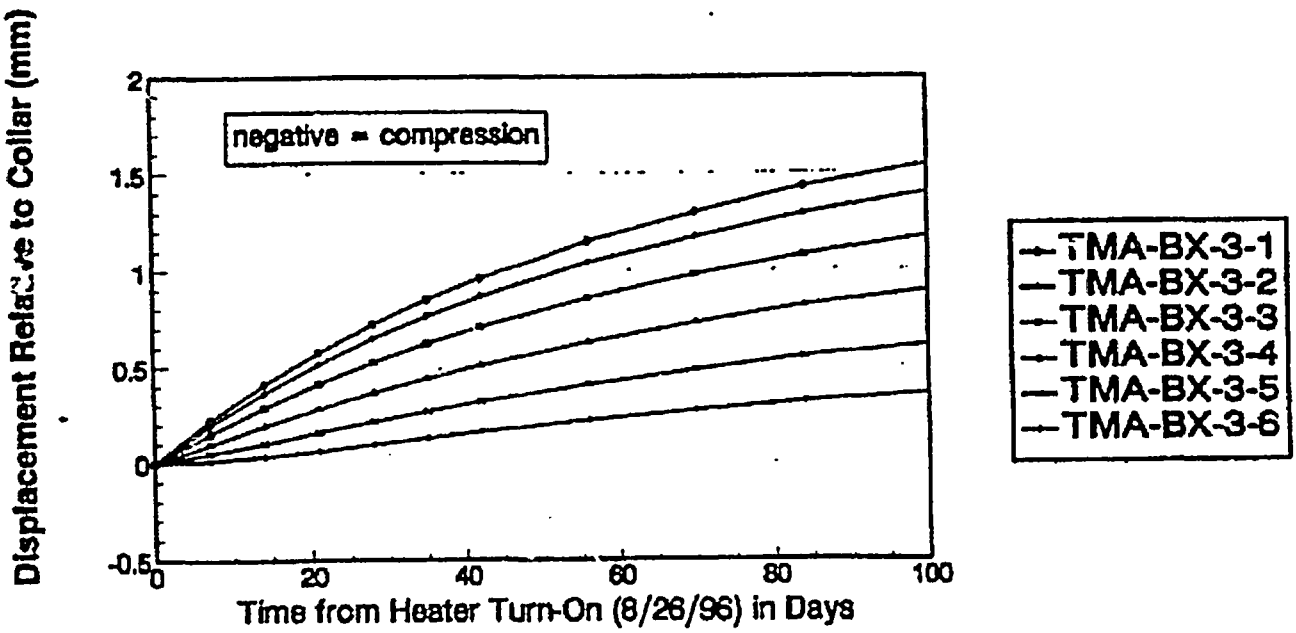

Figure 4-22. Predicted Displacements for TMA-MPBX-3 (High Permeability Case)

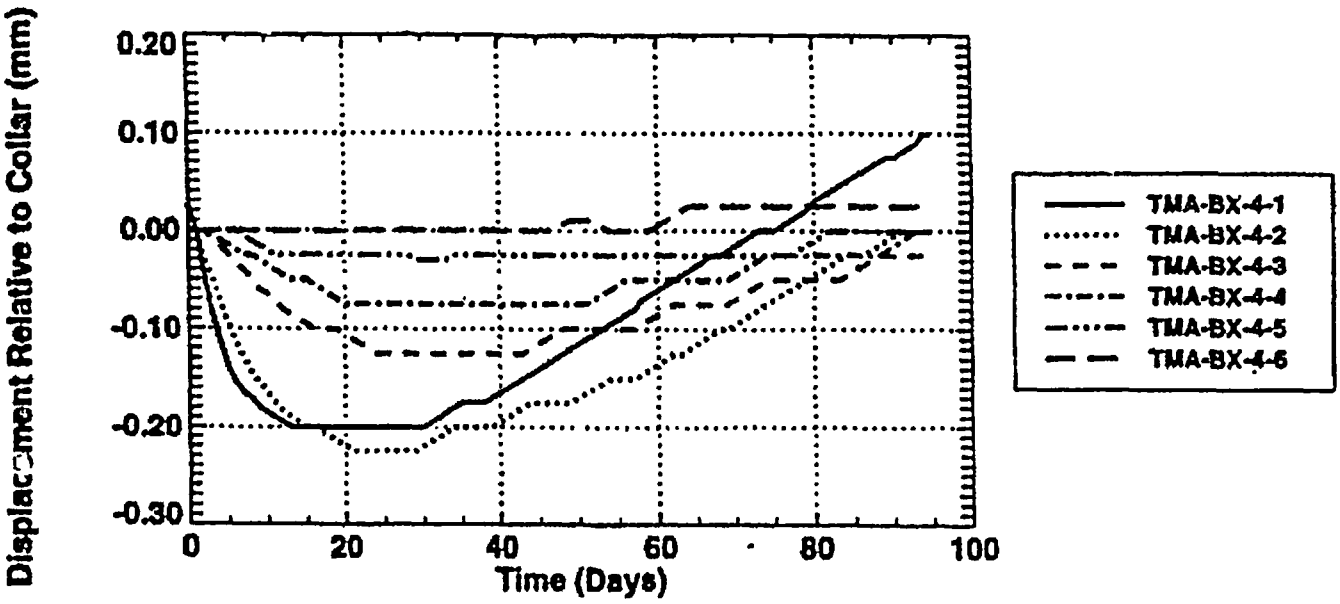

Figure 4-23. Measured Displacements for TMA-MPBX-4 (Uncorrected for Thermal Expansion of Rods; Extension Being Positive)

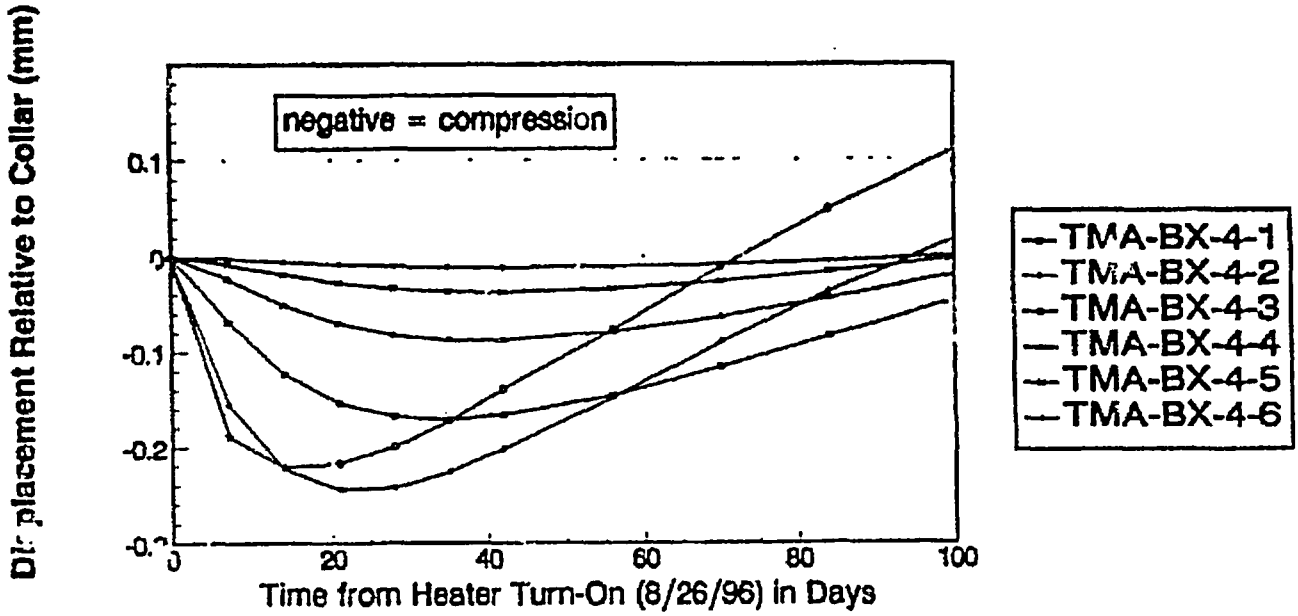

Figure 4-24. Predicted Displacements for TMA-MPBX-4 (High Permeability Case)

not yet reached them. The close correspondence between the predicted and measured MPBX-4 response suggests that the general TM model is adequately describing the rock mass behavior.

The vertical displacements measured using the wire extensometers exhibit erratic behavior as described in SNL (1997). The predicted displacements display relatively smooth displacements with all wire extensometers exhibiting net extension with the greatest extension measured by WX-1 and WX-2. These wire extensometers are located on the western face of the SHT block. The actual wire extensometer measurements are not nearly so smooth. Figures 4-25 through 4-27 show the predicted displacements for all wire extensometers and the measured displacements for WX-1 and WX-2. The measurements are typical of the wire extensometer data with displacement jumps which likely result from discrete block movement near the surface. In fact, three of the six wire extensometers exhibit net compression which is not shown in the model results. As previously stated, the wire extensometers are influenced by the competing processes of the thermal expansion driven extension and the gravity driven compression of the SHT block. Also, the wire extensometers are mounted on shallow pins which can be highly influenced by block rotation and other surface mechanical processes.

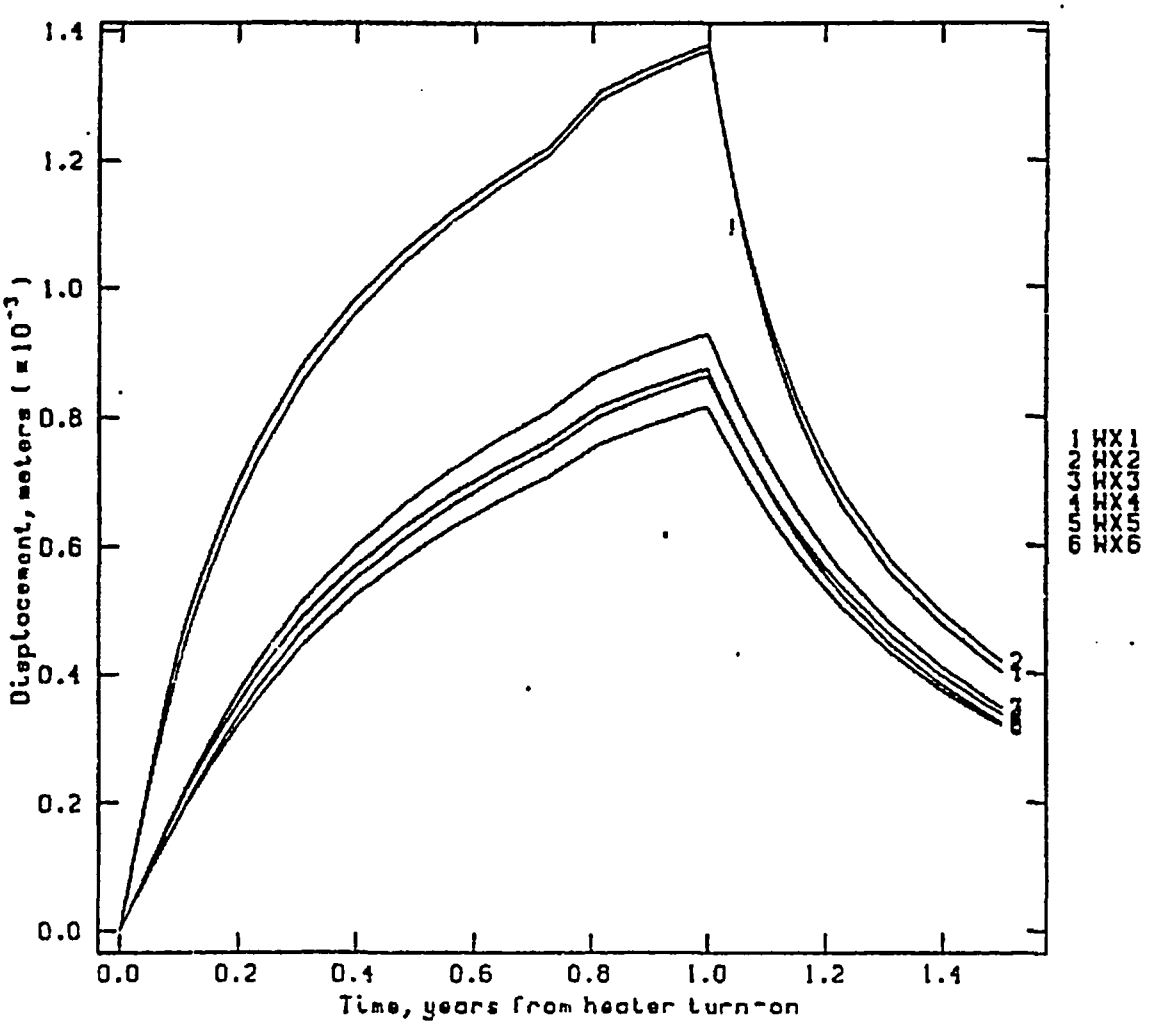

Figure 4-25. Predicted Displacement for the Vertical Wire Extensometer (High Permeability Case/12 Months of Heating Followed by Cooling/positive Displacement Means Elongation)

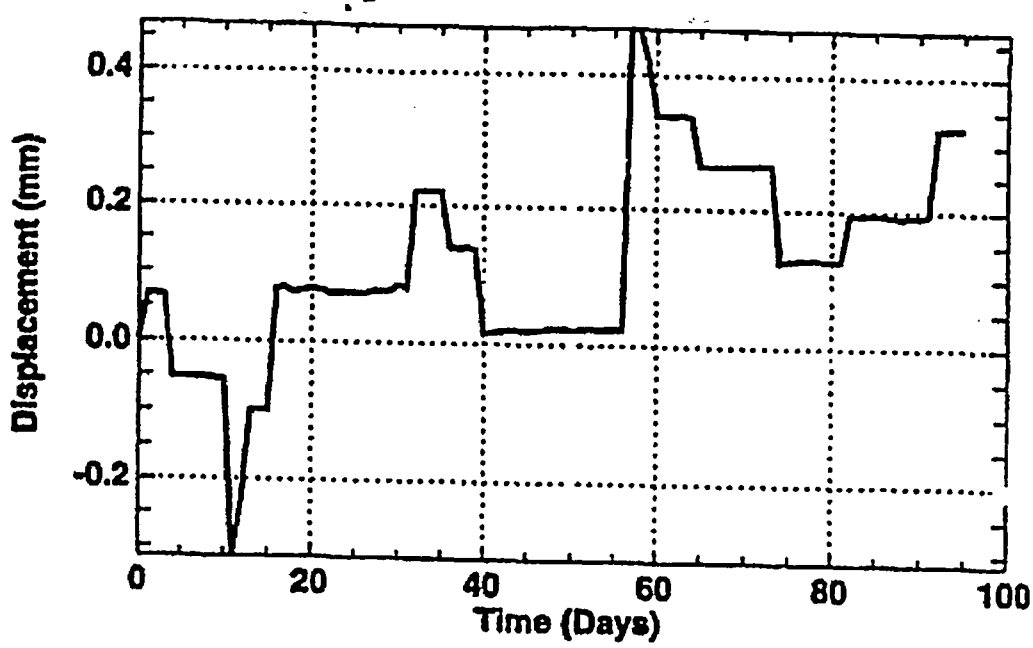

Figure 4-26. Measured Displacements for Wire Extensometer TMA-WX-1 (Extension Positive)

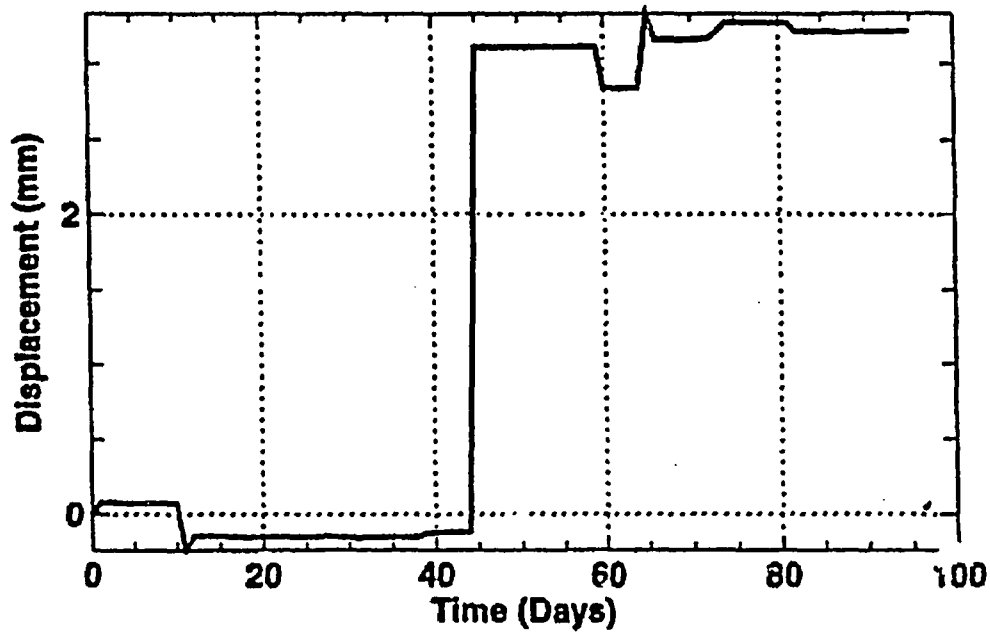

Figure 4-27. Measured Displacements for Wire Extensometer TMA-WX-2 (Extension Positive)

The horizontal measured displacements using the tape extensometer exhibit similar erratic behavior to the wire extensometers. Details regarding the tape extensometer measurements are described in SNL (1997). Expectantly, the predicted tape extensometer displacements are relatively smooth with all tape extensometer stations exhibiting net compression and the greatest compression measured by WX-1 and WX-2 which are located on the western face of the SHT block near the heater borehole collar. The tape extensometer measurements are not nearly so smooth or regular. Figures 4-28 and 4-29 show the predicted and measured displacements for all tape extensometer stations, respectively. The measurements are typical of surface mounted pin data with small displacement jumps likely resulting from discrete block movement near the surface. With the exception of WXM-2, all the tape extensometer measurements are relatively small (less than one mm). However, the measured values are in general agreement in which WXM-1 and WXM-2 exhibit the greatest displacement.

Additional Discussion

Thermomechanical data obtained during the SHT include preliminary estimates of rock mass thermal expansion, rock mass modulus, and rock bolt load. The rock mass thermal expansion coefficient is determined from selected MPBX displacements and temperatures. The rock mass modulus is determined directly from the Goodman jack measurements. The rock bolt load is measured directly using rock bolt load cells, and comparisons between the thermally perturbed and ambient bolts are made.

Rock mass thermal expansion was estimated for the pretest numerical analyses (Sobolik et al., 1996) based on unconstrained laboratory tests on welded tuff samples obtained from the SHT block. These laboratory values ranged from 7.47 10^{-6}/°C for temperatures of 25°C-50°C to 51.7 10^{-6}/°C for temperatures of 275°C-300°C. The very high thermal expansions reported for the intact lab specimens represent the effect of the silica phase transition. It is unlikely that these high temperatures will be seen by any thermomechanical instrumentation installed in the SHT. It is more likely that the maximum temperatures at thermomechanical instrumentation locations will approach 225°C. The intact thermal expansion reported for temperatures between 200°C and 225°C is 15.86 10^{-6}/°C. Therefore, realistic bounding values for the intact rock thermal expansion is 7.47-15.86 10^{-6}/°C. Rock mass thermal expansion calculated from the in situ data is likely to be lower than the laboratory values because of the presence of fractures. The fractures would tend to accommodate some of the thermal expansion in the joint stiffness, particularly early during heating because there would be insufficient thermal displacement to mechanically close fractures (i.e. low stresses). Also, the three-dimensional effects of heated rock bounded by lower temperature rock would decrease the net effect of thermal expansion by resisting the thermal displacements in adjacent volumes of rock.

Rock mass thermal expansion is calculated from the in situ data including temperature change for a given axial length from ambient, gage length, and measured thermal displacement over the gage length. The rock mass thermal expansion coefficient was calculated for the SHT from selected data from TMA-MPBX-1 and TMA-MPBX-3. Only the data from these MPBX's with relatively uniform temperature were used. The predicted values for rock mass thermal expansion are presented in Table 4-1 for data from day 96 (November 30, 1996).

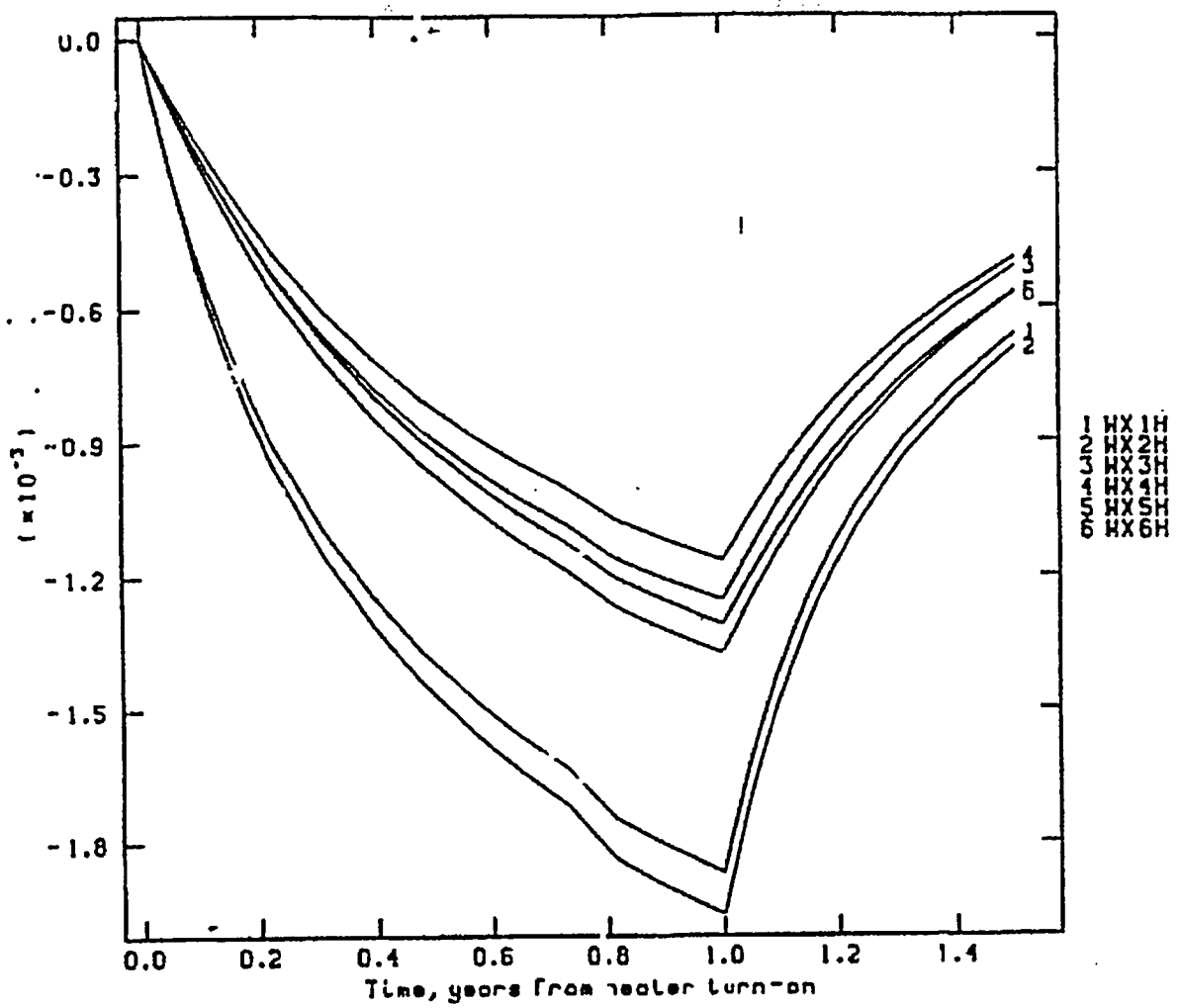

Figure 4-28. Predicted Displacements for the Horizontal Tape Extensometer (High Permeability Case/12 Months of Heating Followed by Cooling/positive Displacement Means Elongation)

The data presented in Table 4-1 are relatively consistent for most temperatures and gage lengths within the six anchors that comprise the MPBX boreholes. The data are averaged values for each MPBX over the gage lengths shown. For MPBX-1 the values ranged from 4.26-5.73 10^{-6}/°C, and for MPBX-3 they ranged from 3.91-6.32 10^{-6}/°C. The predicted values for rock mass thermal expansion are, as expected, lower than the values from intact laboratory specimens, and less than the values used in the pretest TM analyses. During the early stages of heating, the influence of transient fracture closings complicates comparisons between laboratory and field data. Also, the values presented in Table 4-1 are for the single orientation parallel to the heater (N72°W). It is possible that there could be some significant an isotropy in the rock mass thermal expansion coefficient from differences in fracturing along different orientations. These differences could be evaluated through future testing with gages aligned along other orientations. MPBX-4 installed perpendicular to the heater was not evaluated because the temperatures at the gage locations did not encompass a sufficient volume of rock as of day 96 (about 0.66m at about 96°C). MPBX-4 will continue to be monitored and data will be used in future comparisons to evaluate whether thermal expansion an isotropy is evident.

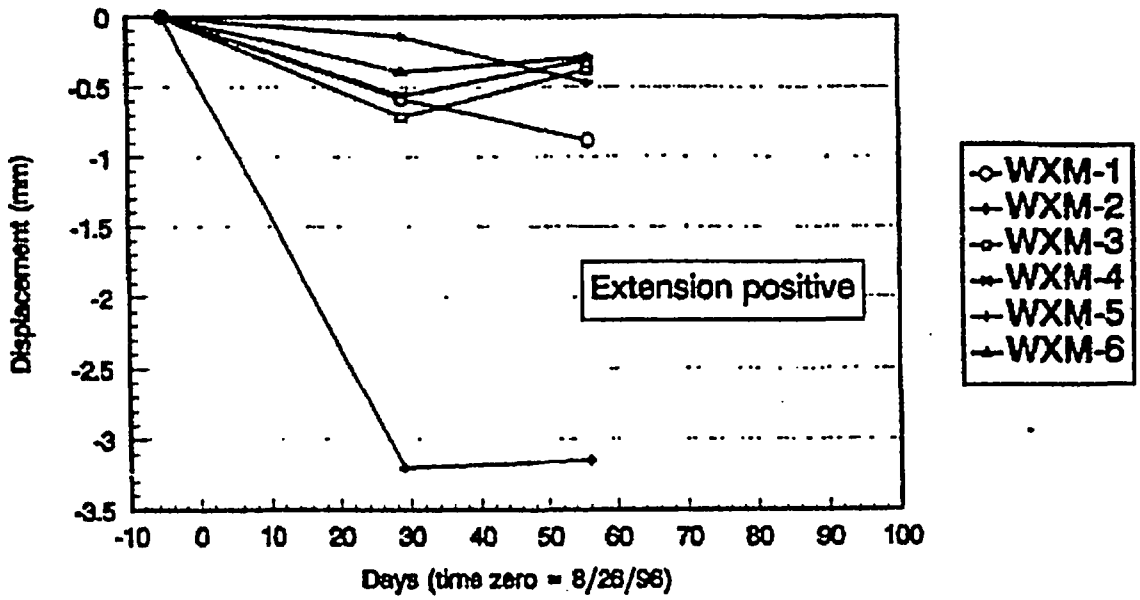

Figure 4-29. Measured Displacements for the Tape Extensometer Measurements

Table 4-1. Calculated Rock Mass Thermal Expansion Coefficient from SHT Data

MPBX # Identification	Average Thermal Expansion (10^{-6}/°C)	Average Temperature (°C)	Maximum Gage Length (m)	Orientation
TMA-MPBX-1	5.02	118.64	2.0	N72°W
TMA-MPBX-3	5.27	63.81	3.0	N72°W

Note: Data for day 96 (November 30, 1996)

The rock mass thermal expansion values presented in Table 4-1 are consistent within the six-anchor region of each MPBX, although slightly lower than expected values. Previous in situ thermal tests in G-Tunnel (Grouse Canyon tuff) measured thermal expansion coefficients of similar magnitude (8.0 10^{-6}/°C). although the intact values reported were lower than the intact values from samples taken from the SHT (Zimmerman and Finley, 1987). The thermal expansion coefficients from the SHT will continue to be evaluated which will include sensitivity analyses.

Rock mass modulus was measured in the SHT from a single borehole drilled horizontal and perpendicular to the heater axis. A Goodman jack was used to measure the rock mass modulus at various distances from the heater in a horizontal configuration in borehole ESF-TMA-BJ-1. Only horizontal measurements were made because this is the orientation of most interest to underground opening design and stability. For the pretest analyses, the rock mass modulus was estimated from laboratory tests on intact specimens from the SHT and by estimating the modulus from rock mass rating (RMR) data using the technique described in Serafim and Periera (1983). The rock mass modulus value suggested from these sources (upper bound value of 32.4 GPa) was used in the pretest

numerical analyses. The results of the Goodman jack testing is described in detail in SNL (1997), however, the calculated values ranged from about 3 GPa to 10 GPa with an *average value of about 7.5 GPa.*

The SHT Goodman jack testing through November 30, 1996 do not show any appreciable change from heating or location relative to the nearest excavation. The borehole is collared in the Observation Drift and extends about 5.7 m. This average value is significantly less than the value used in the pretest analyses (about 25 percent of the intact value). This lower modulus would result in the development of significantly lower stresses in the SHT block than the pretest analyses. However, the SHT displacements would not change in the elastic analyses with a reduced modulus. The reduction in the modulus from intact to rock mass conditions was expected. Previous in situ experiments conducted in welded tuff in G-Tunnel indicate that the modulus values measured in situ were about one-half the intact value which ranged between 23 and 35 GPa (Zimmerman and Finley, 1987). Zimmerman and Finley (1987) also report results of Goodman jack measurements in welded tuff from the G-Tunnel facility. Over 40 Goodman jack tests were conducted and the recommended rock mass modulus from these tests ranged from 14.7 GPa to 17.6 GPa, roughly 50 percent of the intact value from laboratory tests. Additional Goodman jack testing and analyses will be conducted to evaluate further the rock mass modulus from E-TMA-BJ-1 and its effect on overall SHT performance.

Loads were measured in rock bolts installed on both the heated side of the SHT Block and on the opposite ambient rib of the Thermomechanical Alcove. The rock bolts were installed to evaluate the longer-term effects of elevated temperature on this type of rock anchorage. Preliminary results show that loads are decreasing in all load cells, however, the decrease is greatest in those rock bolts on the heated side of the SHT. In particular, two bolts predicted to be at the highest temperature experienced the greatest load decreases (up to about 5.5 percent) from their initial preload values. The higher load decreases seen in the higher temperature rock bolts could be from several sources. For instance, the thermal expansion coefficient of carbon steel is about 10-11 10^{-6}/°C (Popov, 1976). Thus, the thermal expansion of the steel is likely greater than the rock mass expansion surrounding it. Alternatively, there could also be some load loss due to creep of the anchorage which is made up of the steel bolt and mechanical anchor, the surrounding grout, and the rock itself. Post-test evaluations, including pull tests and post-mortem testing of the bolt/grout/rock interface will provide more insight on rock bolt behavior.

4.3 HYDROLOGICAL

Since the most prominent TH response of the rock mass to the heater power output is the redistribution of moisture content, there are several modes of measurement to monitor the spatial variation and temporal evolution of the liquid saturation in the SHT block. These measurements include periodic surveys by neutron log in boreholes 15, 17, 22 and 23, and by electric resistivity tomography (ERT) in boreholes 24, 25, 26 and 27. In addition, boreholes 16 and 18 are installed with four inflatable packers and instrumented with pressure, temperature and relative humidity sensors. Temperature is also measured by resistance temperature devices (RTD) in the neutron logging boreholes 15, 17, 22 and 23. The temperature measured in bores 15, 17, 22, and 23 will be compared with that predicted by model calculations using three-dimensional NUFT code.

The thermal comparison will be included in Section 4.3.1. The humidity and gas pressure measurements in boreholes 16 and 18 will be discussed in Section 4.3.2. The moisture content measured by neutron logging and ERT will be compared with the predictions in Section 4.3.3.

4.3.1 Temperature

Figures 4-30 to 4-33 show the predicted and measured temperatures on January 26, 1997, which is about five months of heating, in boreholes 15, 17, 22 and 23, respectively. In these figures x=0 is the projection of the heater location. The peak temperature in borehole 15 is not exactly at x=0 because the borehole is inclined. The maximum difference between the predicted and measured temperatures is near x=0. The differences in temperature are about 12°C for borehole 17 and 8°C for borehole 15. These discrepancies are considered significant because temperature is usually the easiest parameter to predict. In general, the agreement between the calculated and the measured temperatures at x greater than 3.5 m is very good. Apparently, the discrepancy in the temperature calculations is largely from relatively low thermal conductivity (1.67 W/(m-K)) used in the calculations.

Zones 16-1, 16-2, 16-3, 16-4, 18-1, 18-2, 18-3, and 18-4 are instrumented with temperature sensors. These thermal sensors are relatively far from the heater and rise in temperature is moderate. The temperature monitoring data in these zones compare well with the TH simulations using TOUGH2 (LBNL, 1996). To illustrate this good agreement, the predicted and measured temperatures after 77 and 120 days of heating are listed in Table 4-2.

A plausible argument for the slight under prediction of temperatures in sensors 1,2,3 is that the thermal conductivity value of 1.67 W/m-K used in the simulations may be unreasonably low. This reduction affects the transient temperature distribution by overpredicting rock temperatures near the heater and underpredicting rock temperatures away from the heater.

On November 8, 1996 the temperature data from sensor 16-4 became erroneous. However, by November 15, 199' the sensor began to behave normally.

4.3.2 Humidity

Relative humidity is measured by humicaps in four zones in boreholes 16 and 18. Because of the borehole size, only four packers were installed in each borehole. The four zones in these boreholes are isolated by the inflated high temperature packers. Because of a highly fractured zone near the collar of those boreholes, a packer system was installed near the collar to seal those fracture zones. Zone 1 is near the collar; zone 4 is near the bottom of the borehole. The measured relative humidity as a function of time in those two boreholes are shown in Figures 4-34 and 4-35. The relative humidity in zones 1-3 in b h boreholes decreased from about 92 percent when the heater was energized to about 86-90 percent on about the 50th day of heating and then continued to increase. Active air injection tests carried out on November 25, 1996 caused a discontinuity in the responses of the sensors. In zone 4 however, the humidity decreased for a short period after the energization of the heater, then increased quickly to 100 percent. Based on the laboratory measurements conducted by Lin and Roberts (1997) greater than 50 percent water saturation is needed to generate a 100 percent relative humidity.

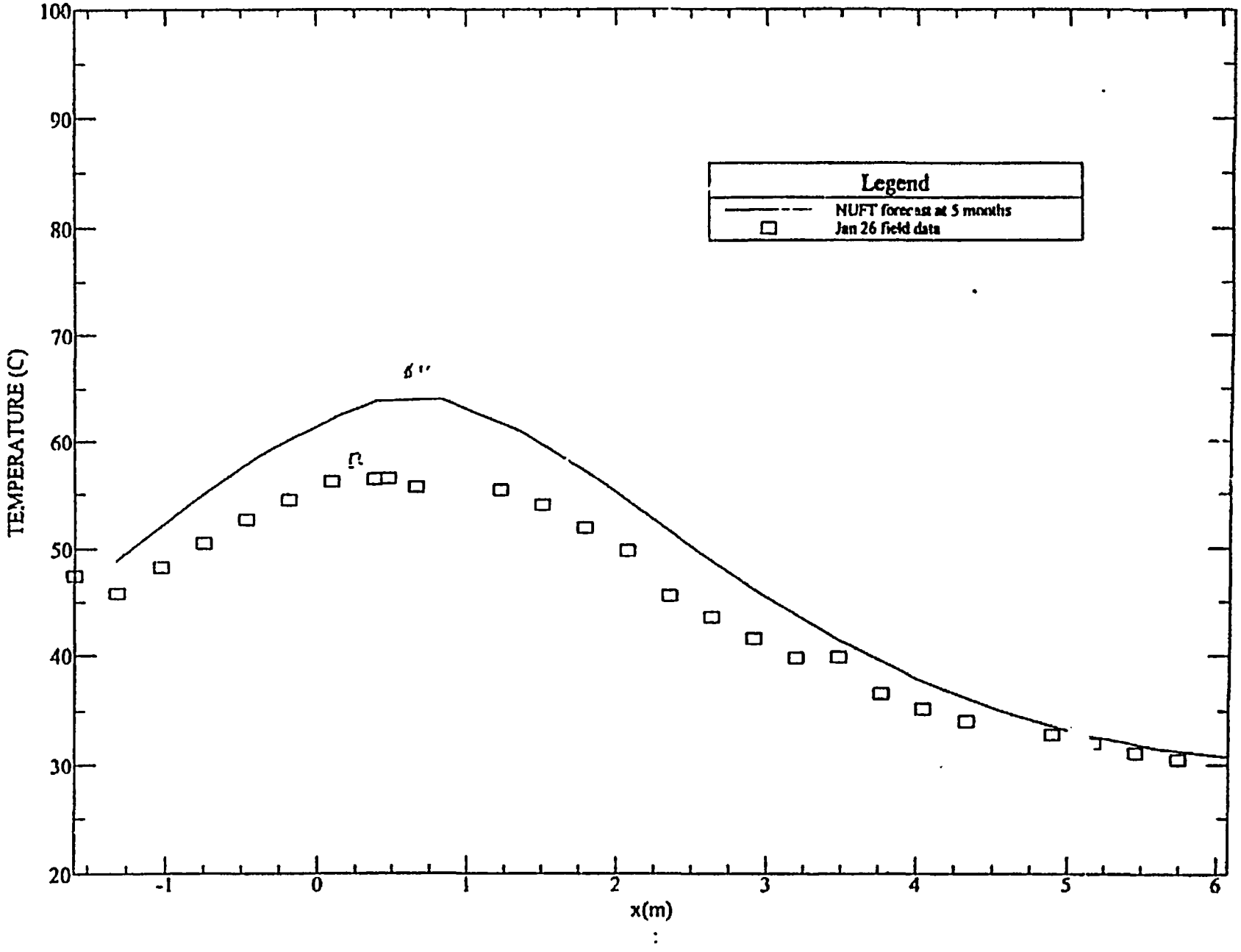

Figure 4-30. Comparison of Predicted and Measured Temperatures Along Borehole 15 after 5 Months of Heating (Three-Dimensional, Predictions, Thermo-Hydrologic, 12-Month Heating)

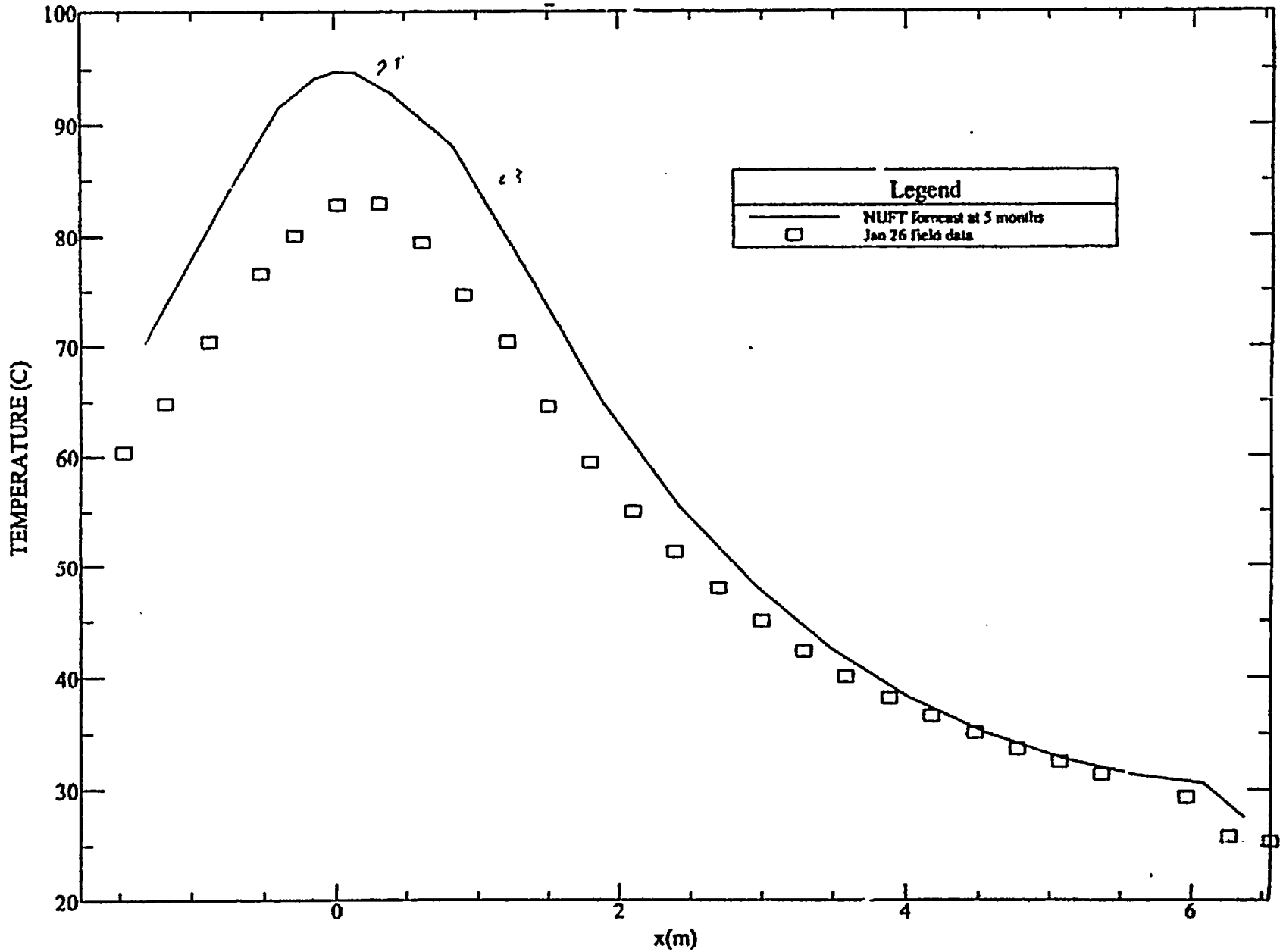

Figure 4-31. Comparison of Predicted and Measured Temperatures Profiles Along Borehole 17 after 5 Months (Three-Dimensional, Predictions, Thermo-Hydrologic, 12-Month Heating)

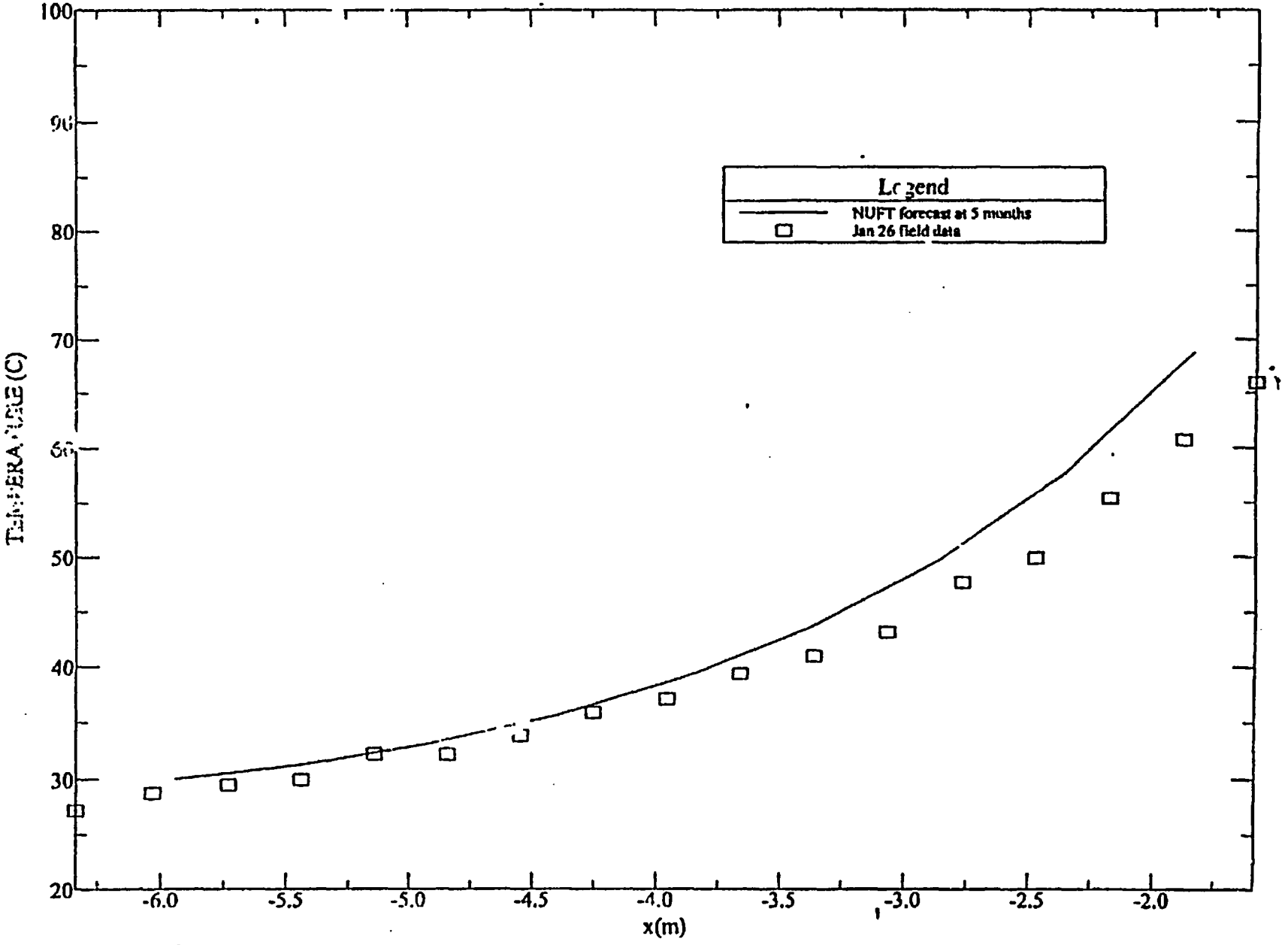

Figure 4-32. Comparison of Predicted and Measured Temperatures Along Borehole 22 after 5 Months of Heating (Three-Dimensional, Predictions Thermo-Hydrologic, 12-Month Heating)

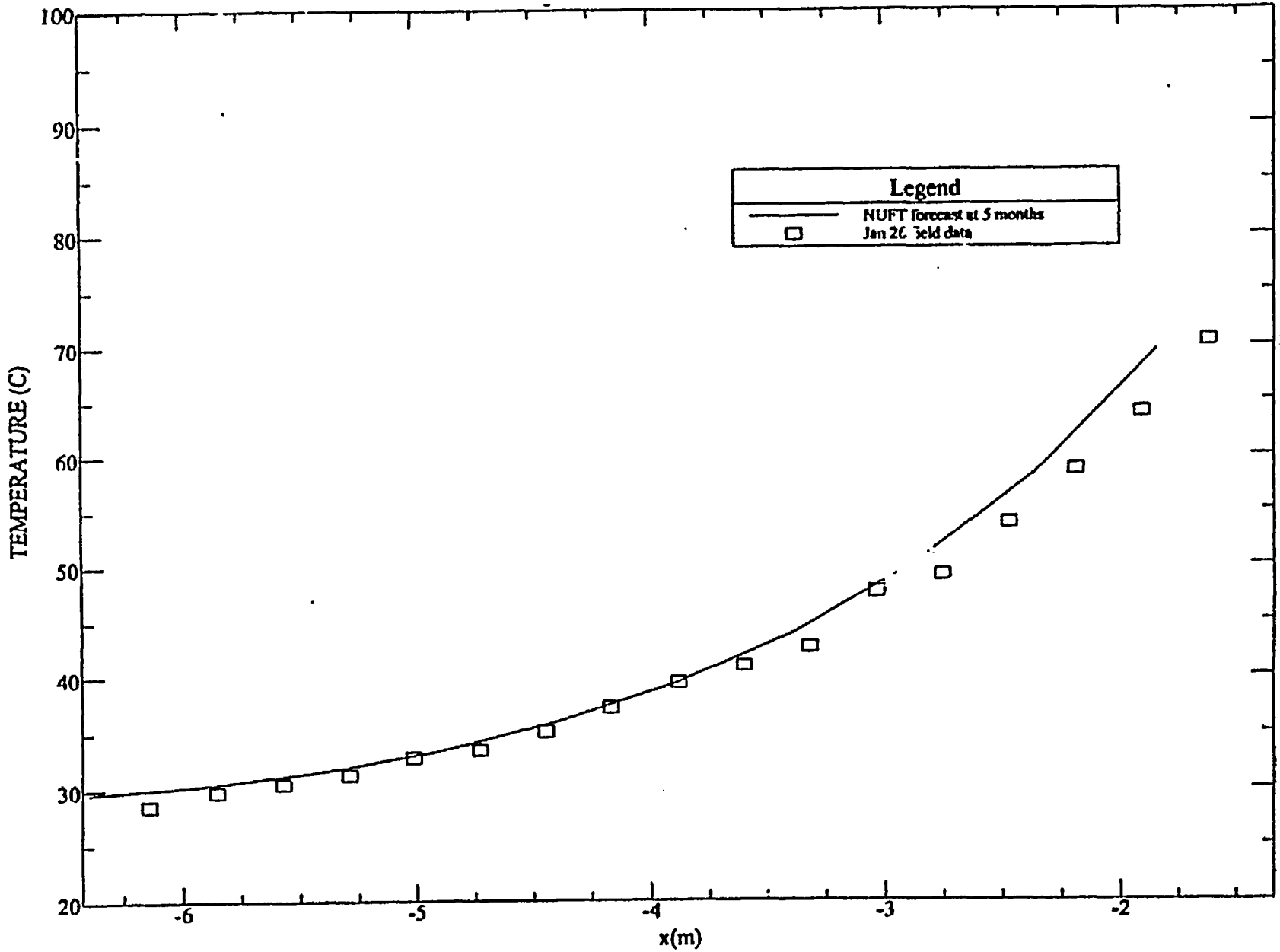

Figure 4-33. Comparison of Predicted and Measured Temperatures Along Borehole 23 after 5 Months of Heating (Three-Dimensional, Predictions Thermo-Hydrologic, 12-Month Heating)

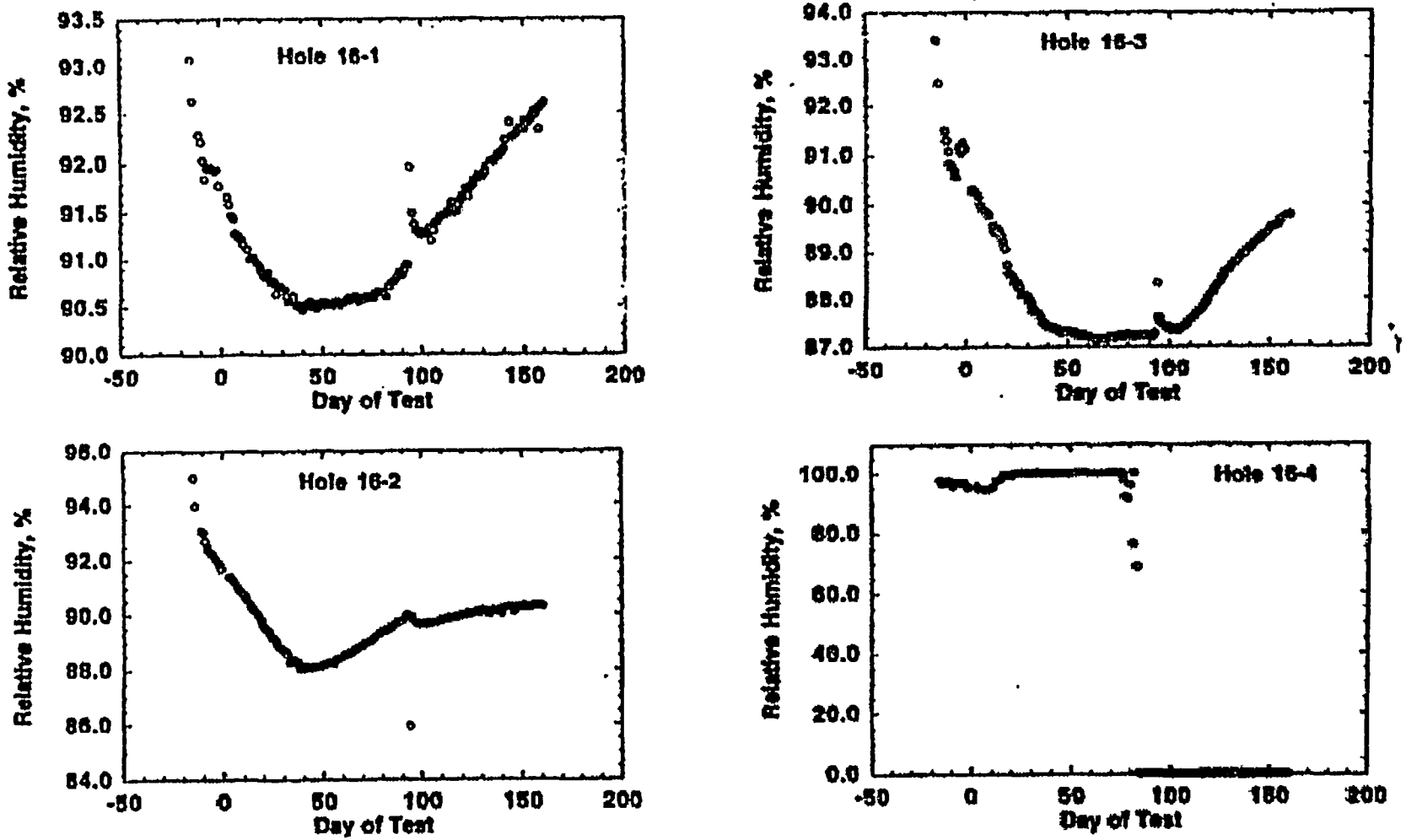

Figure 4-34. Chronology of Relative Humidity in Four Zones of Borehole 16

Table 4-2. Comparison of Predicted and Measured Temperatures after 77 and 120 Days of Heating

Sensors	Approximate Distance From Heater (m)	Temperature 77 Days	
		Predicted (°C)	Measured (°C)
18-1	5.1	28.0	28.8
18-2	4.4	29.8	31.0
18-3	3.7	33.6	34.8
18-4	3.0	40.5	40.5
		Temperature 120 Days	
18-1	5.1	29.5	31.5
18-2	4.4	33.5	34.0

The relative humidity is defined as the ratio of the vapor pressure and the saturation pressure where vapor pressure may be related to the capillary suction of the rock properties by means of the Kelvin's Equation. The relative humidity sensor is effective in monitoring very dry rock mass with strong capillary suction, but is not sensitive to normal liquid saturation unless the rock mass is very dry. Therefore, all sensors in boreholes 16 and 18 were anticipated to register 100 percent relative humidity before heater activation. Therefore, formal numerical analyses were not needed. Moreover, since the closest sensors (16-4 and 18-4) are approximately three meters from the heater, and based on the TH numerical simulations, lie outside the drying zone throughout the one year of heating, the humicap readings were anticipated to continue to register 100 percent.

The monitoring data show that by the first week of September 1996 the vapor phase in the monitoring zones in boreholes 16 and 18 have come into equilibrium with the liquid in the rock mass, and the humidity readings in sensors 16-4 and 18-4 stabilize to 100 percent. However, the first three sensors of each borehole remain constant in the range of 87 percent to 92 percent. Two plausible explanations were offered for the less than 100 percent readings: 1) the zones in which sensors 16-1, 16-2, 16-3, 18-1, 18-2 and 18-3 are located are communicating by the fracture porous medium with the adjacent drifts; and 2) the packers isolating the zones were slowly leaking. The second hypothesis was tested in mid-November 1996 at which time the inflation pressure for the packers in boreholes 16 and 18 were increased by 50 percent. Since the relative humidity readings would not stabilize to 100 percent, it is believed that the relative humidity readings from the first three sensors in each borehole are registering the drying from the drift. Indeed, tomographic images from the Ground Penetrating Radar (GPR) of the SHT block also indicate a drier region near the Observation Drift and the TMA Extension.

While all the relative humidity readings remain essentially constant in the first months of heating, on November 8, 1996, instability began to appear in sensor 16-4. It dropped to zero and then returned to 100 percent. After several cycles (on November 15, 1996), the reading in the relative humidity sensor 16-4 dropped to zero and never recovered. On November 25, 1996 while preparing

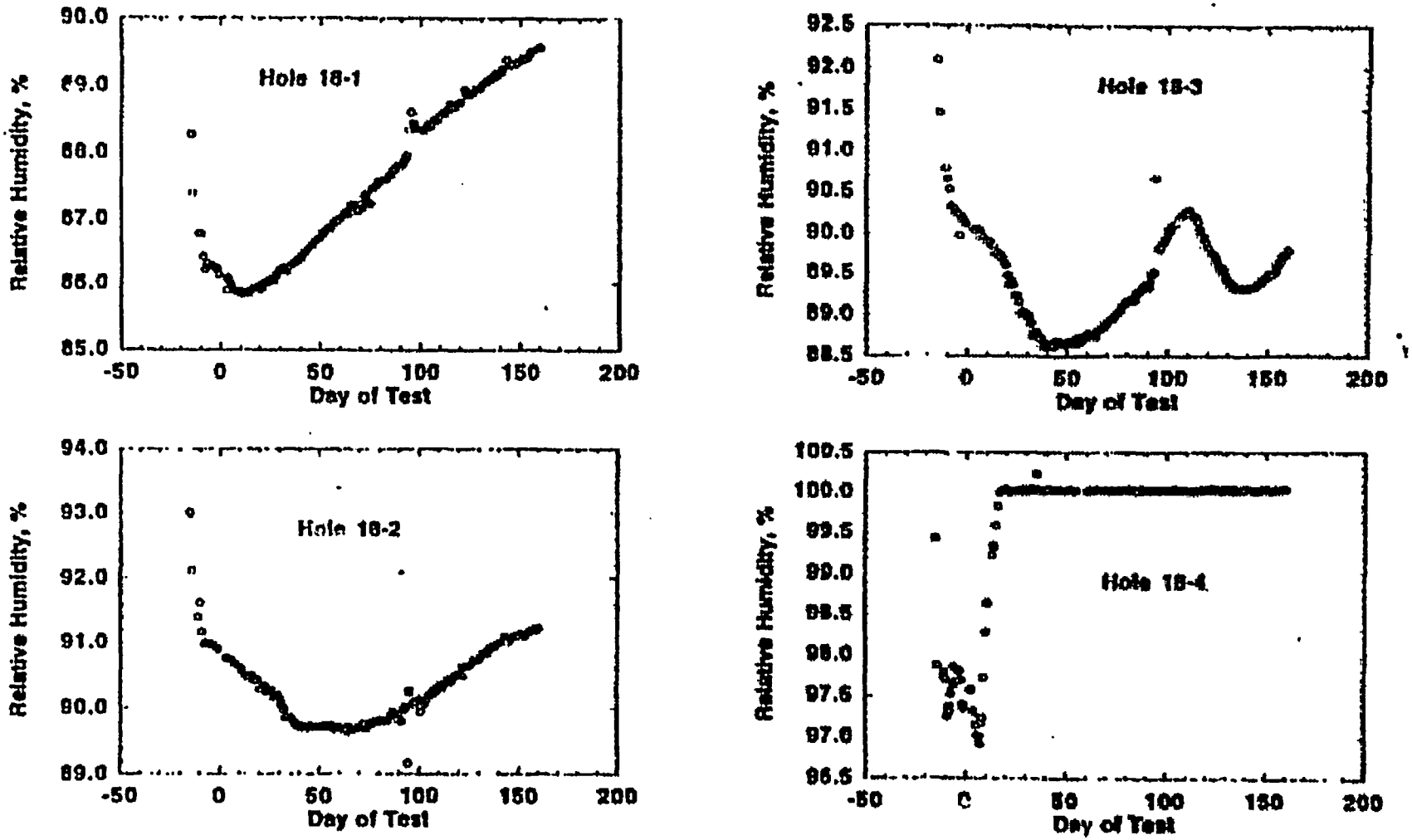

Figure 4-35. Chronology of Relative Humidity in Four Zones of Borehole 18

to conduct cross borehole air permeability measurements, fluid was noticed in an injection tube running into borehole 16 in zone 16-4. The water may have contributed to the failure of the relative humidity sensor 16-4. The gage pressure transducer in zone 16-4 also registered a slight decline since November 8, 1996.

Table A-1 gives the XYZ coordinates of the location of the sensors 16-1, 16-2, 16-3, 16-4, 18-1, 18-2, 18-3, 18-4. The approximate linear distance of these sensors from the heater is given by their X coordinates. Hence the approximate linear distance from the heater for sensors 18-1, 18-2, 18-3, and 18-4 are 5.1 m, 4.4 m, 3.7 m, and 3.0 m, respectively. The corresponding distances for sensors in borehole 16 are only about 0.1 m longer. During passive monitoring, the reading for each of the eight pressure transducers remain practically constant with time. Typically, the constant gage pressure of the different sensors are within a few KPa of each other, which is a very small fraction of the ambient pressure value of about 90 KPa. The near-ambient, constant pressure for all the sensors is consistent with the predicted results from TH numerical simulations. Simulations show that most of the expected pressure build-up is within one meter of the heater, and since even the sensors closest to the heater (18-4 and 16-4) are about 3.0 m from the heater, no pressure build-up is expected for the passive monitoring data in all the pressure sensors during the heating phase of the SHT.

The gas pressure transducers have an accuracy of better than 0.15 percent of the maximum rated pressure which is 50 psig. Therefore, the accuracy of the measured pressure should be within ±0.075 psig. Figures 4-36 and 4-37 show the gas pressures in boreholes 16 and 18, respectively. In borehole 16 there are no systematic trend in the variation of the pressures: zones 1, 3 and 4 show negative pressure (less than the atmospheric pressure in the alcove), zone 2 shows positive pressure, and the pressure in zone 4 decreases with time. An explanation for this behavior is pending more investigations. In borehole 18, however, the pressures are more systematic; the pressure in zones 1 to 3 are negative; and the pressure in zone 4 is positive. As mentioned above, zone 4 is the only one that a 100 percent relative humidity has been measured. These phenomena in borehole 18 may be from the flow of vapor into zone 4 which decreased pressures in other zones.

During active testing in the different zones separated by packers in boreholes 16 and 18, the change in the pressure response (at different stages of heating) reflects the change in liquid saturation in the rock mass. Simulations show that the majority of drying from the heater occurs within one meter of the heater, and both boreholes 16 and 18 are too short to sample this region of vigorous boiling and drying. However, the increase of liquid saturation from condensation occurs in the region of the two hydrology boreholes and should reduce air permeability or increase pressure for the same injection flow rate. The air injection tests performed at three months after heating demonstrates an increase in pressure reading heater over those tested before heater activation (see Sections 2.3 and 3.2).

4.3.3 Moisture Content

The moisture content in the heated block of the SHT is measured by neutron logging in boreholes 15, 17, 22, and 23 and ERT in the diamond-shape region bounded by boreholes 24 to 27. Neutron logging is designed to measure the moisture content in the rock mass along a borehole. The effective region of measurement is about 15 cm radius from the borehole. The region closest to a neutron tool

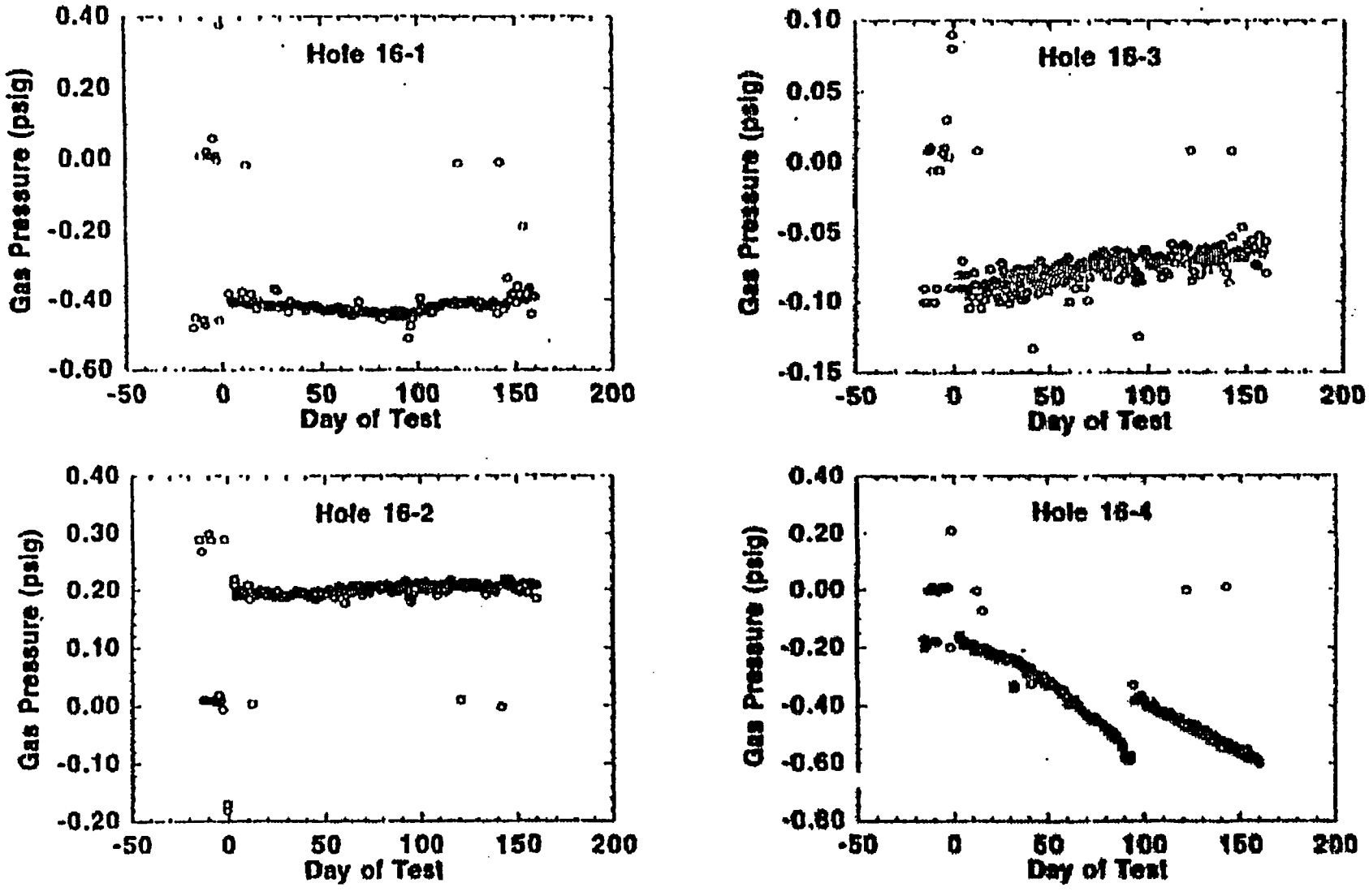

Figure 4-36. Chronology of Gauge Gas Pressure in Four Zones of Borehole 16

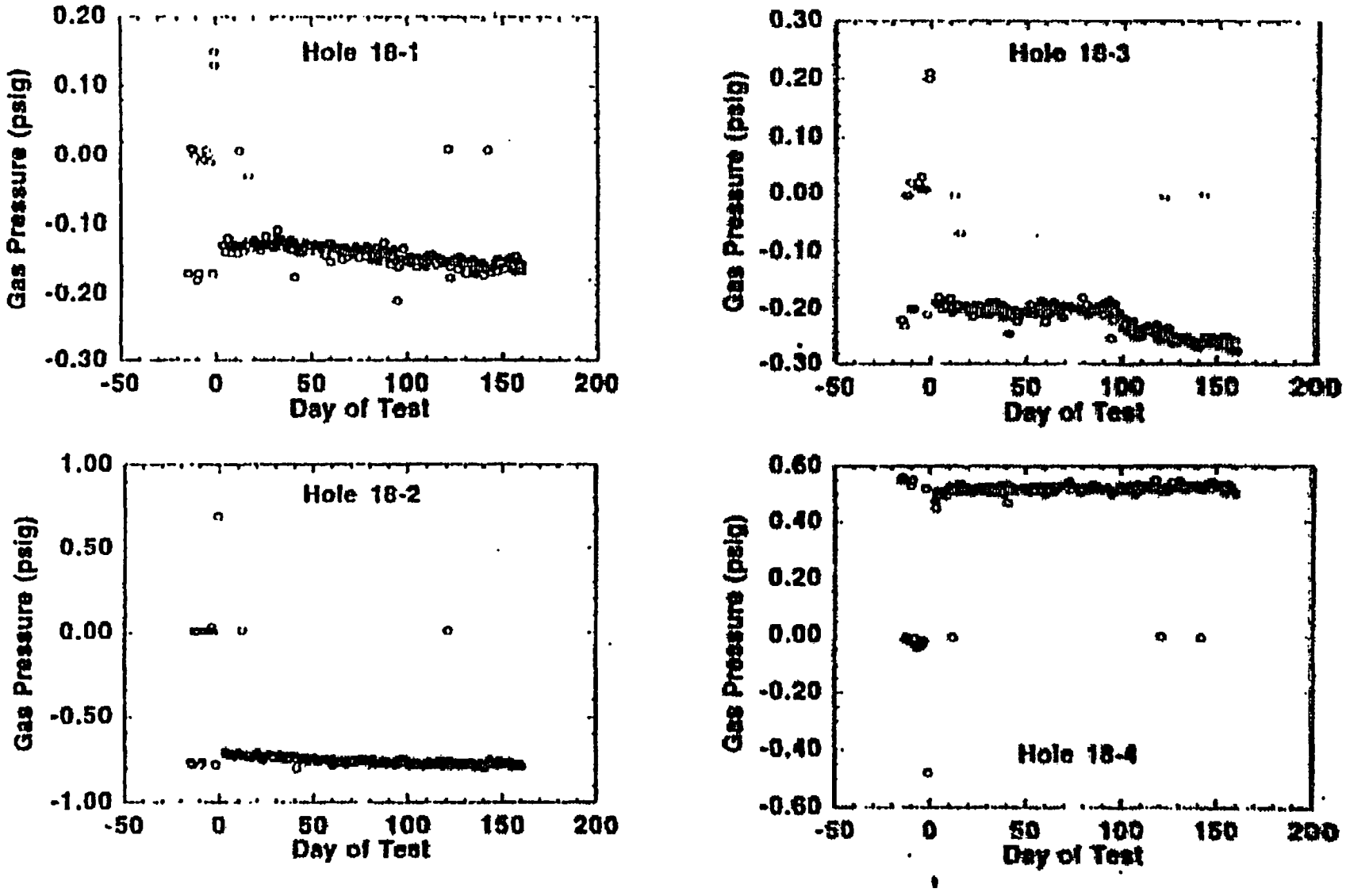

Figure 4-37. Chronology of Gauge Gas Pressure in Four Zones of Borehole 18

will have the greatest effect on the measurement. Therefore, neutron logging is good for detecting local variations in moisture content. On the other hand the ERT is designed to determine the distribution of moisture content in a two-dimensional plane. The ERT is good for determining regional variation in moisture content. As part of the pretest forecast, the three-dimensional model using the NUFT code was applied to the SHT to forecast the changes in the moisture content along the neutron logging boreholes. Predictions will be compared with the neutron logging measurements and the ERT images in the following discussion.

Figures 4-38 to 4-41 show the predicted saturation of water along boreholes 15, 17, 22 and 23 respectively, as a function of distance from the collar in each borehole. An equivalent continuum model (ECM) with an initial saturation of 92 percent is used in the prediction. The moisture content at the end of a five-month heating is compared with the neutron logging conducted on January 30, 1997, which was a few days after the fifth month of heating. The neutron logging results are shown in Figure 4-42. To show the effect of heating on the moisture content, Figure 4-42 shows the difference in the smoothed neutron counts between January 30, 1997 and the ambient data on August 22, 1996. Both the neutron logging results on January 30, 1997 and the preheat data were smoothed using a five-point smoothing algorithm. The calibration of the neutron tool for the exact borehole construction, (i.e., Teflon liner and cement grout) with respect to equivalent moisture content has not been conducted. Therefore, only neutron counts instead of moisture content are presented. But the neutron counts should have the same information concerning the relative drying and wetting as the reduced moisture content. Note that the difference in neutron counts depend on the preheat data on the calculated differences. Because only one set of preheat data was available, the uncertainty in the difference in the neutron counts is large. Another source of uncertainty comes from local variations in the rock mass property, such as fractures and changes in porosity. These were not considered in the predictions.

As shown in Figure 4-38, the model calculations predict that the liquid saturation level in borehole 15 will increase from the initial level of 92 percent at the collar as the distance from the collar increases. The saturation level should reach a maximum level where the distance between the borehole and the heater is the shortest. This is because the heat-driven moisture, moving away from the heater, reaches this portion of the borehole. The measured data are shown in the small figure at the upper-left corner of Figure 4-42. Negative difference neutron counts indicate less moisture content than the preheat condition. Positive difference in neutron counts indicates increases in moisture content. The measured data show dry-out regions near the collar and near the heater.

The predicted saturation levels in borehole 17 are shown in Figure 4-39 and the measured data are shown in the upper-right corner of Figure 4-42. Both of the predicted and measured results show a dry-out near x=6.0 m, where the neutron borehole is near the heater, and an increase in moisture content in the outer region of the borehole. However, the measured data, show a large decrease in moisture content at x=4.8 m, which was not predicted. This behavior could be from the uncertainty in the preheat measurements or local variations as mentioned above.

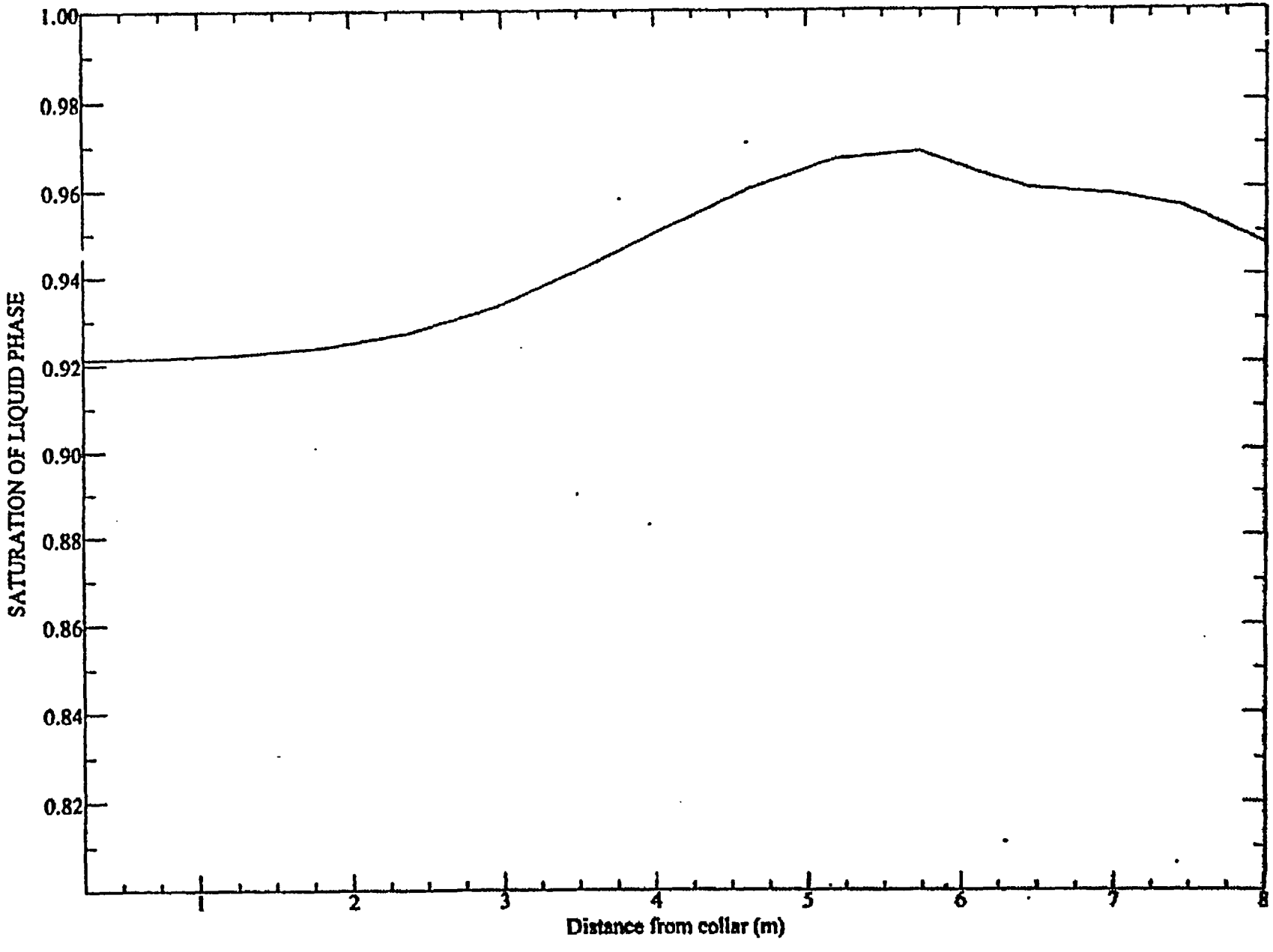

Figure 4-38. Predicted Liquid Saturation Profile Along Borehole 16 after 5 Months of Heating (Three-Dimensional Predictions; Thermo-Hydrologic; 12-Month Heating)

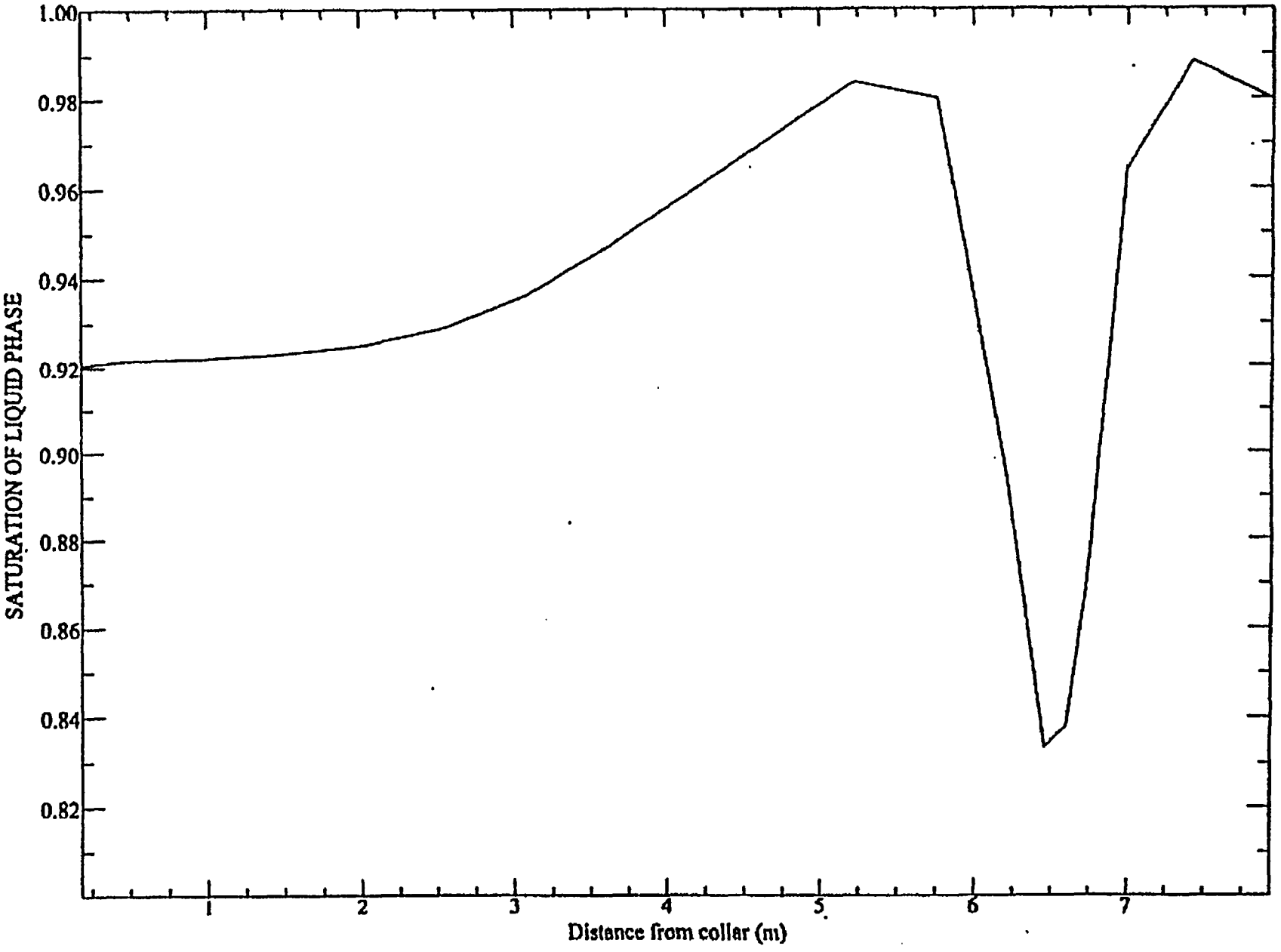

Figure 4-39. Predicted Liquid Saturation Profile Along Borehole 17 after 5 Months of Heating (Three-Dimensional Predictions; Thermo-Hydrologic; 12-Month Heating)

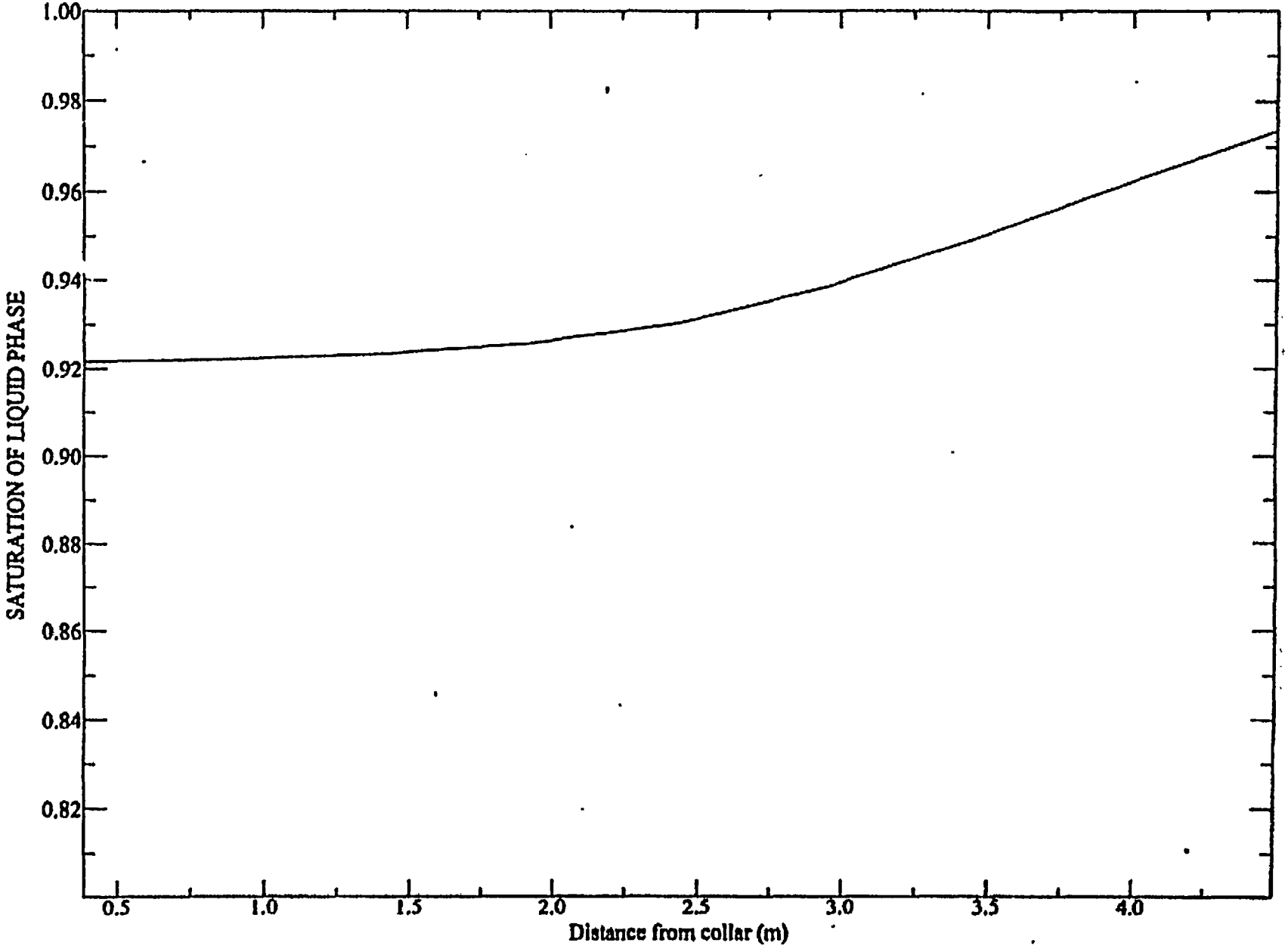

Figure 4-40. Predicted Liquid Saturation Profile Along Borehole 22 after 6 Months of Heating (Three-Dimensional Predictions; Thermo-Hydrologic; 12-Month Heating)

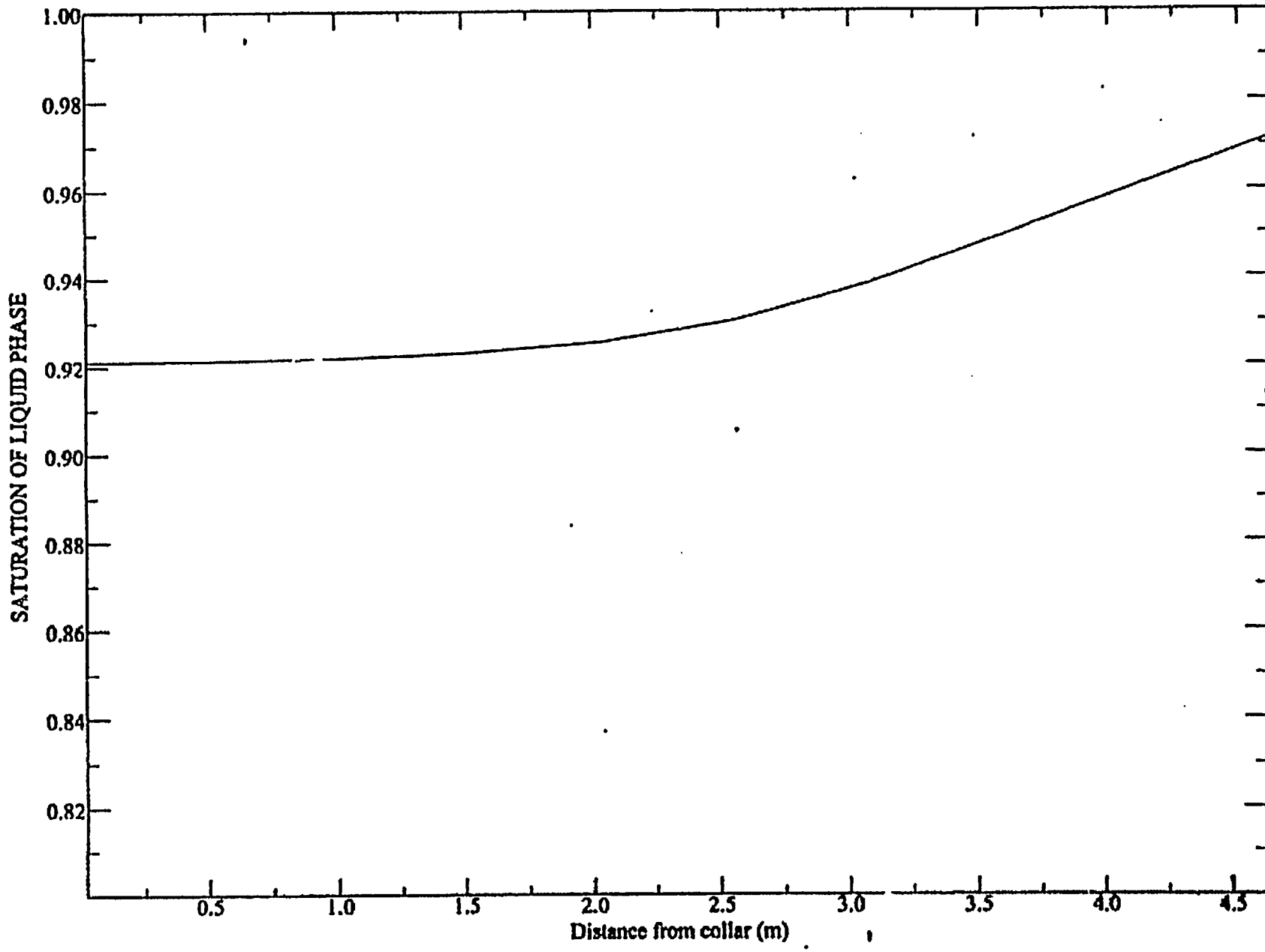

Figure 4-41. Predicted Liquid Saturation Profile Along Borehole 23 after 5 Months of Heating (Three-Dimensional Predictions; Thermo-Hydrologic; 12-Month Heating)

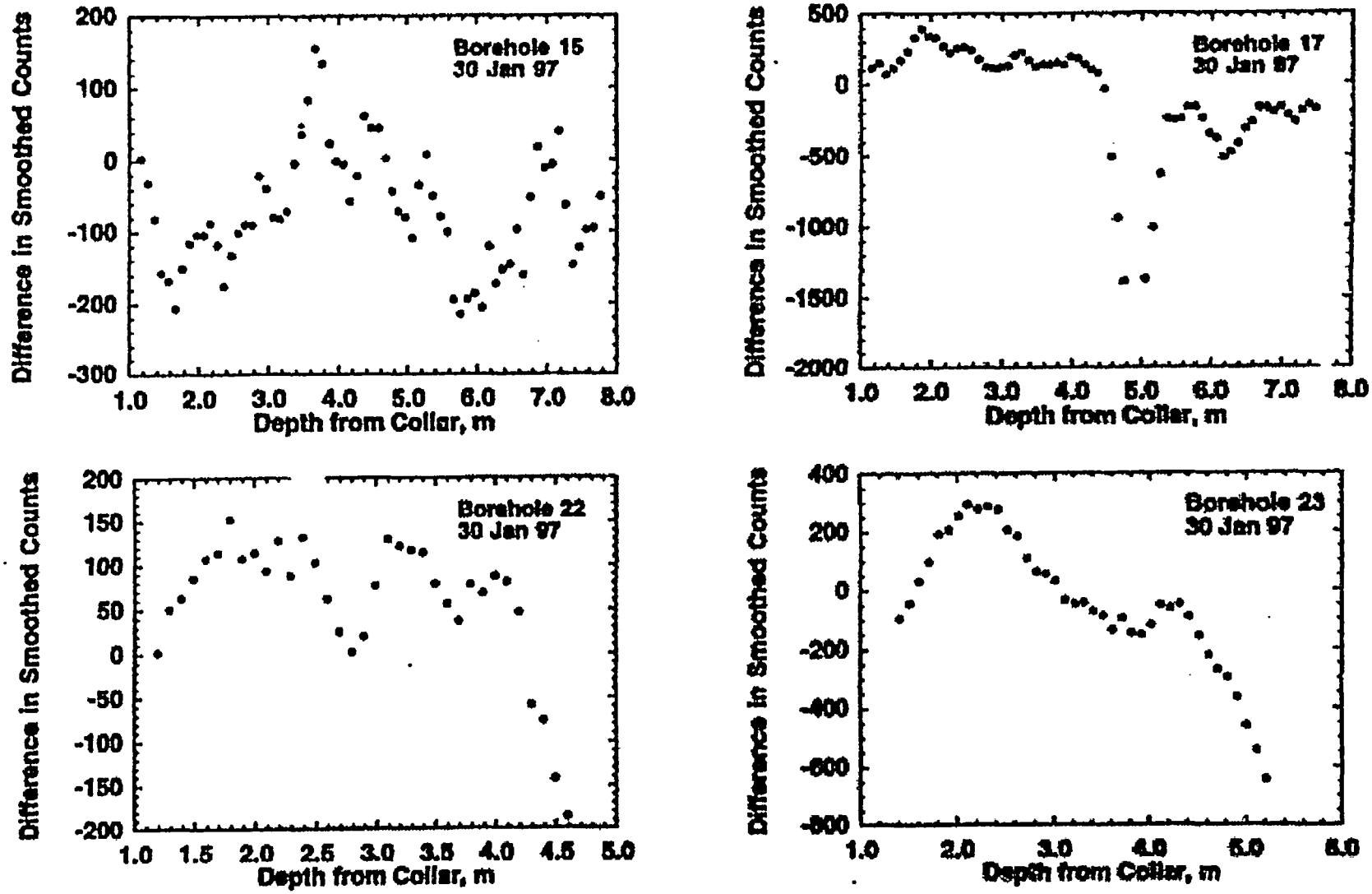

Figure 4-42. Difference in Smoothed Neutron Counts (Taken January 30, 1997) and Ambient Pre-Heat Data for Boreholes 15, 17, 22, and 23, as a Function of Collar Depth

For both boreholes 22 and 23, the model predicted an increase in moisture content for the entire length of the boreholes (Figures 4-40 and 4-41). The measured moisture content agrees with the predicted moisture content, except in regions near the bottom of the boreholes where the measured moisture content reveals a small region of dry-out.

The neutron data seem to indicate that heat has a stronger effect on the dry-out than predicted. However, caution should be taken in assessing the quantitative nature of the effect. Uncertainties associated with the measurement and the data reduction need to be further evaluated.

Several ERT measurements were conducted in boreholes 24 to 27. All of those ERT results have been reported in the first quarter report. ERT images are used to illustrate the nature of the ERT results. Figure 3-13 shows a tomography of resistivity ratio between October 24, 1996 and the ambient background measured on August 22, 1996. The concentric circles shown in the image illustrate the distribution of temperature in the region as measured by one of the thermocouple boreholes perpendicular to the heater borehole on October 23, 1996. As indicated by the resistivity ratio bar code, the resistivity ratio of the entire imaged region decreased from about 1.0 (meaning no change) near the boundary to about 0.5 near the center of the region, where the heater is nearby. Both increase in water saturation and temperature will contribute to the decrease in electrical resistivity in an ERT image. Laboratory measurements by Roberts and Lin (1991) indicate that a region of dry-out near the heater will be shown when the effect of temperature on the electrical resistivity is taken into consideration.

INTENTIONALLY LEFT BLANK

5. CONCLUSIONS

This interim report provides a baseline comparison of predictions and measurements of the thermal-mechanical-hydrologic-chemical (TMHC) behavior for initial heating (approximately four months) in the single heater test (SHT). The conclusions herein are grouped by each of the four TMHC processes considered in the SHT. In general, the SHT is progressing as planned. Although it is premature to completely assess these comparisons, early results are encouraging and the understanding of the coupled TMHC processes are being advanced by the SHT.

The comparison of predicted and measured temperatures indicates good overall agreement despite some temporal and spatial disparities. The ability to predict the measured temperature is important since the thermal behavior drives the mechanical, hydrological and chemical processes. Also, it appears that conduction is the dominate mode of heat transfer in the SHT block.

Comparison of predicted and measured data has led to the following observations of the thermal-mechanical responses. First, the agreement between predicted and measured displacements appears satisfactory for the initial few months of heating. Second, the anticipated one-way coupling of thermal and mechanical processes has been confirmed. Also, the measured data indicates that the presence of fractures substantially influences the TM behavior during the early stages of heating.

Measurements by electrical resistivity tomography (ERT), neutron logging, and ground penetrating radar (GPR) indicate the development of dry-out region surrounding the heater. Subsequent condensation of moisture at some distance away from the heater has also been observed. Predictions using the NUFT code do not closely compare with observations in this regard. Nonetheless, strong one-way thermal-hydrological coupling appears to exist in the SHT. Also, lowering of measured bulk air-permeability because of moisture condensation has been observed.

The thermal-chemical comparison of predicted and measured data is largely limited to the evaluation of the water extracted from zone 4 of borehole 16. Chemical analyses confirmed 16-4 water is condensate and appears to have been exposed to fracture filling minerals. The chemical sensors installed in the SHT block failed in the harsh thermal environment. Absorbent pads emplaced in boreholes have yielded samples for water chemistry analyses which are underway.

INTENTIONALLY LEFT BLANK

6. REFERENCES

ASTM. 1996. "*Standard Test Method for Determining the In Situ Modulus of Deformation of Rock Using the Diametrically Loaded 76-mm (3-in.) Borehole Jack.*" ASTM D4971-89. American Society for Testing and Materials, West Conshohocken, PA.

Bodvarsson, G.S., T.M. Bandurraga (eds.). *Development and Calibration of the Three-Dimensional Site Scale Unsaturated Zone Model of Yucca Mountain*, Nevada, Lawrence Berkeley National Laboratory report, Berkeley, CA, 1996.
DTN: LB960800831229.001

Biffle. J.H. 1993. *JAC3D - A Three-Dimensional Finite Element Computer Program for the Nonlinear Quasi-static Response of Solids with the Conjugate Gradient Method.* SAND87-1305. Sandia National Laboratories, Albuquerque. New Mexico.

Birkholzer, J. T. and Tsang, Y. W. 1996. *Forecast of Thermal-Hydrological Conditions and Air Injection Test Results of the Single Heater Test*, Lawrence Berkeley National. December 1996.

Cook and Wang, 1997. *Infrared Imaging in the Single Heater Test Area*, Lawrence Berkeley National Laboratory, Berkeley CA., 1997.

Carlos, B., 1987. *Minerals in Fractures of the Saturated Zone from Drill Core USW G-4*, Yucca Mountain. Nye County, Nevada. LA-10927-MS. Los Alamos National Laboratory. Los Alamos. New Mexico.

Carlos. B., 1989. *Fracture-Coating Minerals in the Topopah Spring Member and Upper Tuff of the Calico Hills from Drill Hole J-13.* LA-11504-MS. Los Alamos National Laboratory, Los Alamos, New Mexico.

Carlos, B., 1994, *Field Guide to Fracture-Lining Minerals, Yucca Mountain, Nevada.* LA-12803-MS. Los Alamos National Laboratory, Los Alamos, New Mexico.

Craig, H., 1961. *Isotopic Variations In Meteoric Waters.* Science, v. 133, p. 1702-1703.

CRWMS M&O, 1996a. *Test Design, Plans and Layout Report*, M&O Report BAB000000-01717-4600-00025. July 30, 1996. Yucca Mountain Site Characterization Project. TRW Environmental Safety Systems, Las Vegas. Nevada.

CRWMS M&O 1996b. *Characterization of the ESF Thermal Test Area*, Report B00000000-01717-5705-00047, September 1996.

Daily, W., Lin, W., and Buscheck, T., 1987. *Hydrology of Topopah Spring Tuff - Laboratory Measurements.* J. Geophysical Research, v. 92, p. 7854-7864.

DOE (U.S. Department of Energy). 1988. "*Site Characterization Plan. Yucca Mountain Site. Nevada Research and Development Area. Nevada.*" DOE/RW-0199.

DOE (Department of Energy), 1995 YMSCO (Yucca Mountain Site Characterization Office)-003. 1995. *In Situ Thermal Testing Program Strategy.*

DOE (Department of Energy), 1995, "*In Situ Thermal Testing Program.*" DOE/YMSCO-003. Yucca Mountain Site Characterization Project, Las Vegas, Nevada.

DOE (Department of Energy), 1988, "*Site Characterization Plan: Yucca Mountain Site, Nevada Research and Development Area, Nevada.*" DOE/RW-0199, Oak Ridge Tennessee. Office of Scientific and Technical Information.

Freifeld, B. and Tsang, Y., 1997 Letter Report on First Quarter Results of Measurements in Hydrology Holes in Single Heater Test Area in the ESF. Lawrence Berkeley National Laboratory. January 1997.

Glassley, W.E., and Boyd, S., 1995. *Preliminary Description of Small Block Mineralogical Features,* Data Report. Yucca Mountain Site Characterization Project Milestone M0L062.

Glassley, W.E., 1997. *Thermochemical Analysis of the Single Heater Test.* Yucca Mountain Site Characterization Project Milestone SP912M4.

Harrar, J., Carley, J.F., Isherwood, W.F., and Raber, E., 1990. Report of the committee to review the use of J-13 well water in Nevada Nuclear Waste Storage Investigations. Lawrence Livermore National Laboratory, UCID-21867.

Heuze, F.E. and B. Amadei. 1985. "The NX-Borehole Jack: A Lesson In Trials and Errors," *International Journal of Rock Mechanics, Mineral Sciences, and Geomechanics Abstracts.* Vol. 22, no. 2, pp. 105-112.

Lee, K. H. 1996. *Forecast Thermo-Hydrologic Results of the Single Heater Test.* Lawrence Livermore National Laboratory, Livermore, California, December 1996.

Lin, W. and Daily, W., 1984. Transport properties of Topopah Spring Tuff. Lawrence Livermore National Laboratory, Livermore, CA. UCRL-53602.

Lin, W., 1991. *Variation of Permeability with Temperature in Fractured Topopah Spring Tuff Samples.* Proceedings, 2nd Annual Int. Conf. on High Level Radioactive Waste Management, Las Vegas, NV, April 28 - May 3, 1991 (American Nuclear Society, La Grange Park, IL). p. 988-993.

Lin, W., Roberts, J.J., Glassley, W.E., and Ruddle, D. 1995. *The Effect of Rock-Water Interaction on Permeability.* Lawrence Livermore National Laboratory, Livermore, CA. UCRL-JC-119574.

Morelli, G. and LaBrecque, D. 1996. *Robust Scheme for ERT Inverse Modeling,* Proceedings of the Symposium on the Application of Geophysics to Engineering and Environmental Problems,

Keystone. CO. April 28-May 1. 1996; sponsored by the Environmental and Engineering Geophysical Society.

Nitao. J. J., "*Numerical Modeling of the Thermal and Hydrological Environment around a Nuclear Waste Package using the Equivalent Continuum Approximation: Horizontal Emplacement.*" Lawrence Livermore National Laboratory, Livermore. CA, UCID-21444 (1988).

Popov, E.P., *Mechanics of Materials*, 2nd edition, Prentice Hall, Englewood Cliffs, NJ.

Pruess, K. TOUGH2 - *A General-Purpose Numerical Simulator for Multiphase Fluid and Heat Flow.* Lawrence Berkeley National Laboratory report LBL-29400, Berkeley, CA. 1991.

Ramirez. et al, 1997. *Electrical Resistivity Monitoring of the Thermomechanical Heater Test in Yucca Mountain.* Lawrence Livermore National Laboratory. TDIF submitted. DTN LL9701004244.026.

Sandia National Laboratories (SNL), 1996. "Pre-Experiment Predictions of T-H-M Response to the Single Heater Test," Work Agreement WA-0319, Sandia National Laboratories, Albuquerque, New Mexico.

Sandia National Laboratories, 1997, "*Evaluate Measurements and Analyze Single Heater Test First Quarter Results (8/26/96 through 11/30/96)*," Sandia National Laboratory, TDIF No. 305940. DTN SNF35110695001.003, Albuquerque, NM.

Sandia National Laboratory (SNL) 1997. *Evaluate Measurements and Analyze Single Heater Test First Quarter Results.* Albuquerque, NM. January 1997.

Sobolik, S.R., N.D. Francis, J. Pott 1996. *Pre-Experiment Thermal-Hydrological-Mechanical Analyses for the ESF Single Heater Test*, Sandia National Laboratory Letter Report SLTR96-0004, 1996. Albuquerque, NM, December 1996.

Sobolik, S.R., Francis, N.D., and Finley, R.E., 1996, "*Pre-Experiment Thermal-Hydrological-Mechanical Analyses for the ESF Single Heater Test - Phase 2*," Sandia National Laboratories Letter Report, SLTR96-0005, Albuquerque, NM.

Steefel. C.I. and Yabusaki. S.B. 1995. OS3D/GIMRT: Software for modeling multicomponent-multidimensional reactive transport. Pacific Northwest Laboratory. Richland. Washington.

Tsang, Y.W., J. Wang, B. Freifeld, P. Cook, R. Suarez-Rivera, T. Tokunaga, Letter report on hydrological characterization of the single heater test area in the ESF, Level 4 Milestone for WBS 1.2.3.14.2, August 1996. DTN: LB960500834244.001

van Genuchten, M., 1980. "A closed-form equation for predicting the hydraulic conductivity of unsaturated soils," *Soil Science Society of America Journal*, Vol. 44, pp. 892- 898.

Wilder, D. G., 1996, Near Field and Altered Zone Environment Report. Lawrence Livermore National Laboratory. UCRL-LR-124998. Livermore. CA.

Wolery, T.J. 1992. EQ3/6, A software package for geochemical modeling of aqueous systems: Package overview and installation guide. Lawrence Livermore National Laboratory. Livermore. CA. UCRL-MA-110662 PT.

Wuman, L. and Roberts, J. 1997. *Neutron Logging Measurements in the Single Heater Test.* Lawrence Livermore National Laboratory, 1997.

Zimmerman, R.M., and Finley, R.E., 1986, "Summary of Geomechanical Measurements Taken In and Around the G-Tunnel Underground Facility, NTS." Sandia National Laboratories Report SAND86-1015, Albuquerque. NM.

APPENDIX A

AS-BUILT SENSORS COORDINATES FOR SINGLE HEATER TEST

Table A-1. As-Built Sensors Coordinates for Single Heater Test

Sensor Identification	*Coordinates (meters)		
	X	Y	Z
TMA-H-1-TCT-1	-0.008	6.970	0.048
TMA-H-1-TCT-2	-0.007	6.470	0.046
TMA-H-1-TCT-3	-0.007	5.970	0.045
TMA-H-1-TCT-4	-0.006	5.470	0.043
TMA-H-1-TCT-5	-0.005	4.470	0.040
TMA-H-1-TCT-6	-0.004	3.470	0.037
TMA-H-1-TCT-7	-0.003	2.970	0.035
TMA-H-1-TCT-8	-0.003	2.470	0.033
TMA-H-1-TCT-9	-0.002	1.970	0.032
TMA-H-1-TCS-1	-0.041	6.970	0.002
TMA-H-1-TCS-2	-0.040	6.470	0.000
TMA-H-1-TCS-3	-0.040	5.970	-0.001
TMA-H-1-TCS-4	-0.039	5.470	-0.003
TMA-H-1-TCS-5	-0.038	4.470	-0.006
TMA-H-1-TCS-6	-0.037	3.470	-0.009
TMA-H-1-TCS-7	-0.036	2.970	-0.011
TMA-H-1-TCS-8	-0.036	2.470	-0.013
TMA-H-1-TCS-9	-0.035	1.970	-0.014
TMA-H-1-TCB-1	-0.008	6.970	-0.018
TMA-H-1-TCB-2	-0.007	6.470	-0.021
TMA-H-1-TCB-3	-0.007	5.970	-0.022
TMA-H-1-TCB-4	-0.006	5.470	-0.024
TMA-H-1-TCB-5	-0.005	4.470	-0.027
TMA-H-1-TCB-6	-0.004	3.470	-0.030
TMA-H-1-TCB-7	-0.003	2.970	-0.032
TMA-H-1-TCB-8	-0.003	2.470	-0.034
TMA-H-1-TCB-9	-0.002	1.970	-0.035
TMA-TC-1A-1	-0.275	7.977	0.367
TMA-TC-1A-2	-0.269	7.477	0.364
TMA-TC-1A-3	-0.264	6.977	0.360
TMA-TC-1A-4	-0.259	6.477	0.356
TMA-TC-1A-5	-0.253	5.978	0.353
TMA-TC-1A-6	-0.248	5.478	0.349
TMA-TC-1A-7	-0.237	4.478	0.342
TMA-TC-1A-8	-0.226	3.478	0.335
TMA-TC-1A-9	-0.221	2.978	0.331
TMA-TC-1A-10	-0.215	2.478	0.328
TMA-TC-1B-1	-0.213	2.218	0.326
TMA-TC-1B-2	-0.207	1.718	0.322
TMA-TC-1B-3	-0.202	1.218	0.319
TMA-TC-1B-4	-0.196	0.718	0.315
TMA-TC-1B-5	-0.191	0.218	0.312

* Origin is at Center of Heater Collar

Table A-1. As-Built Sensors Coordinates for Single Heater Test (Continued)

Sensor Identification	*Coordinates (meters)		
	X	Y	Z
TMA-TC-2A-1	0.609	8.136	0.263
TMA-TC-2A-2	0.610	7.636	0.260
TMA-TC-2A-3	0.610	7.136	0.277
TMA-TC-2A-4	0.611	6.636	0.274
TMA-TC-2A-5	0.611	6.136	0.272
TMA-TC-2A-6	0.612	5.636	0.269
TMA-TC-2A-7	0.613	4.636	0.263
TMA-TC-2A-8	0.614	3.636	0.257
TMA-TC-2A-9	0.615	3.136	0.254
TMA-TC-2A-10	0.615	2.636	0.251
TMA-TC-2B-1	0.615	2.126	0.248
TMA-TC-2B-2	0.616	1.626	0.245
TMA-TC-2B-3	0.617	1.126	0.242
TMA-TC-2B-4	0.617	0.626	0.239
TMA-TC-2B-5	0.618	0.126	0.237
TMA-TC-3A-1	-0.719	8.268	1.342
TMA-TC-3A-2	-0.721	7.768	1.338
TMA-TC-3A-3	-0.723	7.268	1.335
TMA-TC-3A-4	-0.725	6.768	1.332
TMA-TC-3A-5	-0.728	6.268	1.328
TMA-TC-3A-6	-0.730	5.768	1.325
TMA-TC-3A-7	-0.734	4.768	1.318
TMA-TC-3A-8	-0.738	3.768	1.312
TMA-TC-3A-9	-0.741	3.268	1.308
TMA-TC-3A-	-0.743	2.768	1.305
TMA-TC-3B-1	-0.745	2.298	1.302
TMA-TC-3B-2	-0.747	1.798	1.299
TMA-TC-3B-3	-0.749	1.298	1.295
TMA-TC-3B-4	-0.751	0.798	1.292
TMA-TC-3B-5	-0.754	0.298	1.289
TMA-TC-4A-1	-0.117	6.888	-0.759
TMA-TC-4A-2	-0.111	6.388	-0.752
TMA-TC-4A-3	-0.104	5.888	-0.745
TMA-TC-4A-4	-0.097	5.388	-0.738
TMA-TC-4A-5	-0.090	4.888	-0.731
TMA-TC-4A-6	-0.083	4.388	-0.724
TMA-TC-4A-7	-0.070	3.388	-0.709
TMA-TC-4A-8	-0.056	2.389	-0.695
TMA-TC-4A-9	-0.050	1.889	-0.688
TMA-TC-4A-10	-0.043	1.389	-0.681

* Origin is at Center of Heater Collar

Table A-1. As-Built Sensors Coordinates for Single Heater Test (Continued)

Sensor Identification	*Coordinates (meters)		
	X	Y	Z
TMA-TC-4B-1	-0.052	2.099	-0.691
TMA-TC-4B-2	-0.046	1.599	-0.684
TMA-TC-4B-3	-0.039	1.099	-0.677
TMA-TC-4B-4	-0.032	0.599	-0.670
TMA-TC-4B-5	-0.025	0.099	-0.662
TMA-TC-5A-1	-0.059	8.145	0.712
TMA-TC-5A-2	-0.056	7.645	0.710
TMA-TC-5A-3	-0.053	7.145	0.708
TMA-TC-5A-4	-0.050	6.645	0.706
TMA-TC-5A-5	-0.047	6.145	0.705
TMA-TC-5A-6	-0.044	5.645	0.703
TMA-TC-5A-7	-0.038	4.645	0.699
TMA-TC-5A-8	-0.032	3.645	0.696
TMA-TC-5A-9	-0.029	3.145	0.694
TMA-TC-5A-10	-0.025	2.645	0.692
TMA-TC-5B-1	-0.023	2.225	0.691
TMA-TC-5B-2	-0.020	1.725	0.689
TMA-TC-5B-3	-0.017	1.225	0.687
TMA-TC-5B-4	-0.014	0.725	0.685
TMA-TC-5B-5	-0.011	0.225	0.683
TMA-TC-6-1	0.617	5.417	-0.016
TMA-TC-6-2	0.757	5.418	-0.015
TMA-TC-6-3	0.917	5.419	-0.014
TMA-TC-6-4	1.257	5.421	-0.012
TMA-TC-6-5	1.507	5.423	-0.011
TMA-TC-6-6	1.737	5.424	-0.010
TMA-TC-6-7	2.257	5.428	-0.007
TMA-TC-6-8	3.257	5.434	-0.001
TMA-TC-6-9	4.257	5.441	0.005
TMA-TC-6-10	5.257	5.447	0.010
TMA-TC-7-1	-0.960	3.400	0.007
TMA-TC-7-2	-1.100	3.401	0.008
TMA-TC-7-3	-1.260	3.402	0.008
TMA-TC-7-4	-1.600	3.403	0.009
TMA-TC-7-5	-1.850	3.404	0.010
TMA-TC-7-6	-2.080	3.406	0.010
TMA-TC-7-7	-2.600	3.408	0.011
TMA-TC-7-8	-3.600	3.413	0.014
TMA-TC-7-9	-4.600	3.418	0.016
TMA-TC-7-10	-5.600	3.423	0.019

* Origin is at Center of Heater Collar

Table A-1. As-Built Sensors Coordinates for Single Heater Test (Continued)

Sensor Identification	*Coordinates (meters)		
	X	Y	Z
TMA-BX-1-TC-1	0.131	6.863	0.310
TMA-BX-1-TC-2	0.136	6.023	0.309
TMA-BX-1-TC-3	0.142	5.023	0.307
TMA-BX-1-TC-4	0.148	4.023	0.306
TMA-BX-1-TC-5	0.154	3.023	0.304
TMA-BX-1-TC-6	0.161	2.023	0.303
TMA-BX-1-TC-7	0.164	1.543	0.302
TMA-BX-1-TC-8	0.167	1.043	0.301
TMA-BX-1-TC-9	0.170	0.543	0.301
TMA-BX-2-TC-1	-0.631	7.093	0.281
TMA-BX-2-TC-2	-0.630	6.543	0.278
TMA-BX-2-TC-3	-0.630	6.023	0.274
TMA-BX-2-TC-4	-0.629	5.473	0.271
TMA-BX-2-TC-5	-0.628	4.883	0.267
TMA-BX-2-TC-6	-0.628	4.333	0.263
TMA-BX-2-TC-7	-0.627	3.773	0.259
TMA-BX-2-TC-8	-0.626	3.223	0.256
TMA-BX-2-TC-9	-0.626	2.623	0.252
TMA-BX-2-TC-10	-0.625	2.073	0.248
TMA-BX-2-TC-11	-0.625	1.513	0.245
TMA-BX-2-TC-12	-0.624	0.963	0.241
TMA-BX-2-TC-13	-0.623	0.390	0.237
TMA-BX-3-TC-1	0.768	6.887	1.314
TMA-BX-3-TC-2	0.765	6.047	1.309
TMA-BX-3-TC-3	0.762	5.047	1.302
TMA-BX-3-TC-4	0.759	4.047	1.295
TMA-BX-3-TC-5	0.756	3.047	1.288
TMA-BX-3-TC-6	0.753	2.047	1.281
TMA-BX-3-TC-7	0.752	1.567	1.277
TMA-BX-3-TC-8	0.750	1.067	1.274
TMA-BX-3-TC-9	0.749	0.567	1.270
TMA-BX-4-TC-1	0.788	3.460	-0.176
TMA-BX-4-TC-2	1.108	3.460	-0.171
TMA-BX-4-TC-3	1.448	3.460	-0.165
TMA-BX-4-TC-4	1.928	3.461	-0.156
TMA-BX-4-TC-5	2.448	3.461	-0.147
TMA-BX-4-TC-6	2.928	3.461	-0.139
TMA-BX-4-TC-7	3.447	3.461	-0.130
TMA-BX-4-TC-8	3.927	3.461	-0.122
TMA-BX-4-TC-9	4.447	3.461	-0.112

* Origin is at Center of Heater Collar

Table A-1. As-Built Sensors Coordinates for Single Heater Test (Continued)

Sensor Identification	*Coordinates (meters)		
	X	Y	Z
TMA-BX-4-TC-10	4.927	3.462	-0.104
TMA-BX-4-TC-11	5.447	3.462	-0.095
TMA-BX-4-TC-12	5.927	3.462	-0.087
TMA-RTD-15-1	-1.592	4.245	2.768
TMA-RTD-15-2	-1.320	4.246	2.682
TMA-RTD-15-3	-1.030	4.246	2.592
TMA-RTD-15-4	-0.750	4.247	2.504
TMA-RTD-15-5	-0.468	4.247	2.416
TMA-RTD-15-6	-0.185	4.248	2.327
TMA-RTD-15-7	0.097	4.248	2.239
TMA-RTD-15-8	0.382	4.249	2.149
TMA-RTD-15-9	0.662	4.249	2.061
TMA-RTD-15-10	0.948	4.250	1.972
TMA-RTD-15-11	1.229	4.250	1.884
TMA-RTD-15-12	1.509	4.251	1.796
TMA-RTD-15-13	1.794	4.251	1.707
TMA-RTD-15-14	2.078	4.252	1.618
TMA-RTD-15-15	2.361	4.252	1.529
TMA-RTD-15-16	2.641	4.253	1.442
TMA-RTD-15-17	2.922	4.253	1.354
TMA-RTD-15-18	3.203	4.254	1.266
TMA-RTD-15-19	3.488	4.254	1.176
TMA-RTD-15-20	3.770	4.255	1.088
TMA-RTD-15-21	4.047	4.255	1.001
TMA-RTD-15-22	4.330	4.256	0.913
TMA-RTD-15-23	4.613	4.256	0.824
TMA-RTD-15-24	4.896	4.257	0.735
TMA-RTD-15-25	5.173	4.257	0.648
TMA-RTD-15-26	5.457	4.258	0.559
TMA-RTD-15-27	5.741	4.258	0.471
TMA-RTD-15-28	6.025	4.259	0.382
TMA-RTD-15-29	6.259	4.259	0.308
TMA-TEMP-16-1	5.233	4.271	0.191
TMA-TEMP-16-2	4.540	4.274	0.283
TMA-TEMP-16-3	3.848	4.277	0.375
TMA-TEMP-16-4	3.155	4.280	0.467
TMA-RTD-17-1	-1.767	4.275	-1.438
TMA-RTD-17-2	-1.474	4.275	-1.401
TMA-RTD-17-3	-1.184	4.274	-1.364
TMA-RTD-17-4	-0.879	4.274	-1.325

* Origin is at Center of Heater Collar

Table A-1. As-Built Sensors Coordinates for Single Heater Test (Continued)

Sensor Identification	*Coordinates (meters)		
	X	Y	Z
TMA-RTD-17-5	-0.521	4.273	-1.279
TMA-RTD-17-6	-0.263	4.273	-1.248
TMA-RTD-17-7	0.018	4.272	-1.210
TMA-RTD-17-8	0.317	4.272	-1.171
TMA-RTD-17-9	0.615	4.272	-1.133
TMA-RTD-17-10	0.906	4.271	-1.096
TMA-RTD-17-11	1.208	4.271	-1.057
TMA-RTD-17-12	1.501	4.270	-1.020
TMA-RTD-17-13	1.798	4.270	-0.982
TMA-RTD-17-14	2.100	4.270	-0.943
TMA-RTD-17-15	2.392	4.269	-0.906
TMA-RTD-17-16	2.692	4.269	-0.867
TMA-RTD-17-17	2.995	4.268	-0.829
TMA-RTD-17-18	3.293	4.268	-0.790
TMA-RTD-17-19	3.585	4.268	-0.753
TMA-RTD-17-20	3.888	4.267	-0.714
TMA-RTD-17-21	4.177	4.267	-0.677
TMA-RTD-17-22	4.473	4.266	-0.639
TMA-RTD-17-23	4.775	4.266	-0.600
TMA-RTD-17-24	5.076	4.265	-0.562
TMA-RTD-17-25	5.371	4.265	-0.524
TMA-RTD-17-26	5.660	4.265	-0.487
TMA-RTD-17-27	5.957	4.264	-0.449
TMA-RTD-17-28	6.260	4.264	-0.410
TMA-RTD-17-29	6.550	4.263	-0.373
TMA-TEMP-18-1	5.120	4.255	-0.205
TMA-TEMP-18-2	4.422	4.254	-0.215
TMA-TEMP-18-3	3.723	4.252	-0.224
TMA-TEMP-18-4	3.025	4.250	-0.234
TMA-RTD-22-1	-1.584	4.358	-0.711
TMA-RTD-22-2	-1.876	4.360	-0.706
TMA-RTD-22-3	-2.172	4.362	-0.701
TMA-RTD-22-4	-2.469	4.364	-0.696
TMA-RTD-22-5	-2.764	4.366	-0.691
TMA-RTD-22-6	-3.065	4.368	-0.686
TMA-RTD-22-7	-3.358	4.370	-0.681
TMA-RTD-22-8	-3.658	4.372	-0.677
TMA-RTD-22-9	-3.954	4.374	-0.672
TMA-RTD-22-10	-4.251	4.376	-0.667
TMA-RTD-22-11	-4.546	4.378	-0.662
TMA-RTD-22-12	-4.842	4.380	-0.657

* Origin is at Center of Heater Collar

Table A-1. As-Built Sensors Coordinates for Single Heater Test (Continued)

Sensor Identification	*Coordinates (meters)		
	X	Y	Z
TMA-RTD-22-13	-5.138	4.382	-0.652
TMA-RTD-22-14	-5.440	4.384	-0.647
TMA-RTD-22-15	-5.731	4.386	-0.642
TMA-RTD-22-16	-6.031	4.388	-0.638
TMA-RTD-22-17	-6.336	4.390	-0.632
TMA-RTD-23-1	-1.337	4.385	0.674
TMA-RTD-23-2	-1.616	4.385	0.639
TMA-RTD-23-3	-1.902	4.386	0.604
TMA-RTD-23-4	-2.182	4.386	0.570
TMA-RTD-23-5	-2.466	4.387	0.535
TMA-RTD-23-6	-2.750	4.387	0.500
TMA-RTD-23-7	-3.030	4.388	0.465
TMA-RTD-23-8	-3.315	4.388	0.430
TMA-RTD-23-9	-3.596	4.388	0.396
TMA-RTD-23-10	-3.878	4.389	0.361
TMA-RTD-23-11	-4.166	4.389	0.325
TMA-RTD-23-12	-4.444	4.390	0.291
TMA-RTD-23-13	-4.727	4.390	0.256
TMA-RTD-23-14	-5.011	4.391	0.221
TMA-RTD-23-15	-5.288	4.391	0.187
TMA-RTD-23-16	-5.570	4.391	0.152
TMA-RTD-23-17	-5.853	4.392	0.117
TMA-RTD-23-18	-6.141	4.392	0.082
TMA-RTD-23-19	-6.423	4.393	0.047
TMA-STC-1	1.000	0.000	2.000
TMA-STC-2	1.000	0.000	0.000
TMA-STC-3	0.500	0.000	-1.000
TMA-STC-4	0.500	0.000	1.000
TMA-STC-5	-1.000	0.000	0.000
TMA-STC-6	3.000	0.000	0.750
TMA-STC-7	6.264	3.489	0.488
TMA-STC-8	6.264	3.489	-0.012
TMA-STC-9	6.264	3.489	-0.488
TMA-STC-10	6.264	5.489	0.988
TMA-STC-11	6.264	5.489	-0.012
TMA-STC-12	6.264	5.489	-1.012
TMA-STC-13	-6.593	3.463	0.493
TMA-STC-14	-6.593	3.463	-0.007
TMA-STC-15	-6.593	3.463	-1.007
TMA-STC-16	-6.593	5.463	0.993
TMA-STC-17	-6.593	5.463	-0.007
TMA-STC-18	-6.593	5.463	-0.507

* Origin is at Center of Heater Collar

Table A-1. As-Built Sensors Coordinates for Single Heater Test (Continued)

Sensor Identification	*Coordinates (meters)		
	X	Y	Z
TMA-STC-19	0.000	0.000	1.250
TMA-STC-20	4.000	0.000	0.000
TMA-STC-21	3.000	0.000	-0.750
TMA-STC-22	-3.000	0.000	0.750
TMA-STC-23	-4.000	0.000	0.000
TMA-STC-24	0.000	0.000	-1.250
TMA-STC-25	-6.593	1.963	1.993
TMA-STC-26	-6.593	1.963	-0.007
TMA-STC-27	-6.593	1.963	1.493
TMA-STC-28	6.264	1.989	1.988
TMA-STC-29	6.264	1.989	-0.012
TMA-STC-30	6.264	1.989	1.488
TMA-STC-31	6.264	4.489	-0.012
TMA-STC-32	6.264	6.989	-0.012
TMA-STC-33	6.264	6.989	1.488
TMA-STC-34	-6.593	4.463	-0.007
TMA-STC-35	-6.593	6.963	-0.007
TMA-STC-36	-6.593	6.963	1.493
TMA-IN-THRM-1	1.000	-0.076	2.000
TMA-IN-THRM-2	-3.000	-0.076	1.500
TMA-IN-THRM-3	0.500	-0.076	-1.000
TMA-IN-THRM-4	4.000	-0.076	0.000
TMA-IN-THRM-5	-1.000	-0.076	0.000
TMA-IN-THRM-6	6.340	5.500	1.000
TMA-IN-THRM-7	6.340	4.500	0.000
TMA-IN-THRM-8	6.340	3.500	-0.500
TMA-IN-THRM-9	6.340	5.500	-1.000
TMA-IN-THRM-10	6.340	7.000	-2.000
TMA-IN-THRM-11	-6.670	2.000	2.000
TMA-IN-THRM-12	-6.670	3.500	0.500
TMA-IN-THRM-13	-6.670	4.500	0.000
TMA-IN-THRM-14	-6.670	5.500	-0.500
TMA-IN-THRM-15	-6.670	3.500	-1.000
TMA-BX-1-1-THRM	0.173	0.043	0.300
TMA-BX-3-1-THRM	0.747	0.067	1.267
TMA-BX-4-1-THRM	6.427	3.462	-0.078
Multiple Point Borehole Extensometers			
TMA-BX-1-1	0.130	6.683	0.310
TMA-BX-1-2	0.136	6.043	0.309
TMA-BX-1-3	0.142	5.043	0.307
TMA-BX-1-4	0.148	4.043	0.306
TMA-BX-1-5	0.154	3.043	0.304
TMA-BX-1-6	0.161	2.043	0.303

* Origin is at Center of Heater Collar

Table A-1. As-Built Sensors Coordinates for Single Heater Test (Continued)

Sensor Identification	*Coordinates (meters)		
	X	Y	Z
TMA-BX-2-1	-0.631	7.093	0.281
TMA-BX-2-2	-0.630	6.023	0.274
TMA-BX-2-3	-0.628	4.883	0.267
TMA-BX-2-4	-0.627	3.773	0.259
TMA-BX-2-5	-0.626	2.623	0.252
TMA-BX-2-6	-0.625	1.513	0.245
TMA-BX-3-1	0.768	6.907	1.315
TMA-BX-3-2	0.765	6.067	1.309
TMA-BX-3-3	0.762	5.067	1.302
TMA-BX-3-4	0.759	4.067	1.295
TMA-BX-3-5	0.756	3.067	1.288
TMA-BX-3-6	0.753	2.067	1.281
TMA-BX-4-1	0.768	3.460	-0.177
TMA-BX-4-2	1.428	3.460	-0.165
TMA-BX-4-3	2.428	3.461	-0.148
TMA-BX-4-4	3.427	3.461	-0.130
TMA-BX-4-5	4.427	3.461	-0.113
TMA-BX-4-6	5.427	3.462	-0.095
Rock Bolt Load Cells			
TMA-RB-LC-1-AVG	0.180	-0.300	-0.370
TMA-RB-LC-2-AVG	0.180	-0.300	-0.370
TMA-RB-LC-3-AVG	0.620	-0.300	-0.210
TMA-RB-LC-4-AVG	0.620	-0.300	-0.210
TMA-RB-LC-5-AVG	-0.180	-4.700	-0.370
TMA-RB-LC-6-AVG	-0.180	-4.700	-0.370
TMA-RB-LC-7-AVG	0.620	-4.700	-0.290
TMA-RB-LC-8-AVG	0.620	-4.700	-0.290
Wire Extensometer			
TMA-WX-1 (top)	2.098	0.000	2.230
TMA-WX-1 (bottom)	1.983	0.000	-1.240
TMA-WX-2 (top)	-2.040	0.000	2.591
TMA-WX-2 (bottom)	-2.085	0.000	-0.914
TMA-WX-3 (top)	6.264	3.612	2.752
TMA-WX-3 (bottom)	6.264	3.582	-0.978
TMA-WX-4 (top)	6.264	5.633	2.759
TMA-WX-4 (bottom)	6.264	5.613	-1.041
TMA-WX-5 (top)	-6.593	3.622	1.477
TMA-WX-5 (bottom)	-6.593	3.712	-1.558
TMA-WX-6 (top)	-6.593	5.735	1.216
TMA-WX-6 (bottom)	-6.593	5.735	-1.784

* Origin is at Center of Heater Collar

Table A-1. As-Built Sensors Coordinates for Single Heater Test (Continued)

Sensor Identification	*Coordinates (meters)		
	X	Y	Z
Tape Extensometer			
TMA-WXM-1	2.006	0.000	-0.295
TMA-WXM-2	-1.960	0.000	0.121
TMA-WXM-3	6.264	3.702	0.012
TMA-WXM-4	6.264	5.603	-0.056
TMA-WXM-5	-6.583	3.722	0.012
TMA-WXM-6	-6.583	5.735	-0.019

* Origin is at Center of Heater Collar